Strange and Deformed : A Study of Strangeness Production in U+U collisions at $\sqrt{s_{NN}} = 193$ GeV in STAR

A Thesis submitted to the Sambalpur University
For the Award of
Doctor of Philosophy
in
Science (Physics)

by
Srikanta Kumar Tripathy
Ph.D. Regn No. 159/2016/Phy

Institute of Physics, Bhubaneswar
October 2019

To them,
Whose unknown silent contributions made
this happen.

CERTIFICATE

We certify that Srikanta Kumar Tripathy has prepared his thesis entitled Strange and Deformed : A Study of Strangeness Production in U+U collisions at $\sqrt{s_{NN}}$ = 193 GeV in STAR, for the award of Ph.D. degree of the Sambalpur University, under our guidance. He has carried out the work jointly at the School of Physics, Sambalpur University and Institute of Physics, Bhubaneswar.

(Dr. Pradip Kumar Sahu)
Institute of physics
Bhubaneswar-751005
India

(Dr. Zashmir Naik)
Sambalpur University
Burla-768019
India

October 19, 2019

DECLARATION

I declare that the thesis entitled Strange and Deformed : A Study of Strangeness Production in U+U collisions at $\sqrt{s}_{NN} = 193$ GeV in STAR has been prepared by me under the guidance of Dr. Pradip Kumar Sahu, Institute of physics, Bhubaneswar and Dr. Zashmir Naik, Sambalpur University. No part of this thesis has formed the basis for the award of any degree or fellowship previously.

Srikanta kumar Tripathy

(Srikanta Kumar Tripathy)
School of Physics
Sambalpur University
Burla-768019,India
PhD Regn No: 159/2016/Phy

October 19, 2019

ACKNOWLEDGEMENTS

This is Fall, 2018 I am submitting my thesis after end of the journey started exactly seven years before in 2011, when I was searching for a topic to speak in my M.Sc Seminar. Constrains for topic was my special paper in Mastee degree, which was nuclear physics. And I was just faded of with few conventional topics like radioactive -decay, nuclear reactor/particle accelerator etc. It was Dr. Sunil Tripathy (faculty at IGIT, Sarang) who gave me a glimpse of RHIC and introduce with the physics with it. And I presented that in my seminar. Perhaps that was my first step or motivation to experimental high energy physics and I never looked back.

During final semester of Master degree, Prof S.N.Nayak (faculty at Sambalpur University) taught us particle physics. Honestly, the way he taught, clarity in expressing it and sound command over the subject, made certain impact on me. I recall asking him many silly question during his lecture; even, like is there any physical significance of coluor quantum number or they are just a mathematical abstract. To which my classmates asked me outside of class, that 'how come so many questions peep in your mind'. But, those classes were my steeping stone for this filed.

By Summer,2012 I have finished my Master degree and staying at Bhubaneswar with teaching in a undergraduate college. The plan was to prepare for competitive exams meant for PhD with some earning for a living. A day I received a call from Dr Z. Naik (faculty at Sambalpur University and co-supervisor of my PhD thesis) about openings at Institute of Physics, Bhubaneswar and urged to apply. Since this was a project position, for some un-certain period, so I was not sure about converting that to PhD. He then kindly agreed to do registration under him and I entered in that elite research institute. It's not that, things went smooth over time, but he stood behind me in every issue over the years.

It was Fall, 2012 I Joined in Institute of Physics, Bhubaneswar without any NET/GATE/JEST or such like competitive scores, which was a kind of mandatory to join such institutes in research programs. I just appeared an interview among with 20 odd candidates. It's kindness of Prof P.K.Sahu (faculty at Institute of Physics and supervisor of my PhD thesis), who have given me this scope. He was the person who provided me an official platform to start research. Months and years passed; he was continuously helping me, inspiring me and trying to build up the spirit 'you can do'. It was tough to start from scratch and do an entire new analysis in India, His expertise, both in theory and experiment, helped me to chose appropriate direction.

I came in contact with Prof B.Mohanty (faculty at NISER, Bhubaneswar) around high summer of 2013. Although I was not student of him, yet he was so kind enough to make me learn data analysis techniques and allowed me to interact with his group. I attended his group's weekly meeting and discussed with his students to a much minute details. Even from switching library in the code to checking farm job status in cell phones, I did learn a lot. I owe to him.

I was stuck with data analysis, for some miss-match with earlier published results. During fall of 2015, I came in contact with Prof Frank Geurts (faculty at Rice University, Texas). He was on his way to catch a train after a conference session, but he stopped and we discussed there. He kindly invited me to visit his institute and to collaborate with his group. For some constraints, although I could not visit, but we have started online group meetings. In a year or so, things were in place. Some jobs are still going on and hope that they will appear online soon.

During all these 'PhD' days, I spent fruitful discussions with many people, who shaped my thesis. They were with me all the times I spent with pursing my research. They were my friends, philosopher and guide through this journey.

Dr Rama Chandra Baral(Postdoc at NISER), Dr Mohammed Younus (Nelson Mandela University,South Africa), Dr Mriganka Mouli Mondal (Postdoc at NISER), Dr Deb Sankar Bhattacharya (Postdoc at University of Wurzburg, Germany), Dr Somnath Kar (Postdoc at CCNU, Wuhan), Dr Md Nasim (faculty at IISER, Berhampur), Dr Subhash Singha(Postdoc at Kent State University, Ohio), Dr Rihan Haque (Postdoc at Nikhef National institute for subatomic physics,Utrecht), Dr Ranbir Guleria (Scientific Officer, NISER), Dr Prasant Srivastav (Postdoc at IIT, Roopar), Dr Sandeep Chatarjee (faculty at IISER, Berhampur), Dr Chitrasen Jena(IISER, Tirupati),

Noor Alam(Phd scholar VECC, Kolkata), Dr Debojit Sarkar(Postdoc at Bose Institute), Arghya Chatarjee (Phd scholar VECC, Kolkata), Dr. Aditya Nath Mishra (Postdoc at UNAM,Mexico), Dr Santosh Kumar Das (faculty at IIT Goa), Dr Kalyan De (faculty at Bodoland University), Dr Shikshit Gupta, Dr Saikat Biswas (faculty at Bose Institute, Kolkata), Dr Neha Shah (faculty at IIT Patna),

Dr Prithwish Tribedy (Postdoc at Brookhaven National Labortory, NY), Dr Nihar Ranjan Sahoo (Texas A&M University, TX), Dr Rongrong Ma (Postdoc at Brookhaven National Labortory, NY), Dr James Daniel Brandenburg (Postdoc at Brookhaven National Labortory, NY), Dr David Tlusty (Rice University), Dr Pavol Federic (Nuclear Physics Institute, The Czech Academy of Sciences), Dr Kunsu OH(CCNU, Wuhan), Liwen Wen (University of California - LA), Daniel McDonald (Vice president at citizens bank, Rhode island), Prabhat Bhattarai (Research Scientist Position,UT Austin), Dr Zilong Chang (Postdoc at Brookhaven National Labortory, NY), Dr Christopher Flores (Data scientist at USAA).

If I missed some one, it's not purposefully, I wrote this just $\sim$ hours before submission. Don't worry, you are in my heart for sure.

'And in the end all I learned was how to be strong, alone!'

List of publications
(Part of thesis publications are in * mark)

Publication in peer reviewed journal

1. Production of D-mesons in p + p and p + Pb collisions at LHC energies
   By R.C.Baral, S.K.Tripathy, M.Younus, Z. Naik and P.K.Sahu
   Int. J. Mod. Phys. E 25, 1650092 (2016)

2. Azimuthal correlations of D-mesons in p+p and p+Pb collisions at LHC energies
   By M. Younus, S. K. Tripathy, P. K. Sahu and Z. Naik
   Eur. Phys. J. A (2017) 53: 112

3. * Application of Nilsson model for deformed nucleus in relativistic heavy ion collisions
   By S. K. Tripathy,M. Younus, P. K. Sahu and Z. Naik
   arXiv:1802.00639 [nucl-th], Under review

4. * Calculating charged particle observables using modified Wood Saxon model in HIJING for U+U collisions at 193 GeV
   By S. K. Tripathy,M. Younus, Z. Naik and P. K. Sahu
   Nuclear Physics A, 980, 81-90 (2018)

Publication in conference proceedings

1. Production of D-Mesons in p+p and p+Pb Collisions at LHC Energies
   Baral R.C., Tripathy S.K., Younus M., Naik Z., Sahu P.K.
   XXII DAE High Energy Physics Symposium. Springer Proceedings in Physics, vol 203, pp 809-811 (2018)

2. A Model Study of D-h Azimuthal Correlation at LHC Energies
   Tripathy S.K., Younus, M., Naik, Z. and Sahu P.K
   XXII DAE High Energy Physics Symposium. Springer Proceedings in Physics, vol 203, pp 793-794 (2018).

3. A model study of D-meson production at LHC energies
   R.C.Baral, S.K.Tripathy, M.Younus, Z. Naik and P.K.Sahu
   Proceedings of the DAE-BRNS Symp. on Nucl. Phys. 61 (2016) (E31)

4. A model study of D-h and D- (bar)D azimuthal correlation at LHC energies
   S.K. Tripathy,M. Younus,Z. Naik,P. K. Sahu
   Proceedings of the DAE-BRNS Symp. on Nucl. Phys. 61 (2016) E50.

5. * Strangeness Production in U+U collisions at RHIC
   Srikanta Kumar Tripathy for the STAR collaboration
   XXI DAE-BRNS High Energy Physics Symposium (2014) pp 177-1812 Springer Proceedings in Physics 174

6. Higher flow coefficients with STAR energy
   S K Tripathy,P K Sahu
   Proceedings of the DAE Symp. on Nucl. Phys. 58 (2013) E59

List of Collaboration Papers

1. Transverse spin transfer to Λ and $\bar{\Lambda}$ hyperons in polarized proton-proton collisions at $\sqrt{s_{NN}} = 200$ GeV
   J. Adam et al. (STAR Collaboration), e-Print: arXiv:1808.08000 [hep-ex]

2. Improved measurement of the longitudinal spin transfer to Λ and $\bar{\Lambda}$ hyperons in polarized proton-proton collisions at $\sqrt{s_{NN}} = 200$ GeV
   J. Adam et al. (STAR Collaboration), e-Print: arXiv:1808.07634 [hep-ex]

3. The Proton-Ω correlation function in Au+Au collisions at $\sqrt{s_{NN}}$=200 GeV
   J. Adam et al. (STAR Collaboration), e-Print: arXiv:1808.02511 [hep-ex]

4. Low -p_T e^+e^- pair production in Au+Au collisions at $\sqrt{s_{NN}} = 200$ GeV and U+U collisions at $\sqrt{s_{NN}} = 193$ GeV at STAR
   J. Adam et al. (STAR Collaboration), e-Print: arXiv:1806.02295 [hep-ex]

5. Longitudinal Double-Spin Asymmetries for Dijet Production at Intermediate Pseudorapidity in Polarized pp Collisions at $\sqrt{s} = 200$ GeV
   J. Adam et al. (STAR Collaboration),Phys. Rev. D 98, 032011, 2018

6. Longitudinal double-spin asymmetries for π^0s in the forward direction for 510 GeV polarized pp collisions
   J. Adam et al. (STAR Collaboration),Phys. Rev. D 98, 032013, 2018

7. J/ψ production cross section and its dependence on charged-particle multiplicity in p+p collisions at $\sqrt{s} = 200$ GeV
   J. Adam et al. (STAR Collaboration), e-Print: arXiv:1805.03745 [hep-ex]

8. Global polarization of Λ hyperons in Au + Au collisions at $\sqrt{s_{NN}}$ =200 GeV
   J. Adam et al. (STAR Collaboration), Phys. Rev. C 98, 014910, 2018

9. Beam energy dependence of rapidity-even dipolar flow in Au+Au collisions
   J. Adam et al. (STAR Collaboration), Physics Letters B, Volume 784, 2018, Pages 26-32

10. Correlation Measurements Between Flow Harmonics in Au+Au Collisions at RHIC
    J. Adam et al. (STAR Collaboration), e-Print: arXiv:1803.03876 [hep-ex]

11. Azimuthal anisotropy in Cu+Au collisions at $\sqrt{s_{NN}}$ =200 GeV
    L. Adamczyk et al. (STAR Collaboration), Phys. Rev. C 98, 014915, 2018

12. Transverse spin-dependent azimuthal correlations of charged pion pairs measured in $p\uparrow$ + ?p collisions at $\sqrt{s} = 500$ GeV L. Adamczyk et al. (STAR Collaboration), Physics Letters B, Volume 780, 2018, Pages 332-339

13. Measurement of the ${}^{3}_{\Lambda}$H lifetime in Au+Au collisions at the BNL Relativistic Heavy Ion Collider L. Adamczyk et al. (STAR Collaboration), Phys. Rev. C 97, 054909, 2018

14. Collision energy dependence of moments of net-kaon multiplicity distributions at RHIC L. Adamczyk et al. (STAR Collaboration), Physics Letters B, Volume 785, 2018, Pages 551-560

15. Beam-Energy Dependence of Directed Flow of$\Lambda, \bar{\Lambda}, K^{\pm}, K^{0}_{s}, and \phi$ in Au+Au Collisions L. Adamczyk et al. (STAR Collaboration), Phys. Rev. Lett. 120, 062301, 2018

16. Azimuthal transverse single-spin asymmetries of inclusive jets and charged pions within jets from polarized-proton collisions at $\sqrt{s}$ =500 GeV L. Adamczyk et al. (STAR Collaboration), Phys. Rev. D 97, 032004, 2018

17. Beam Energy Dependence of Jet-Quenching Effects in Au+Au Collisions at $\sqrt{s_{NN}}$=7.7, 11.5, 14.5, 19.6, 27, 39, and 62.4 GeV L. Adamczyk et al. (STAR Collaboration), Phys. Rev. Lett. 121, 032301, 2018

18. Coherent diffractive photoproduction of ρ_0 mesons on gold nuclei at 200 GeV/nucleon-pair at the Relativistic Heavy Ion Collider L. Adamczyk et al. (STAR Collaboration), Phys. Rev. C 96, 054904 , 2017

19. Measurements of jet quenching with semi-inclusive hadron+jet distributions in Au+Au collisions at $\sqrt{s_{NN}}$=200 GeV L. Adamczyk et al. (STAR Collaboration), Phys. Rev. C 96, 024905, 2017

20. Harmonic decomposition of three-particle azimuthal correlations at RHIC L. Adamczyk et al. (STAR Collaboration), e-Print: arXiv:1701.06496 [nucl-ex]

21. Constraining the initial conditions and temperature dependent transport with three-particle correlations in Au+Au collisions L. Adamczyk et al. (STAR Collaboration),e-Print: arXiv:1701.06497 [nucl-ex]

22. Measurement of D^0 Azimuthal Anisotropy at Midrapidity in Au+Au Collisions at $\sqrt{s_{NN}}$=200 GeV L. Adamczyk et al. (STAR Collaboration), Phys. Rev. Lett. 118, 212301, 2017

23. Global Lambda hyperon polarization in nuclear collisions: evidence for the most vortical fluid L. Adamczyk et al. (STAR Collaboration), Nature 548 (2017) 62

24. Measurement of the cross section and longitudinal double-spin asymmetry for dijet production in polarized pp collisions at $\sqrt{s}$=200 GeV L. Adamczyk et al. (STAR Collaboration), Phys. Rev. D 95, 071103(R) , 2017

25. Dijet imbalance measurements in Au+Au and pp collisions at $\sqrt{s_{NN}}$=200 GeV at STAR L. Adamczyk et al. (STAR Collaboration), Phys. Rev. Lett. 119, 062301 , 2017

26. Υ production in U + U collisions at $\sqrt{s_{NN}}$=193 GeV measured with the STAR experiment L. Adamczyk et al. (STAR Collaboration), Phys. Rev. C 94, 064904, 2016

27. Charge-Dependent Directed Flow in Cu+Au Collisions at $\sqrt{s_{NN}}$=200 GeV L. Adamczyk et al. (STAR Collaboration), Phys. Rev. Lett. 118, 012301, 2017

28. Energy dependence of J/ψ production in Au + Au collisions at $\sqrt{s_{NN}}$ = 39, 62.4 and 200 GeV L. Adamczyk et al. (STAR Collaboration), Physics Letters B, Volume 771, 2017, Pages 13-20

29. Direct virtual photon production in Au+Au collisions at $\sqrt{s_{NN}}$ = 200 GeV L. Adamczyk et al. (STAR Collaboration), Physics Letters B, Volume 770, 2017, Pages 451-458

30. Jet-like correlations with direct-photon and neutral-pion triggers at $\sqrt{s_{NN}}$ = 200 GeV L. Adamczyk et al. (STAR Collaboration), Physics Letters B, Volume 760, 2016, Pages 689-696

31. Near-side azimuthal and pseudorapidity correlations using neutral strange baryons and mesons in d+Au, Cu + Cu, and Au + Au collisions at $\sqrt{s_{NN}}$ =200 GeV B. Abelev et al. (STAR Collaboration),Phys. Rev. C 94, 014910, 2016

32. J/ψ production at low transverse momentum in p+p and d + Au collisions at $\sqrt{s_{NN}}$=200 GeV L. Adamczyk et al. (STAR Collaboration), Phys. Rev. C 93, 064904, 2016

33. The $\phi(1020) \rightarrow e^+e^-$ meson decay measured with the STAR experiment in Au+Au collisions at $\sqrt{s_{NN}}$ = 200 GeV L. Adamczyk et al. (STAR Collaboration) e-Print: arXiv:1503.04217 [hep-ex]

34. Measurement of elliptic flow of light nuclei at $\sqrt{s_{NN}}$=200, 62.4, 39, 27, 19.6, 11.5, and 7.7 GeV at the BNL Relativistic Heavy Ion Collider L. Adamczyk et al. (STAR Collaboration), Phys. Rev. C 94, 034908, 2016

35. Beam Energy Dependence of the Third Harmonic of Azimuthal Correlations in Au+Au Collisions at RHIC L. Adamczyk et al. (STAR Collaboration),Phys. Rev. Lett. 116, 112302, 2016

36. Measurement of the Transverse Single-Spin Asymmetry in $p\uparrow + p \rightarrow W\pm/Z^0$ at RHIC L. Adamczyk et al. (STAR Collaboration),Phys. Rev. Lett. 116, 132301, 2016

37. Centrality dependence of identified particle elliptic flow in relativistic heavy ion collisions at $\sqrt{s_{NN}}$=7.7?62.4 GeV L. Adamczyk et al. (STAR Collaboration),Phys. Rev. C 93, 014907, 2016

38. Measurement of interaction between antiprotons L. Adamczyk et al. (STAR Collaboration),Nature volume 527, pages 345-348,2015

39. Centrality and Transverse Momentum Dependence of Elliptic Flow of Multistrange Hadrons and ϕ Meson in Au+Au Collisions at $\sqrt{s_{NN}}$=200 GeV L. Adamczyk et al. (STAR Collaboration),Phys. Rev. Lett. 116, 062301, 2016

40. Beam-energy dependence of charge balance functions from Au + Au collisions at energies available at the BNL Relativistic Heavy Ion Collider L. Adamczyk et al. (STAR Collaboration),Phys. Rev. C 94, 024909, 2016

41. Probing parton dynamics of QCD matter with Ω and ϕ production L. Adamczyk et al. (STAR Collaboration),Phys. Rev. C 93, 021903(R), 2016

42. Azimuthal Anisotropy in U+U and Au+Au Collisions at RHIC L. Adamczyk et al. (STAR Collaboration), Phys. Rev. Lett. 115, 222301, 2015

43. Observation of Charge Asymmetry Dependence of Pion Elliptic Flow and the Possible Chiral Magnetic Wave in Heavy-Ion Collisions L. Adamczyk et al. (STAR Collaboration), Phys. Rev. Lett. 114, 252302, 2015

44. Measurements of dielectron production in Au + Au collisions at $\sqrt{s_{NN}}$=200 GeV from the STAR experiment L. Adamczyk et al. (STAR Collaboration), Phys. Rev. C 92, 024912, 2015

45. Observation of Transverse Spin-Dependent Azimuthal Correlations of Charged Pion Pairs in $p\uparrow + p$ at $\sqrt{s}$=200 GeV L. Adamczyk et al. (STAR Collaboration), Phys. Rev. Lett. 115, 242501, 2015

46. Long-range pseudorapidity dihadron correlations in d + Au collisions at $\sqrt{s_{NN}}$=200 GeV L. Adamczyk et al. (STAR Collaboration), Physics Letters B, Volume 747, 2015, Pages 265-271

47. Energy dependence of acceptance-corrected dielectron excess mass spectrum at mid-rapidity in Au+Au collisions at $\sqrt{s_{NN}}$=19.6 and 200 GeV L. Adamczyk et al. (STAR Collaboration), Physics Letters B, Volume 750, 2015, Pages 64-71

48. Effect of event selection on jetlike correlation measurement in d + Au collisions at $\sqrt{s_{NN}}$=200 GeV L. Adamczyk et al. (STAR Collaboration), Physics Letters B, Volume 743, 2015, Pages 333-339

49. Energy dependence of $K\pi$, $p\pi$, and Kp fluctuations in Au + Au collisions from $\sqrt{s_{NN}}$=7.7 to 200 GeV L. Adamczyk et al. (STAR Collaboration),Phys. Rev. C 92, 021901(R), 2015

50. Di-hadron correlations with identified leading hadrons in 200 GeV Au + Au and d + Au collisions at STAR L. Adamczyk et al. (STAR Collaboration), Physics Letters B, Volume 751, 2015, Pages 233-240

51. Isolation of flow and nonflow correlations by two- and four-particle cumulant measurements of azimuthal harmonics in $\sqrt{s_{NN}}$ = Au+Au collisions L. Adamczyk et al. (STAR Collaboration), Physics Letters B, Volume 745, 2015, Pages 40-47

52. Charged-to-neutral correlation at forward rapidity in Au + Au collisions at $\sqrt{s_{NN}}$=200 GeV L. Adamczyk et al. (STAR Collaboration), Phys. Rev. C 91, 034905, 2015

53. $\Lambda\Lambda$ Correlation Function in Au+Au Collisions at ?sNN=200GeV L. Adamczyk et al. (STAR Collaboration), Phys. Rev. Lett. 114, 022301, 2015

54. Elliptic flow of electrons from heavy-flavor hadron decays in Au+Au collisions at $\sqrt{s_{NN}}$= 200, 62.4, and 39 GeV L. Adamczyk et al. (STAR Collaboration) Phys. Rev. C 95, 034907, 2017

Contents

List of Tables

List of Figures

Chapter 1

Introduction to Heavy Ion Collision and Strangeness

1.1 Quarks, Gluons and Plasmas

To answer bizarre patterns of hadrons fit into (eightfold way), Gell-Mann [1] and Zweig [2] in 1964 proposed that hadrons further composed of more elementary constituent ('quark' by Gell-Mann and 'aces' by Zweig). The approach had three quarks (u, d, s and their anti-particles), of which baryons are made of three and mesons of two quarks. These were proposed to have non-integral value of charge and spin-half particles.

Thus three quarks are a symmetric state, in contradiction with, what one would expect from the Pauli exclusion principle. Greenberg in 1964 [3] proposed possibility of fixing up the quark statistics by assuming, quarks obey para fermi statistics of order three. The order of the parastatistics for quarks in baryons is uniquely fixed by the two requirements that the three quarks be in a symmetric state and that the proton and other baryons not have any additional degeneracy besides the known spin degeneracy [4]. Nambu and Han in 1965 [5, 6] explicitly introduced the color SU(3) symmetry, which in fact is implicit in the parastatistics model. One of their motivations was to avoid fractional quark charges, so these are arranged for their three flavor triplets to have different electric charge, so that these are distinguishable. Averaging over the charges for each flavor gives the fractional charges of the original quark model [4].

Evidence for gluons, however, remained circumstantial. First indication probably came from the data on lepton nucleon scattering [7]. Momentum sum rule of the nucleon structure functions, was not saturated by the quarks and antiquarks [8, 9, 10, 11]. This suggests that half of nucleon's momentum must be carried by flavorless parton constituents, presumably gluons [12].

In 1972, Friedman, Kendall and Taylor, using SLAC-MIT experiment (deep inelastic electron scattering; $e + p \rightarrow e + X$, where X is not necessarily a proton) have shown that, the incident electron loses a large part of its original energy and emerges at a large angle in relation to the original direction [13]. The scattering of electrons at large angles was explained as, the existence of inner nucleonic structure, called partons [14, 15]. In Fig. 1.1, it is shown interior view of end station A of SLAC-MIT experiment, showing fixed-target area and spectrometer. Here the scattered electrons from hydrogen target and detected outgoing electrons in a large magnetic spectrometer are shown.

Figure 1.1: Equipment used in the SLAC - MIT deep inelastic scattering experiment 1967, where quarks were discovered taken from Ref [16].

In 1975, different phase of vacuum was proposed, where quarks are not confined. Collins and Perry argued that [17] since the interaction between quarks weakens as quarks get closer at sufficiently high density, these quarks are no longer confined inside the hadrons and become free. The superdense matter at densities higher than the nuclear one consists of a quark soup. Cabibbo and Parisi [18] re-interpreted the existence of the Hagedorn limiting temperature TH as a signal of a second-order phase transition between the hadronic and quark-gluon phases of matter [19].

In 1978, PLUTO collaboration at DORIS (Double Orbit Intersecting Storage Ring) demonstrated that [20] the event shapes $e^+e^- \to \gamma(1S) \to hadrons$, differed significantly from those in the nearby e^+e^- off-resonance continuum. This was a hint towards a possible three -gluon decay mechanism of the $\gamma(1S)$ as expected in QCD [21, 22, 23]. In 1979, PLUTO collaboration at PETRA (Proton Electron Tandem Ring Accelerator) showed [24, 25] a two -jet decay of $\gamma(1S)$ could be excluded while a three-gluon decay model based on the decay distribution predicted from QCD convoluted with hadronization.

It may be worthwhile to mention that, PETRA collider had four interaction regions in which the electrons and positrons met and detectors could be installed; CELLO, JADE, MARK-J and TASSO (Two Arm Spectrometer SOlenoid). As CELLO faced with a delay of the cryogenics for its superconducting magnet, so in place of that, PLUTO was installed [7]. PLUTO at DORIS have CMS energy up to 10 GeV, while at PETRA, it was upgraded up to 48 GeV CMS energy [26]. Both, PETRA and DORIS, are/were part of DESY facility.

PETRA cite is shown, in Fig 1.2. Construction of the experiment went in 1976-78. First stored beam was successful in July 1978.

(a) PETRA experiment cite, taken from Ref [27].

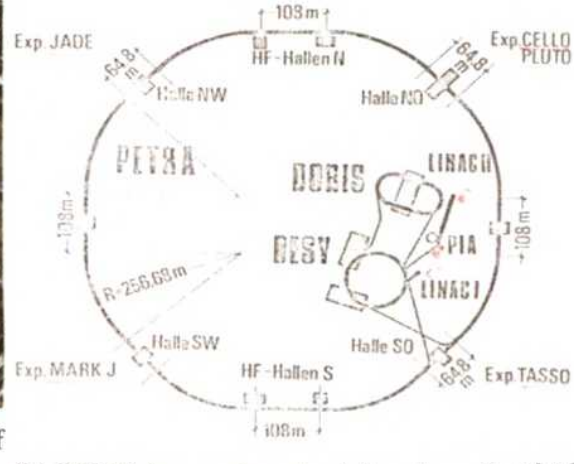

(b) PETRA experiments, taken from Ref [28]

Figure 1.2: PETRA facility and PLUTO experimental cite, where gluon was discovered.

Quite a few years after, in 2000, CERN announced circumstantial evidence of,

Table 1.1: Properties of quarks and gluons [34]

Name(Symbol)	Mass(MeV)	Charge	Quantum Number
Up (u)	$2.2^{+0.6}_{-0.4}$	$+\frac{2}{3}$	Isospin = $+\frac{1}{2}$
Down (d)	$4.7^{+0.5}_{-0.4}$	$-\frac{1}{3}$	Isospin = $-\frac{1}{2}$
Strange (s)	96^{+8}_{-4}	$-\frac{1}{3}$	Strangeness = -1
Charm (c)	1027 ± 0.03	$+\frac{2}{3}$	Charm = +1
Bottom (b)	$4018^{+0.04}_{-0.03}$	$-\frac{1}{3}$	Bottom = -1
Top (t)	173000.21 ± 0.51	$+\frac{2}{3}$	Top = +1

plasma of quarks and gluons, for the first time in laboratory [29, 30]. Some of the results include J/ψ suppression from NA50 Collaboration [31], enhancement of strange particle yield by NA49 collaboration [32]. Five years later, in 2005, RHIC announced creation of QGP [33]. Interestingly, it showed, QGP instead of behaving like a gas, it behaves more like a liquid - a 'perfect' liquid with virtually no viscosity, or resistance to flow.

Current understanding of quarks and gluons are presented in Tab. 1.1.

QCD Lagrangin may be written as [35, 36]:

$$L_{QCD} = \sum_q \bar{\psi}_q (i\gamma^\mu D_\mu - m_q)\psi_q - \frac{1}{4} G^a_{\mu\nu} G^{a\mu\nu}. \tag{1.1}$$

Where q = quark flavors (u,d,s,c,b,t),

$G^a_{\mu\nu} = \delta_\mu A^a_\nu - \delta_\nu A^a_\mu - g f^{abc} A^b_\mu A^c_\nu$

and $D_\mu = \delta_\mu + igA^a_\mu T^a$.

The generators (T^a) and the SU(3) structure constants (f^{abc}) fulfill the relation:

$$[T^a, T^b] = i f^{abc} T^c. \tag{1.2}$$

QCD running coupling constant may be written as [37]:

$$\alpha_s(Q^2) = \frac{4\pi}{\beta_0 ln \frac{Q^2}{\Lambda^2_{QCD}}}. \tag{1.3}$$

In the Fig. 1.3, a variation of α_s with Q is shown. At high momentum transfer

between quarks and gluons ($Q^2 >> \Lambda_{QCD}$), the coupling strength approaches to zero and thus quarks behave like free particles. This is known as Asymptotic Freedom. These are referred as hard processes and dealt with perturbative QCD approach. It was first proposed by David Gross, David Politzer and Frank Wilczek in 1975 [38, 39].For low momentum transfers ($Q^2 << \Lambda_{QCD}$), coupling strength becomes large. It is the reason for partons being never seen in free state and the state is refered as confinement. These are soft processes and dealt with Non-perturbative QCD approaches.

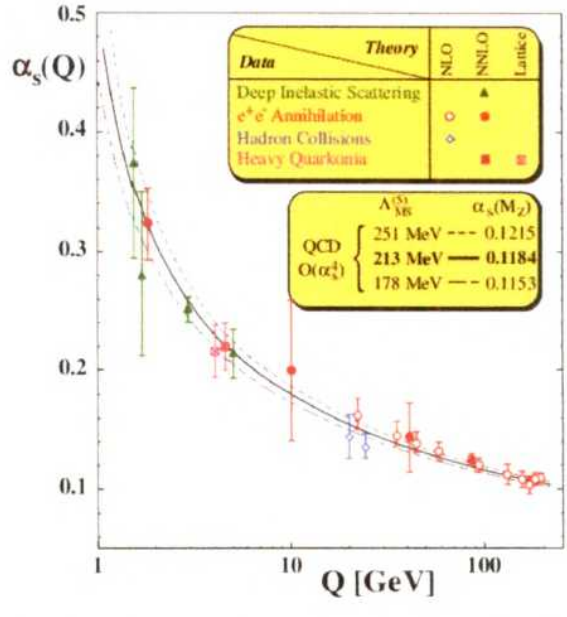

Figure 1.3: Coupling constant α_s as a function of momentum transfer Q, taken from Ref [40].

De-confinement of quarks and gluons can be argued, if they can move over of the size of a hadron (~1 fm). It may happen in two scenarios.

1. Asymptotic freedom (high temperature),

2. Debye screening (high compression).

For asymptotically free case, energy density and temperature is related by the following relation:

$$\frac{\epsilon}{T^4} = (16 + \frac{21}{2} n_f) \frac{\pi^2}{30}, \tag{1.4}$$

where n_f is the number of quark flavor [41, 42]. The lattice QCD proposes existence

of a critical point ($T_c \sim 154$ MeV and $\epsilon \sim 1$ GeV/fm^3), where phase transition occurs from confined hadronic matter to de-confined state of quarks and gluons [43, 44]. It also predicts a smooth crossover between hadron and quark phases [45]. At high temperature (T) and small baryon chemical potential (μ_B) [46], reverse to this, for small T and large μ_B, a first order phase transition may possible betwen these phases [47]. We have shown a reference plot in this regard in Fig. 1.4.

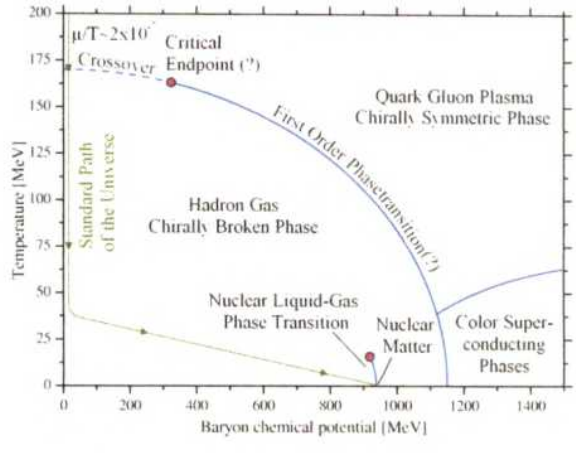

Figure 1.4: QCD-phase diagram, which shows transition from hadron to quark phase, taken from Ref. [48].

In Debye screening case, high compression of hadronic matter (separation between hadrons < 1fm) lead partons among hadrons interact with each other. As a consequence, it is highly unlike then, to categorise partons as localised inside hadrons, so de-confinement is possible. Debye screened quarks might be characterised by non-perturbative QCD phenomenon.

1.2 Heavy-ion Collisions and production of QGP

In order to investigate these type of extremely high temperature and density conditions, system should behave like matter, not like particles. $p+p$ or $e^+ + e^-$ collisions gives a few particles to fulfil such conditions, which heavy nuclei also do. Indeed, a paper published in Ref [49] shows that T and μ_B can actually varied in collider experiments involving heavy-ions. Results from that analysis is shown in Fig 1.5 says that, with increasing of collision energy, chemical potential decreases. Contrary

with this, the temperature increases strongly at first, and around $\sqrt{s_{NN}} = 10$ GeV, it forms plateaue.

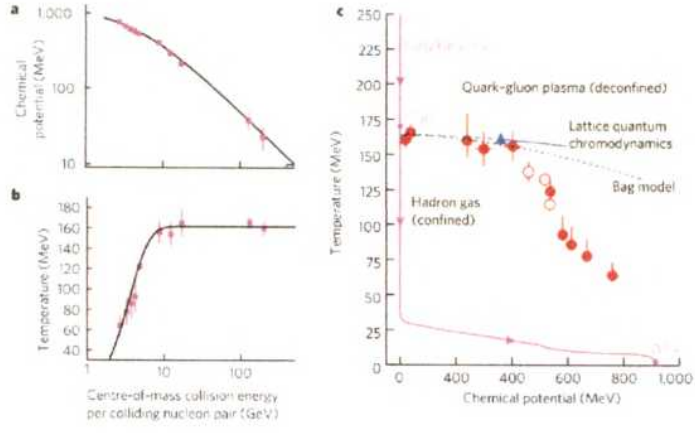

Figure 1.5: Energy dependence of chemical potential and temperature, taken from Ref [49].

To achieve this, experiments collide ions travelling with relativistic speed. The loss of kinetic energy due to such type of collisions, leads to the creation of fireball. If this is hot or compress enough as discussed in earlier sections, this may form QGP. Since all this energy is manifested to produce particles, so it can be related produced particles' multiplicity [50]. This may be written as [51]:

$$\epsilon = \frac{m_T}{\tau_0 A} \frac{dN}{dy}\Big|_{y=0}, \tag{1.5}$$

where τ_0 is the proper time at which QGP is expected to be formed, $\sim$ 1fm/c.

For Au+Au 130 GeV, assuming only pions are produced, estimated energy density will be $\sim$ $2.9 GeV/fm^3$ [52], which is higher than one required to produce QGP.

The Fig 1.6 shows space-time evolution of fireball in nucleus collision, both for hadron and quark phase. As shown in the figure, the fireball created aftermath collisions, expands due to pressure gradients. After cooling down below critical temperature T_C, quarks and gluons forms hadron gas. On further expansion of hadron gas, in-elastic collision ceases, which no more allows formation of new particles. This is referred as chemical freeze out temperature (T_{ch}). From this stage, chemical component of the system will remain unchanged. On further expansion of

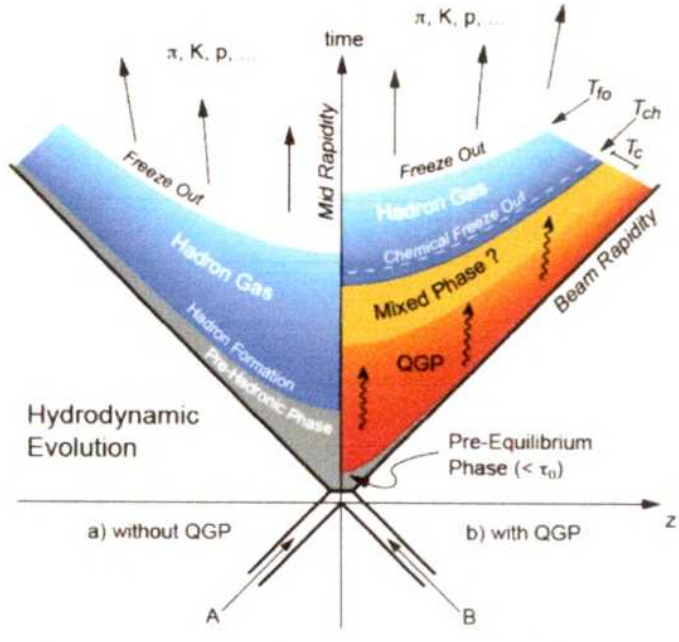

Figure 1.6: Space time evolutions with and without QGP are pointed out, taken from Ref [53].

fireball, elastic collisions will eventually cease at thermal freeze-out (T_{fo}). What we observe at detectors, is particles after this stage.

To experimentally establish, that QGP is indeed created in collider experiments, one could look for various signatures. Few of these are:

1. Quarkonia suppression

   At high densities, Debye screening (color charge of a quark is subject to screening due to presence of gluons and other quark-anti quarks) in a quark-gluon plasma reduces the range of the attractive force between heavy quarks and antiquarks (quarkonium is a bound state of a heavy quark and its own anti-quark) [98], and above some critical density screening prevents the formation of bound states. The large bound states are expected to dissolve before the smaller ones as the temperature of the system increases [54].

   The result for different charmonium and bottomonium states is shown in Fig. 1.7-a. In Fig. 1.7-b nuclear modification factor shown for J/psi for Pb-Pb collisions at $\sqrt{s_{NN}}$ 2.76 and 5.02 TeV; along with results from Au-Au collisions at 0.2 TeV.

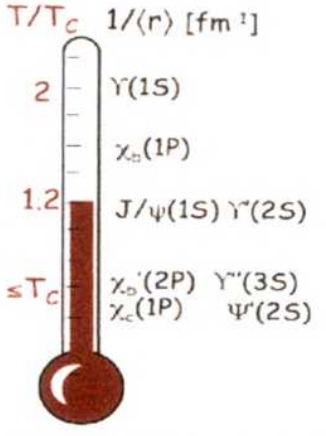

(a) The QGP thermometer, taken from [55].

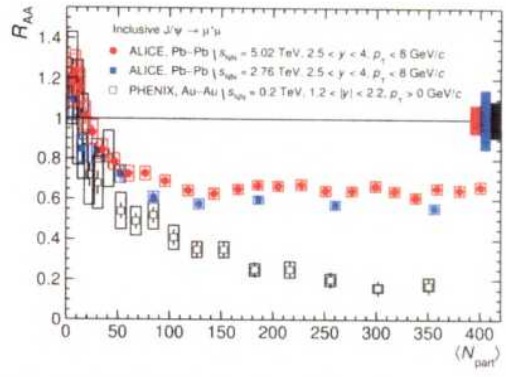

(b) J/psi RAA as a function of centrality measured by the PHENIX and ALICE at experiment, taken from [56].

Figure 1.7: Quarkonia suppression results from RHIC and LHC facility

2. Electro-magnetic probes (Dileptons & direct photons)

   A hot and dense medium should emit thermal radiations [57]. For direct photons (produced in the initial hard parton-parton scattering) $1 < p_T < 3$ GeV, partonic phase was predicted to be the dominant source [58]. The dominant processes for photon production in QGP are the annihilation ($q\bar{q} \rightarrow g\gamma$) and Compton processes ($q(\bar{q}) \rightarrow q(\bar{q})\gamma$) [59]. However disadvantage with direct photons is the substantial background from various processes (thermal and non-thermal).

   Dileptons (lepton pairs, e^+e^- *and* $\mu^+\mu^-$) have an advantage over direct photons, as the mass of the meson which decayed into the lepton pair can be calculated. It was proposed that [60] with presence of quark matter, there would be an enhancement of dileptons of approximately an order of magnitude in the mass region between 200 MeV and 600 MeV.

   Fig. 1.8 shows dilepton decays compared to the dilepton invariant mass spectra.

3. Strangeness enhancement

   If matter went through a phase transition to a QGP, then there would be an enhancement of strange particles in the final state [62]. This enhancement is relative to a collision system, where a transition to a QGP phase does not take

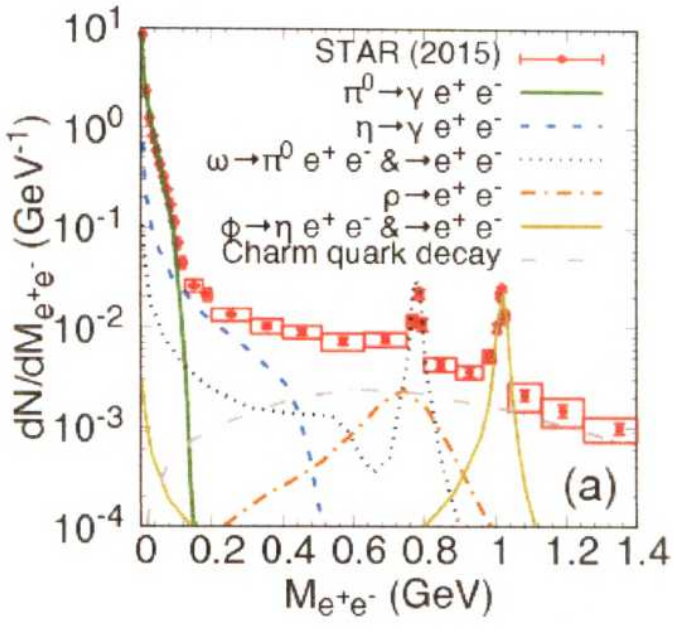

Figure 1.8: Hadronic and charm quark dilepton decays compared to the dilepton invariant mass spectra , taken from Ref [61].

place, such as p+p or p+A collisions where the system size is very small.

The strangeness enhancement factor is defined as the ratio of yield of a strange particle per participating nucleon in the heavy ion collisions to that in pp collisions.

$$E(i) = \frac{(Yield/N_{part})^{AA}}{(Yield/N_{part})^{NN}} \tag{1.6}$$

Fig. 1.9 shows strangeness enhance factor as a function of average number of nucleons from different experiments.

4. Elliptic flow

In non-central collisions, the reaction zone is asymmetric [53]. Interactions among constituents of the system, generates a pressure gradient, which is large in one direction and small in the other [64]. Thus, this initial spatial anisotropy is then transformed into momentum anisotropy. The elliptic flow (v2) is a measure of the anisotropy in momentum space [65, 66].

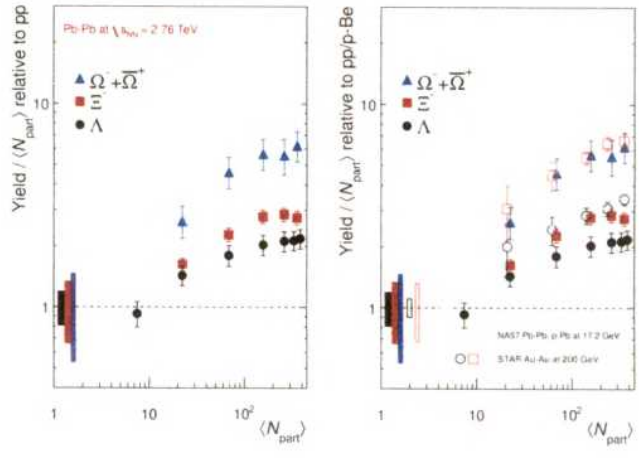

Figure 1.9: Strangeness enhancement as a function of mean number of participating nucleons from ALICE, SPS and RHIC, taken from Ref [63].

Azimuthal distribution may be characterised by the following equation:

$$\frac{dN}{d\phi} \propto 1 + \sum_{n=1}^{\infty} 2v_n cos[n(\phi - \psi)], \tag{1.7}$$

where ϕ is the azimuthal angle.

Fig. 1.10 shows elliptic flow scaled by number of constituent as a function of transverse momentum scaled by number of constituent for different particles.

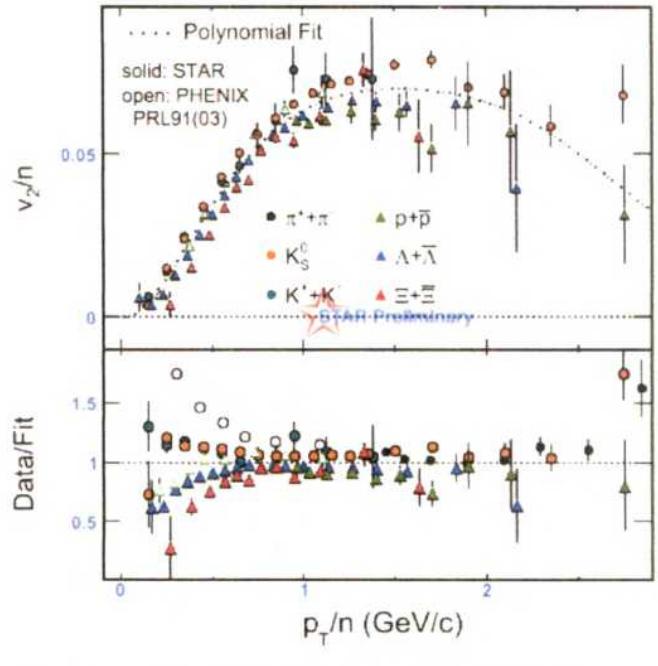

Figure 1.10: NCQ scaling of elliptic flow from RHIC facility, taken from Ref [67].

5. Nuclear Modification factor

Nuclear Modification factor is the ratio of yield in heavy ion collision to that in proton-proton collisions, normalised to binary nucleon-nucleon collisions.

$$R_{AA} = \frac{1}{T_{AA}} \times \frac{(d^2N/dp_T dy)_{AA}}{(d^2N/dp_T dy)_{pp}} \tag{1.8}$$

Where $T_{AA} = < N_{coll} > /\sigma_{NN}$, σ_{NN} is inelastic pp cross-section.

If the nucleus-nucleus collision is a simple superposition of nucleon-nucleon collision, then the value of R_{AA} should be unity. If it's value is less than unity then it will indicate the effect of strongly interacting matter produced in heavy ion collisions.

Fig. 1.11 shows nuclear modification factors for charged hadrons from RHIC BES data.

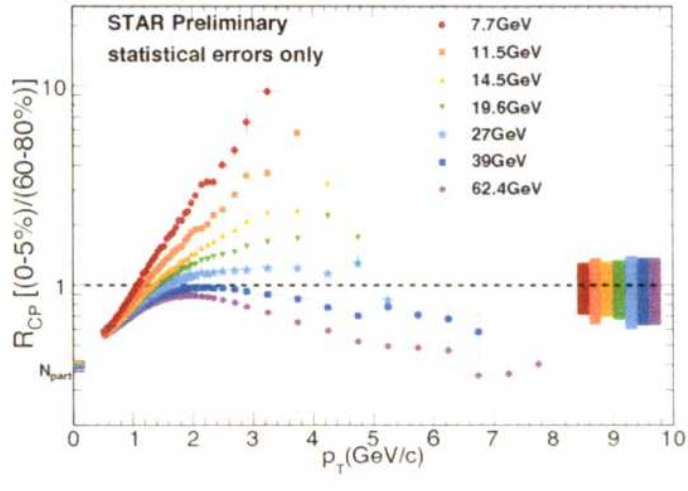

Figure 1.11: The nuclear modification factor as a function of the transverse momentum from STAR experiment, taken from Ref [68].

6. Hard probes (Jet quenching)

   If two jets are created near the fireball edge, one will be emitted away from the fireball and the other pass through the medium and will appears on the other side [51, 53]. This is true in p+p and d+Au collisions, but not for Au+Au collisions. Here the jet is completely quenched, i.e. it looses all its energy while traversing in the dense medium. The asymmetry in the dijet production is the signatures of the formation of a QGP.

Dihadron azimuthal correlations may be used to observe jets in high energy collisions [53].

Fig. 1.12 shows near and away side jet from heavy ion collision and elementary pp collisions.

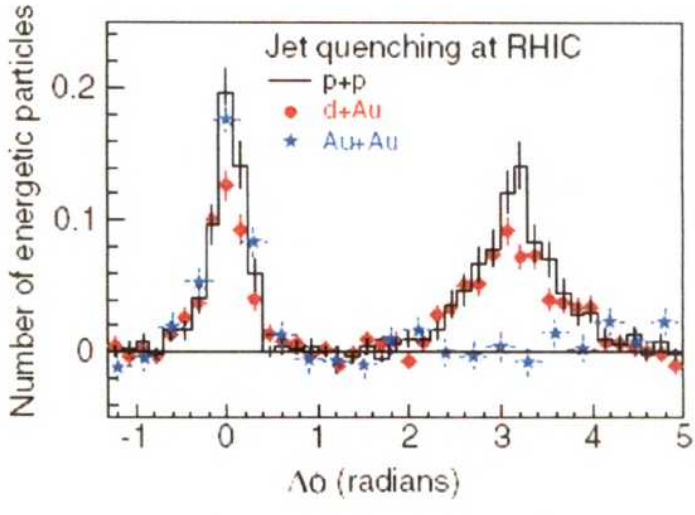

Figure 1.12: jet particles are observed at $\delta\phi = \pi$ opposite a trigger particle at $\delta\phi = 0$ in p + p and d + Au collisions but are completely absent in Au + Au collisions. , taken from Ref [69].

This thesis work is based on the one of these, i.e. strangeness enhancement.

1.3 Strangeness as a signature of QGP

A paper in 1982 [70], suggests that the dominant process for the production of strange quarks in the quark gluon plasma is gluonic fusion. Chemical equilibration of strange quarks formed in such a medium happens faster than it would be the situation in hadronic scenario .

Strangeness production channels in hadronic scenario are [71]:

$$\pi + N \rightarrow \Lambda + K$$
$$\pi + \bar{N} \rightarrow \bar{\Lambda} + \bar{K}$$
$$N + N \rightarrow N + \Lambda + K^{+}$$
$$\pi + \pi \rightarrow K + \bar{K}$$
$$N + N \rightarrow N + N + \Lambda + \bar{\Lambda}.$$

Where N represents nucleons.

And that in partonic scenario are [72]:

$$\bar{q} + q \rightarrow \bar{s} + s$$
$$\bar{g} + g \rightarrow \bar{s} + s.$$

Q-value corresponds for partonic scenario, is the current masses of a strange quark anti-quark pair ($2m_s \approx 200$ MeV) [73], whereas for hadronic case the smallest is $\sim$ 540 MeV. So, once plasma of quarks and gluons are formed, strangeness will be generated more and more.

Another direction is about equilibration time. In ideal gas of quarks and gluons; equilibration time is $\tau_{eq} \approx 10fm$ [62], which is order of the total duration of a heavy ion reaction. As QGP time span is shorter than this, partonic processes might not be sufficient to drive the system to a complete chemical equilibrium [74]. Way around, in a gas of free hadrons, particles with strangeness, chemical equilibrium might attainable after $\tau_{eq} \approx 30fm$ [70]. Also multi-strange production in hadron-gas scenerio, will be difficult to be produced in large abundances.

Early experimental attempts to verify this, begun around in 1990. Few publications [75, 76, 77] shows enhanced strangeness production (for K and Λ) relative to pion production - compared to elementary p+p or p+A collisions. However, as mentioned earlier single strangeness produciton in nucleus-nucleus collision, may be

3297

interpreted in terms of hadron resonance gas, these do not prove unambiguously as a signature of QGP. Probably, first experimental result from multi-strange hadron came from WA85 Collaboration [78]. They have shown enhanced Ξ production in S+W system, compared to p+W system.

Fig. 1.13 shows strange particle enhancement in Pb+Pb collisions relative to p+Be collisions from NA57 experiment [79]. As one can observe, for S=1 (Λ), enhancement values is 3-4, while same is $\sim$ 10 for S=2 (Ξ) and $\sim$ 20 for S=3 (Ω). This pattern is expected if there is a full chemical equilibrium for a large system [80]. This is also sign for fast partonic equilibration in a QGP [62, 81, 70].

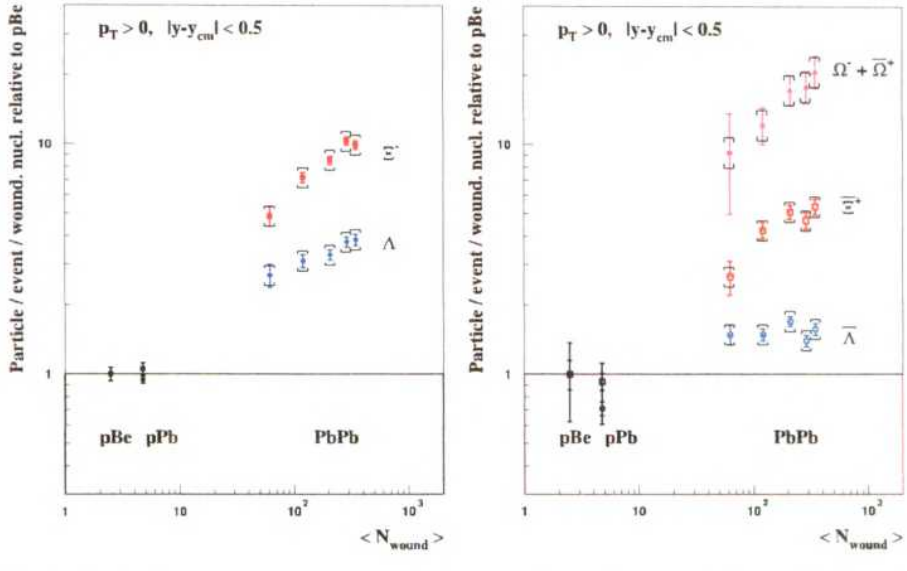

Figure 1.13: Hyperon enhancements as a function of the number of wounded nucleons. , taken from Ref [79].

During the course of time, we were able to explore strangeness more elaborately. Some results are; system size, energy [82] and multiplicities [83] dependence of strange quark yield , hierarchy of s-quarks content, correlation in between strange particles [84], elliptic flow of strange particles [85] and so on.

Although QGP leads to strangeness enhancement, but the reverse does not imply in certain. A study published in Ref [86] proposes the idea of anti-hyperon production by multi-mesonic reactions, as one of the reason. Alternative ideas of canonical suppression of strangeness have been proposed to be a source of strangeness enhancement in small systems (proton-proton) [87]. A recent experimental publica-

tion [88] shows enhanced production of multi-strange hadrons in high-multiplicity proton-proton collisions.

There are indications of strangeness enhancement in p+A collisions, relative to pp (scaled by N_{part}) [89, 90]. This may not be explained by a QGP formation, since the created fireball is too small, and it is not sufficient to explain the enhancement in A + A. As a consequence of this is, the measured enhancement in A + A will be less, if p + A is used as baseline instead of p + p [74].

1.4 Scope and Organisation of the thesis

This thesis aims to answer some un-solved questions at top RHIC energy from strangeness point of view.

STAR collaboration published results on nuclear modification factor [62, 70] for single and multi-strange hadrons. These results as shown in Fig. 1.14, do not address whether particles and anti-particles are suppressed equally in QGP. This will be addressed in this thesis work.

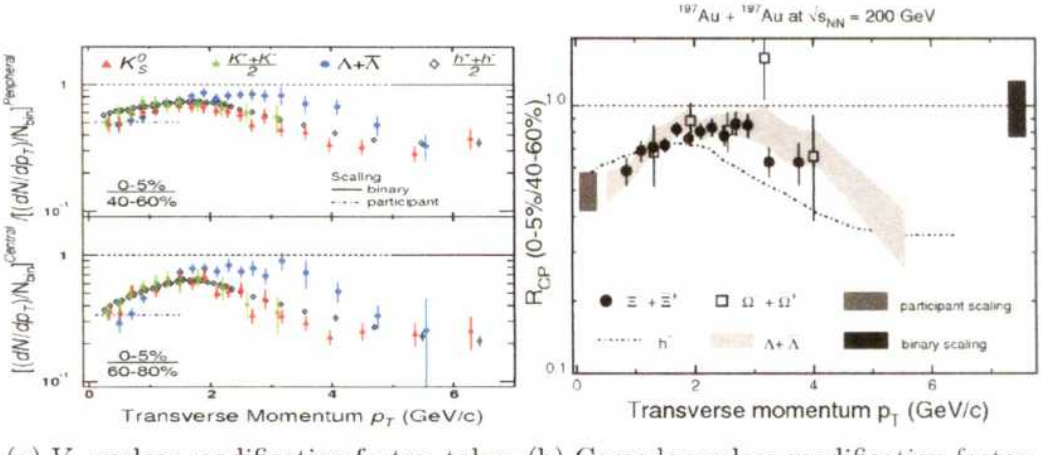

(a) V_0 nuclear modification factor, taken from [91]

(b) Cascade nuclear modification factor, taken from [70]

Figure 1.14: Nuclear modification factor of strange hadrons from STAR experiment of RHIC

Another study reported in Ref [92] shows single-strange anti-baryon to baryon measurement in in most central collision. It neither says any centrality dependence nor it addresses dependence on strangeness content of this ratio. Fig. 1.15 may be

referred in this regard. This will be addressed in this thesis.

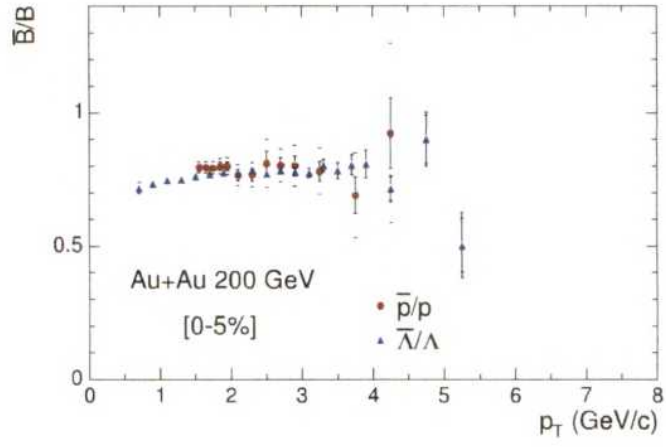

Figure 1.15: Anti-baryon to baryon ratio ($\bar{\Lambda}/\Lambda$) at Au+Au 200 GeV most central collision, is taken from Ref [92].

At similar colliding energies, U+U collisions are expected to have larger energy density [93] and higher number of produced particles than in the case of Au+Au or Pb+Pb collisions [94]. This makes U+U system to be an unique platform for testing various observables. We'll compare results from deformed nucleus , U with results from spherical nucleus collision, Au.

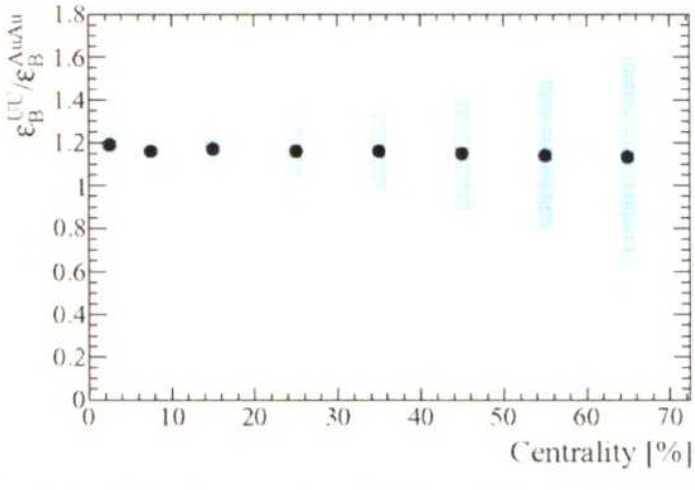

Figure 1.16: The ratio of Bjorken energy densities in U + U and Au+Au collisions as a function of centrality, taken from Ref [93].

As U nuclei is prolate deformed, so it may undergo different configurations during collision. Few such are shown in Fig. 1.17. This makes U nuclei an interesting platform to study configuration dependence of observables. We plan to implement

shape deformation in Monte Carlo simulation models and study the effects of shape deformation.

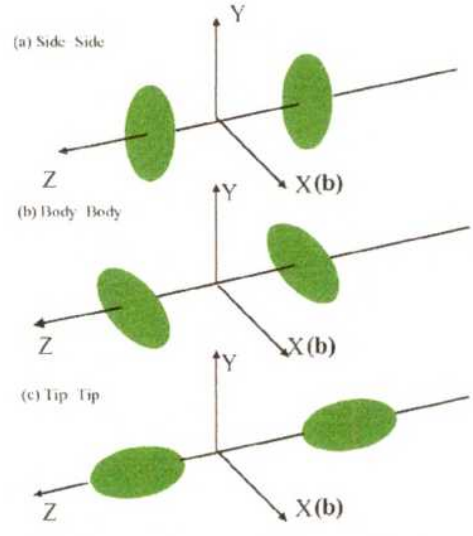

Figure 1.17: Different configurations of U+U collisions, taken from Ref [95].

This thesis is organised as following. In next chapter, we will introduce about STAR experiment of RHIC, viz, how collision takes place between relativistic particles, the way collision information became data and methods are processed. Next section will cover experimental techniques for data analysis, corrections and results from U+U collision. In consequent section, we will try to explain some of results of data analysis with simulation model formalism, which will be followed with conclusion.

Bibliography

[1] Murray Gell-Man, Phys.Lett. 8, 214-215 (1964)

[2] G. Zweig ,CERN-TH-412, NP-14146, PRINT-64-170 (1964)

[3] O.W. Greenberg, Phys. Rev. Lett.13, 598 (1964)

[4] O.W. Greenberg, arXiv:hep-ph/9301207

[5] Y. Nambu, inPreludes in Theoretical Physics, ed. A. de Shalit, H. Feshbachand L. Van Hove (North Holland, Amsterdam, 1966), p. 133;

[6] M.Y. Han and Y.Nambu,Phys. Rev.139, B1006 (1965)

[7] P. Soding, Eur. Phys. J. H 35, 3-28 (2010)

[8] C.H. Llewellyn Smith, Nucl. Phys. B 17, 277 (1970)

[9] C.H. Llewellyn Smith, Phys. Rev. D 4, 2392 (1971)

[10] J. Kuti, V.F. Weisskopf,Phys. Rev. D 4, 3418 (1971)

[11] R.P. Feynman, Photon-Hadron Interactions, Reading, MA : Benjamin, 1972, p. 152

[12] D.H. Perkins, Review paper, Proc. 16th Int. Conf. on High Energy Physics (Chicago-Batavia, 1972), Vol. 4, p. 189

[13] J. I. Friedman and H. W. Kendall, Annu. Rev. Nucl. Sci. 22, 203 (1972)

[14] J. D. Bjorken and E. A. Paschos, Phys. Rev. 185, 1975 (1969)

[15] Richard P. Feynman, Phys. Rev. Lett. 23, 1415 (1969)

[16] https://www.flickr.com/photos/slaclab/30603934362/in/photostream/

[17] Collins J C , Perry M J, Phys. Rev. Lett., 34, 1353 (1975)

[18] Cabibbo N, Parisi G, Phys. Lett. B , 59, 67-69 (1975)

[19] Pasechnik, R.; Sumbera, M., Universe, 3, 7. (2017)

[20] Ch. Berger et al. (PLUTO Coll.) Phys. Lett. B 78, 176 (1978)

[21] T. Appelquist, H.D. Politzer, Phys. Rev. Lett. 34, 43 (1975)

[22] T. Appelquist, H.D. Politzer,Phys. Rev. D 12, 1404 (1975)

[23] K. Koller, T.F. Walsh,Phys. Lett. B 72, 227 (1977)

[24] Ch. Berger et al. (PLUTO Coll.) Phys. Lett. B 82, 449 (1979)

[25] Ch. Berger et al. (PLUTO Coll.), Z. Phys. C 1, 343-347 (1979)

[26] Stella, B. & Meyer, HJ. EPJ H , 36: 203 (2011)

[27] https://player.slideplayer.com/24/7524101/data/images/img9.jpg

[28] https://player.slideplayer.com/24/7524101/data/images/img4.jpg

[29] Ulrich Heinz, Maurice Jacob,arXiv:nucl-th/0002042

[30] https://home.cern/news/press-release/cern/
new-state-matter-created-cern

[31] M.C. Abreu et al (NA50 Collaboration) Physics Letters B 477, 28- 36 (2000)

[32] F. Sikler et al. (NA49 Collaboration) Nuclear Physics A 661, 45c -54c (1999)

[33] https://www.phenix.bnl.gov/WWW/info/comment/

[34] C. Patrignani et al. (Particle Data Group), Chinese Physics C, Volume 40, Number 10 (2016)

[35] http://pdg.lbl.gov/2019/reviews/rpp2018-rev-qcd.pdf

[36] PhD Thesis, Alexander Laschka, Technische Universitat Munchen (2012)

[37] Alexandre Deura, Stanley J. Brodskyb, Guy F. de Teramond, Progress in Particle and Nuclear Physics 90,1-74 (2016)

[38] D. Gross and F. Wilczek, Phys. Rev. Lett. 30, 1343 (1973); Phys. Rev D 8, 3633 (1973)

[39] H. D. Politzer, Phys. Rev. Lett. 30, 1346 (1973)

[40] S Bethke, J. Phys. G: Nucl. Part. Phys.26 R27 (2000)

[41] D.H. Rischke, Prog. Part. Nucl. Phys. 52, 197 (2004)

[42] Leupold S. et al., Bulk Properties of Strongly Interacting Matter. In: Friman B. et al. (eds) The CBM Physics Book. Lecture Notes in Physics, vol 814. Springer, Berlin, Heidelberg, (2011)

[43] F. Karsch and K. Redlich, Phys. Rev. D 84, 051504(R) (2011)

[44] F. Karsch, Nucl. Phys. A 698, 199 (2002)

[45] F. R. Brown et al., Phys. Rev. Lett. 65, 2491 (1990)

[46] Masayuki Asakawa, Shinji Ejiri, and Masakiyo Kitazawa, Phys. Rev. Lett. 103, 262301 (2009)

[47] Y. Hatta and T. Ikeda, Phys. Rev. D 67, 014028 (2003)

[48] Tillmann Boeckel and Jurgen Schaffner-Bielich, Phys. Rev. D 85, 103506 (2015)

[49] Peter Braun-Munzinger and Johanna Stachel, Nature volume 448, pages 302-309 (2007)

[50] K. Geiger,Phys. Rev. D 48, 4129 (2009)

[51] J. D. Bjorken, Phys. Rev. D 27, 140 (1983)

[52] PhD theis, Hui Long, UCLA (2002)

[53] https://particlesandfriends.wordpress.com/2016/10/14/evolution-of-collisions-and-qgp/

[54] S A Bass et al , J. Phys. G: Nucl. Part. Phys.25 R1 (1999)

[55] Agnes Mccsy, Eur. Phys. J. C ,61: 705-710 (2009)

[56] http://alicematters.web.cern.ch/?q=content/node/1031

[57] P Stankus, Annu. Rev. Nucl. Part. Sci. 55, 517 (2005)

[58] S Turbide, R. Rapp, and C. Gale, Phys. Rev. C69, 014903 (2004)

[59] Jan-e Alam, Sourav Sarkar, Pradip Roy, T. Hatsuda, Bikash Sinha, Annals Phys. 286,159-248 (2001)

[60] G. Domokos and Joseph I. Goldman, Phys. Rev. D 23, 203 (1981)

[61] Jean-Francois Paquet , J. Phys.: Conf. Ser.832 012035 (2017)

[62] J.Rafelski and B.Muller, Phys. Rev. Lett. 48,1066 (1982)

[63] http://alice.web.cern.ch/content/strangeness-enhancement

[64] A K Chaudhuri, Journal of Physics G: Nuclear and Particle Physics, Volume 37, Number 7 (2010)

[65] J. Y. Ollitrault, Phys. Rev. D 46, 229 (1992)

[66] P. Huovinen et al. Phys. Lett. B 503, 58 (2001)

[67] http://hep.itp.tuwien.ac.at/qgpth05/talks/Vienna_pdf_final.pdf

[68] Luo, Xiaofeng Nucl.Phys. A956, 75-82 (2016)

[69] https://www.nap.edu/read/13438/chapter/4#87

[70] P. Koch, B. Muller and J. Rafelski, Phys. Rep. 142, 167 (1986)

[71] Strahov, E. & Fyodorov, Y. Commun. Math. Phys. 241: 343, (2003)

[72] PhD thesis, Anthony Robert Timmins, The University of Birmingham (2008)

[73] K. Nakamura, et al., (Particle Data Group), J. Phys. G 37, 075021 (2010)

[74] C. Blumea, C. Markert, Progress in Particle and Nuclear Physics 66 ,834-879 (2011)

[75] T. Abbott, et al., (E802 Collaboration), Phys. Rev. Lett. 66 , 1567 (1991)

[76] J. Bartke, et al., (NA35 Collaboration), Z. Phys. C 48 ,191 (1990)

[77] T. Alber, et al., (NA35 Collaboration), Z. Phys. C 64 ,195 (1994)

[78] S. Abatzis, et al., (WA85 Collaboration), Phys. Lett. B 447 ,178 (1999)

[79] F. Antinori, et al., (NA57 Collaboration), J. Phys. G 32, 427 (2006)

[80] S. Hamieh, K. Redlich, A. Tounsi, Phys. Lett. B 486,61(2000)

[81] P. Koch, J. Rafelski, W. Greiner, Phys. Lett. B 123,151 (1983)

[82] B. I. Abelev et al., (STAR Collaboration), Phys. Rev. C 77, 044908 (2008)

[83] M. M. Aggarwal et al., (STAR Collaboration), Phys. Rev. C 83, 024901 (2011)

[84] L. Adamczyk et al., (STAR Collaboration) Phys. Rev. Lett. 114, 022301 (2015)

[85] J. Adams, et al., (STAR Collaboration) Phys. Rev. Lett. 95, 122301 (2005)

[86] Greiner, C. APH N.S., Heavy Ion Physics, 14: 149 (2001)

[87] K. Redlich and A. Tounsi, Eur. Phys. J. C 24, 589 (2002)

[88] ALICE Collaboration, Nature Physics 13, 535-539, (2017)

[89] T. Susa, et al., (for the NA49 Collaboration), Nucl. Phys. A 698, 491c (2002)

[90] I. Chemakin, et al., (E910 Collaboration), Phys. Rev. Lett. 85 ,4868 (2000)

[91] J. Adams et al. (STAR Collaboration), Phys. Rev. Lett. 92, 052302 (2004)

[92] STAR, STAR-RICH Collaborations, arXiv:nucl-ex/0601042

[93] Daniel Kikola, Grazyna Odyniec and Ramona Vogt, Phys. Rev. C 84, 054907 (2011)

[94] Thomas Schorner-Sadenius, The Large Hadron Collider, Springer International Publishing Switzerland (2015)

[95] Md. Rihan Haque, Zi-Wei Lin, and Bedangadas Mohanty, Phys. Rev. C 85, 034905 (2012)

[96] PhD thesis, SABITA DAS, Institute of Physics, Bhubaneswar,2015

[97] PhD thesis, Md. Rihan Haque, NISER, Bhubaneswar, 2015

[98] Steffen A. Bass, Pramana 60 (2003) 593-612

Chapter 2

STAR Experiment at RHIC

2.1 Overview

Open town meeting of NSAC (Nuclear Science Advisory Committee) at Wells College in Aurora, NY, 1983 was possibly first crucial meeting for RHIC (Relativistic Heavy Ion Collider) experiment [1]. Major experiments before this was ISR (Intersecting Storage Rings, 1971-1984) and SPS (Super Proton Synchrotron,1981-1984) at CERN (European Council for Nuclear Research). Available nuclear volume in ISR was too small and this was supposed to shut down in mid 1984. Also energy available in the SPS was too low. Though ISABELLE experiment (Colliding Beam Accelerator (CBA)) was planned by BNL (Brookhaven National Laboratory), later it was cancelled[2].

Scientific questions in '83 meeting's Long Range Plan were [1, 3]:

- What is the nature of nuclear matter at energy densities comparable to those of the early universe?

- What are the new phenomena and physics associated with the simultaneous collision of hundreds of nucleons at relativistic energies?

RHIC experiment was designed to answer few such questions. We have shown one of meetings for creation of RHIC and it's current areal view in Fig. 2.1.

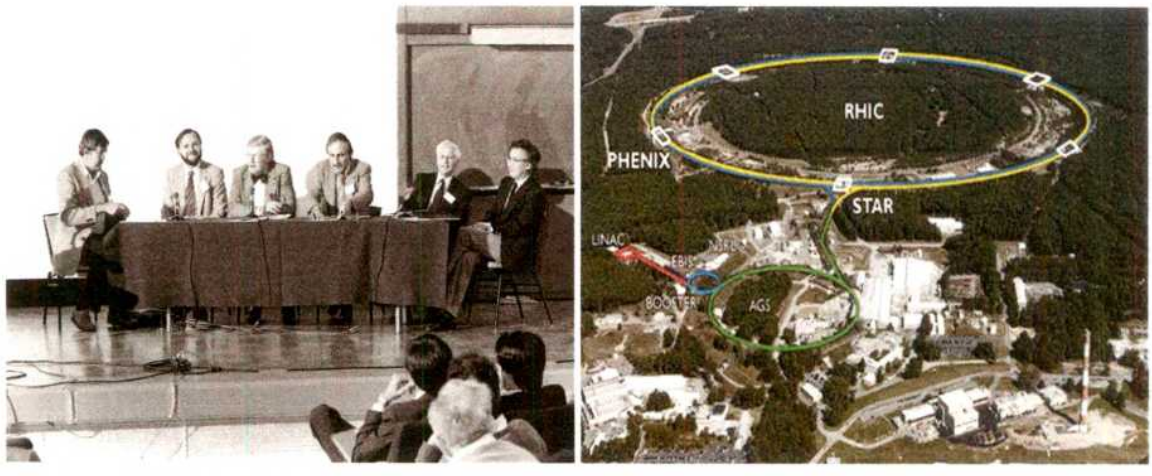

(a) Quark Matter '83 :[4] (b) Areal View:[4]

Figure 2.1: Inception meeting of RHIC and Current view

This was built at BNL with existing facility meant for CBA. This consists of 3.83km circumference of two superconducting rings (conventionally known as blue and yellow); where beams move in clockwise and anti-clockwise direction. There are six interaction points where two rings of magnet cross, thus allowing accelerating beams to collide. STAR(Solenoidal Tracker at RHIC), PHENIX (Pioneering High Energy Nuclear Interacting Experiment), PHOBOS(named for a moon of Mars), BRAHMS (Broad Range Hadron Magnetic Spectrometer), PP2PP and CNI & Gas jet Polarimeter experiment are situated at these six interaction points respectively. PHOBOS and BRAHMS completed its run in the years of 2005 and 2006, respectively.

RHIC becomes operational in 2000 with colliding Au+Au at 56GeV/c centre of mass energy. By the year 2017 it successfully collided Au, Cu, U in heavy ion side; while P, D, He in other side with centre of mass energy starting from 7GeV/c to 500 GeV/c . On one side, it is exploring quantum chromodynamics while on the other side dealing with spin physics. Some of the exciting results include establishment of experimental signature of Quark Gluon Plasma (QGP) in 2005 [5], discovery of nearly perfect fluid property of QGP, discovery of anti-matter (anti-hypertritons [6], anti-helium [7]) in 2011, discovery of strong elliptic flow [8] and discovery of jet quenching [9].

From the Table 2.1, one can find year wise it's operation until this thesis work

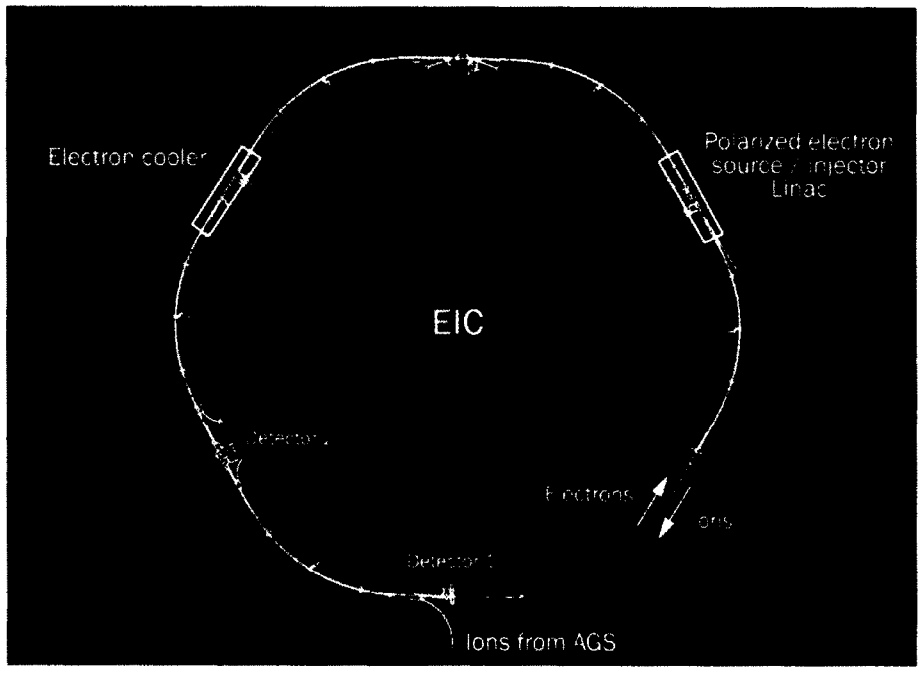

Figure 2.2: eRHIC-schematic design :[11]

has been carried out.

There are plans to build an Electron-Ion Collider(EIC) at BNL. Current design proposes addition of an electron ring inside the existing RHIC tunnel, which will be capable of reaching energies up to 18 GeV. Here both the ion and electron beams will be polarized to study nuclear spin and it's role in nuclear structure. EIC at Brookhaven Lab thus will be the world's first spin-polarized electron-nucleus collider. It would have the flexibility to change the nuclear ion species as well as the beam energies, both crucial for the systematic study of the 'glue' postulated to dominate the internal structure of nuclear matter [10]. Schematic of proposed EIC is shown in Fig. 2.2.

2.2 STAR Experiment

One of major goal of STAR is to investigate characterisation and formation of the Quark Glion Plasma. There are two ways of doing this, either one have to compress the matter or have to heat the matter, to a critical point where eventually they break their hadronic degrees of freedom. As those two things can be varied with

Table 2.1: RHIC Operations [12] from the day of it's inception up to the year, where this thesis work is carried out.

year	system	energy(GeV/nucleon)	luminosity
2000	Au+Au	27.9	<0.001 μb^{-1}
	Au+Au	65.2	<20 μb^{-1}
2001	Au+Au	100.2	<258 μb^{-1}
	Au+Au	9.8	<0.4 μb^{-1}
	P+P	100.2	<1.4 pb^{-1}
2003	d+Au	100.7-100.0	<73 nb^{-1}
	P+P	100.2	<5.5 pb^{-1}
2004	Au+Au	100.0	<3.53 nb^{-1}
	Au+Au	31.2	<67 μb^{-1}
	P+P	100.2	<7.1 pb^{-1}
2005	Cu+Cu	100.0	<42.1 nb^{-1}
	Cu+Cu	31.2	<1.5 nb^{-1}
	Cu+Cu	11.2	<0.02 nb^{-1}
	P+P	100.2	<29.5 pb^{-1}
	P+P	204.9	<0.1 pb^{-1}
2006	P+P	100.2	<88.6 pb^{-1}
	P+P	31.2	<1.05 pb^{-1}
2007	Au+Au	100.0	<7.25 nb^{-1}
	Au+Au	4.6	small
2008	d+Au	100.7-100.0	<437 nb^{-1}
	P+P	100.2	<38.4 pb^{-1}
	Au+Au	4.6	small
2009	P+P	249.9	<110 pb^{-1}
	P+P	100.2	<114 pb^{-1}
	P+P	100.2	<0.6nb^{-1}
2010	Au+Au	100.0	<10.3nb^{-1}
	Au+Au	31.2	<544 μb^{-1}
	Au+Au	19.5	<206 μb^{-1}
	Au+Au	3.85	<4.23 μb^{-1}
	Au+Au	5.75	<7.8 μb^{-1}
2011	P+P	249.9	<166 pb^{-1}
	Au+Au	9.8	<33.2 μb^{-1}
	Au+Au	100.0	<9.79 nb^{-1}
	Au+Au	13.5	<63.1 μb^{-1}
2012	P+P	100.2	<74.0 pb^{-1}
	P+P	254.9	<283 pb^{-1}
	U+U	96.4	<736 μb^{-1}
	Cu+Au	99.9-100.0	<27.0 nb^{-1}

Table 2.2: Bunch information [12]

Mode	No. of bunches	Ions per bunch [10^9]	β^* [m]	rms emittance [μm]	L_{peak} [$cm^{-2}s^{-1}$]	$L_{store\ avg}$ [$cm^{-2}s^{-1}$]	L_{week}
U-U	111	0.3	0.7	2.2 $\rightarrow$ 0.4	8.8×10^{26}	5.6×10^{26}	200

beam energy[13], RHIC is actively doing high-energy heavy-ion collisions at such a broad range of energies. We have shown current status and upgrade of STAR in Fig. 2.3.

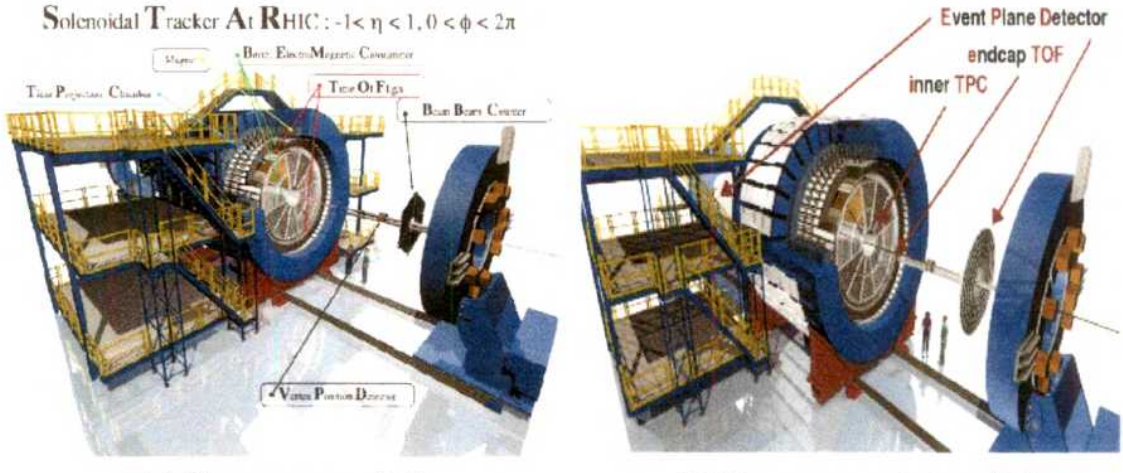

(a) Current status:[14] (b) Future upgradation :[15]

Figure 2.3: STAR Detector

Electron Beam Ion Source (EBIS) is used for generating ions. Optically Pumped Polarised Ion Source(OPPIS) is used to produce protons. Then ions or protons are collected in a bunch. In a bunch, there are about 10^9 ions or 10^{11} protons. And per store, there are number of such bunches accelerated to the target energy of collision with few nanosecond gap between two bunches. Technical information for U+U run are mentioned in Table 2.2.

Ions or protons pass through various Boosters before reaching RHIC storage ring. For U+U collisions, 4 bunches with 8×10^8 ions injected in the booster. Then they were combined into one. Booster can extract 6.5×10^8 ions per bunch with required speed. With 30% efficiency, AGS (Alternating Gradient Synchrotron) can extract 2×10^8 ions per bunch. And then they were transferred to RHIC accelerator ring

Table 2.3: Ion Movement [16] in Au+Au 200 GeV run. In U+U 193 GeV run, EBIS used for first time in RHIC operations.

Accelerator name	Incoming Ion		Outgoing Ion	
	charge	speed	charge	speed
EBIS			+32	2MeV
Booster Synchrotron	+32	2MeV	+77	100MeV
AGS	+77	100MeV	+79	8.86GeV
RHIC storage ring	+79	8.86GeV		

Table 2.4: Proton Movement[17]

Accelerator name	Incoming P speed	Outgoing P speed
OPPIS		750KeV
Linac	750KeV	200MeV
Booster	200MeV	2.35GeV
AGS	2.35	24.3GeV
RHIC Ring	24.3GeV	

with 6×10^8 ions per bunch. Speed & stripping of electrons (for Au+Au and p+p) can be found from Table 2.3 and 2.4.

Once they achieve target energy, collision takes place in either one of existing experiments, i.e. STAR or PHENIX. Once a collision takes place, emerging particles hit/pass through various detectors. Corresponding informations such as ionisation energy loss, number of hit, momenta etc are recorded in a .daq file.

Between every two events recorded, there is a dead time of detector of the order of nano-second. This data taking process runs over days/weeks as per event statistics asked by researchers.

From 19 April, 2012 to 15 May, 2012 U-U physics run have been taken by RHIC [18] with total delivered luminosity 736 μb^{-1} [12] (STAR and PHENIX each have 368 μb^{-1} [12]). RHIC Parameters for 96.4 GeV U-U Run is mentioned in Table 2.5.

Table 2.5: U+U injection and beam parameters [18] [12]

	beam energy[GeV]
injection	9.796
ramp	9.796 – 96.4
store	96.4
no of bunches	111
ions/bunch 10^9	0.3

2.3 Detector Setup

STAR experiment currently consists of 17 detector subsystem [19]. They are BBC (Beam Beam Counter), VPD (Vertex Position Detector), BEMC (Barrel Electromagnetic Calorimeter), EEMC (Endcap ElectroMagnetic Calorimeter), TOF (Time Of Flight), MTD (Muon Telescope Detector), BSMD (Barrel Shower Maximum Detector), FGT (Forward GEM Tracker), TPC (Time Projection Chamber), ESMD, ZDC (Zero Degree Calorimeters), FPD (Forward Pion Detector), SSD (Silicon Strip Detector), HFT (Heavy Flavour Tracker), FMS (Forward Meson Spectrometer), PXL (PiXeL detector) and Roman Pots. Last 6 detectors were not functional for run12 [20].

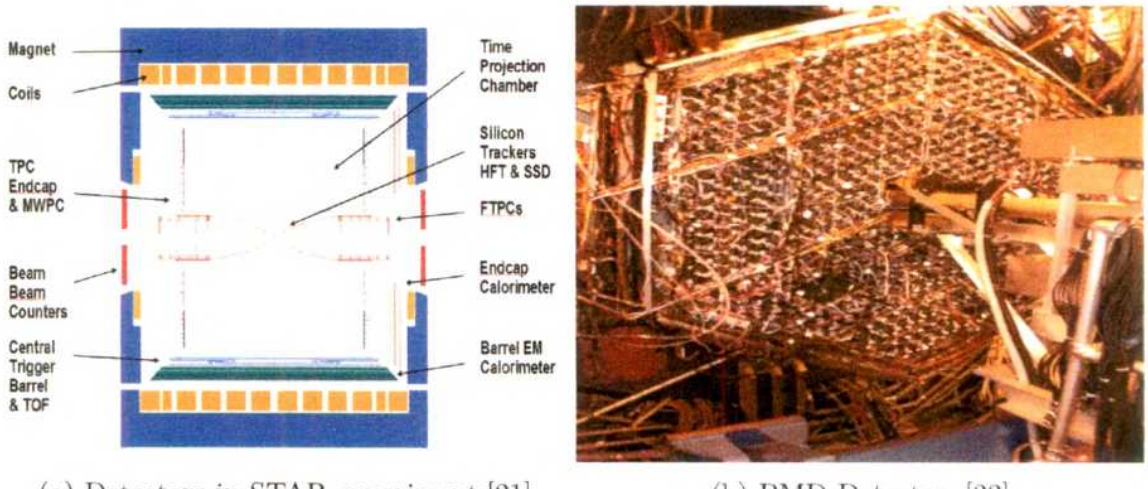

(a) Detectors in STAR experiment:[21] (b) PMD Detector :[22]

Figure 2.4: Cross-sectional view of STAR experiment and PMD

Future up-gradation consists of iTPC (Inner TPC), EPD (Event Plain Detector) and eTOF (Endcap TOF).

Out of few detectors used in past are RICH, CTB, FTPC(Forward TPC), SVT(Silicon Vertex Tracker) and PMD (Photon Multiplicity Detector). The PMD detector was fabricated and maintained by Indian group.

Cross-sectional view of STAR experiment and PMD detector is shown in Fig. 2.4.

For this thesis work, we have used few detector systems. To select minimum bias events from all the stored events, we have used Vertex Position Detectors (VPD), Zero Degree Calorimeters (ZDCs) and Beam-Beam counters (BBCs); which are parts of STAR trigger system. For identification and momentum of tracks, we have used Time Projection Chamber Detector (TPC) detector. We will explain in more detail about these systems in subsequent sections.

2.3.1 Trigger detectors

The interaction rates at RHIC for beams of highest luminosity may approach $\sim$ 10 MHz [51]. However, slow detectors (TPC, SVT, FTPC, EMC) can operate at rate of $\sim$ 200 kHz. STAR trigger system [24] based on input from fast detectors (ZDC, BBC, VPD), control the selection of events, for slower tracking detectors (in order to record data). Trigger detectors also used to select events with rare or specific signals of interest to increase the recorded statistics of these events [51].

A schematic diagram of a STAR trigger system is shown in Fig. 2.5.

There are three levels that use the fast trigger detectors. Level 0 receives data from the detectors and accepts events. Other two levels can only abort events. Only after it has passed all three levels, DAQ(Data Acquisition) is informed that an event has occurred [54].

- Level 0 is the 1st layer of trigger electronics. It consists of two a tree of Data Storage and Manipulation (DSM) boards, where the output from one layer feeds the next, and a Trigger Control Unit (TCU). This layer processes the trigger data for every RHIC crossing and accepts the event (initiates data taking) if it is interesting. The Level 0 hardware is implemented as a set of 9U

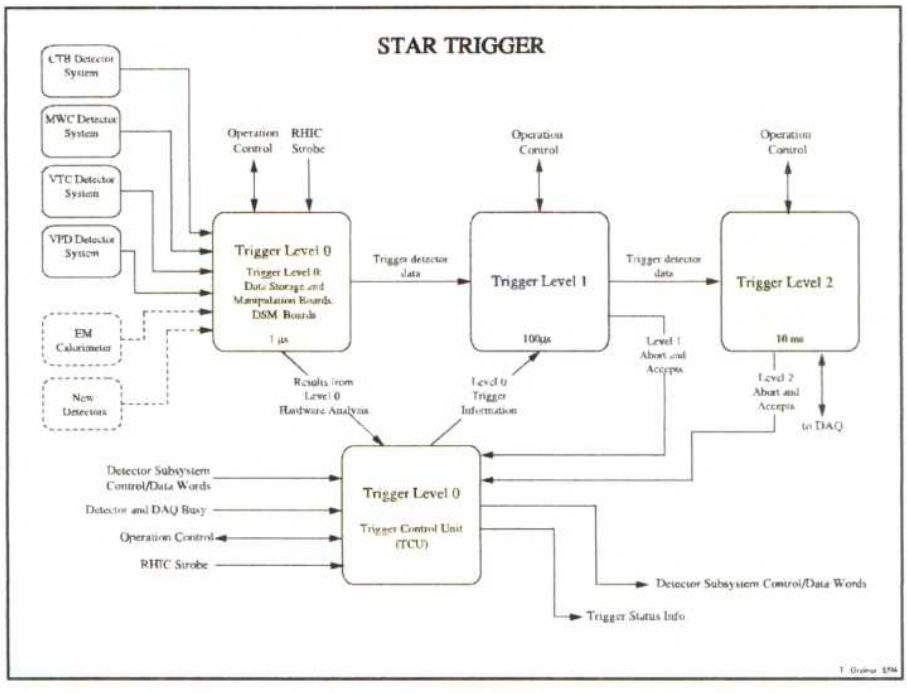

Figure 2.5: The STAR trigger system [25]

VME modules spread out over many VME crates on the first floor of the STAR electronics platform. The detector front-end electronics that feeds Level 0 is spread out over the detectors (BEMC and EEMC), more VME crates (CTB, ZDC, BBC and FPD) and some NIM crates (ZDC) [54].

- Level 1 is the next layer to Level 0, of trigger processing. This layer consists of 2 CPUs that read data from TCU and DSMs for each accepted event and pass it to Level 2 [54].

- Level 2 is the final pre-DAQ layer of trigger processing. This layer performs a more detailed analysis of the trigger detector data for just those events that were accepted by level 0. It either accepts the event and passes it on to DAQ, or aborts the event [54].

At $\sqrt{s_{NN}} = 200$ GeV, evaporation neutrons diverge by <2 milli-radians from the beam axis [26]. If $\theta \leq 0.4$ mrad, then neutral beam fragments can be detected downstream of RHIC ion collisions. In the same angular range, charged fragmentes usually too close to the beam trajectory. This is referred as zero degree region. ZDC's detect neutrons emitted within this region and measure their total energy;

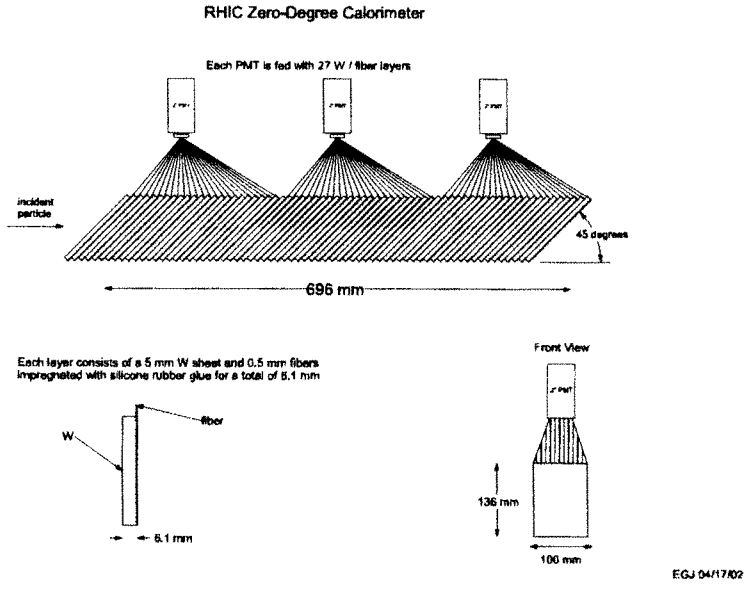

Figure 2.6: ZDC detector [25]

and hence we calculate charged particle multiplicity. Also for minimal bias events, we use ZDC coincidence of both beam directions. A schematic diagram of a ZDC detectors is shown in Fig. 2.6.

There are pair of BBC's wrapped around the beampipe, one on either side of the TPC. Each counter consists of two rings of hexagonal scintillator tiles: an outer ring composed of large tiles and an inner ring composed of small tiles. Internally, each ring is itself divided into two separate sub-rings of 6 and 12 tiles each [25]. A coincident signal from any of east side 18 tiles with any of west side 18 tiles of the normal interaction region, constitutes a BBC coincidence [27]. BBC's are used in STAR during p+p runs to provide triggers, to monitor the overall luminosity, and to measure the relative luminosity for different proton spin orientations [28]. A schematic diagram of a BBC detectors is shown in Fig. 2.7.

A pair of VPD's is also used to select events [29] . Each VPD consists of 19 lead converters plus plastic scintillators with photo- multiplier tube readout. These are positioned very close to the beam pipe on each side of STAR [52, 53]. Each VPD is about 5.7 m from interaction point and have pseudo-rapidity range $4.24 < |\eta| < 5.1$.

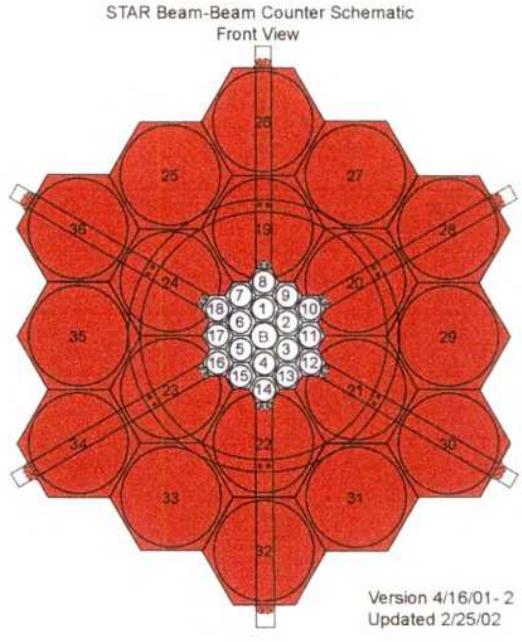

Figure 2.7: BBC detector [25]

Trigger for the minimum-bias events using VPD, is defined as a coincidence signal in the east and west VPD detectors [52]. The VPD also provides information about the Z component of the primary vertex. The VPD has much better timing resolution than the BBC detector.

The main STAR calorimeters comprise a full Barrel Electromagnetic Calorimeter (BEMC) [31], single Endcap Electromagnetic Calorimeter (EEMC) [30] and a Forward Meson Spectrometer (FMS) [32]. The electromagnetic calorimeters allow STAR to trigger on and study rare and high p_T processes such as jets, leading hadrons, direct photons, and heavy quarks [51, 53]. They provide large acceptance for photons, electrons along with neutral pions, and η mesons in all collision systems from polarized p+p to Au+Au collisions. These are also used for characterisation of event in heavy-ion collisions including ultra-peripheral collisions [51, 53]. A schematic diagram of a BEMC/EEMC detectors is shown in Fig. 2.8.

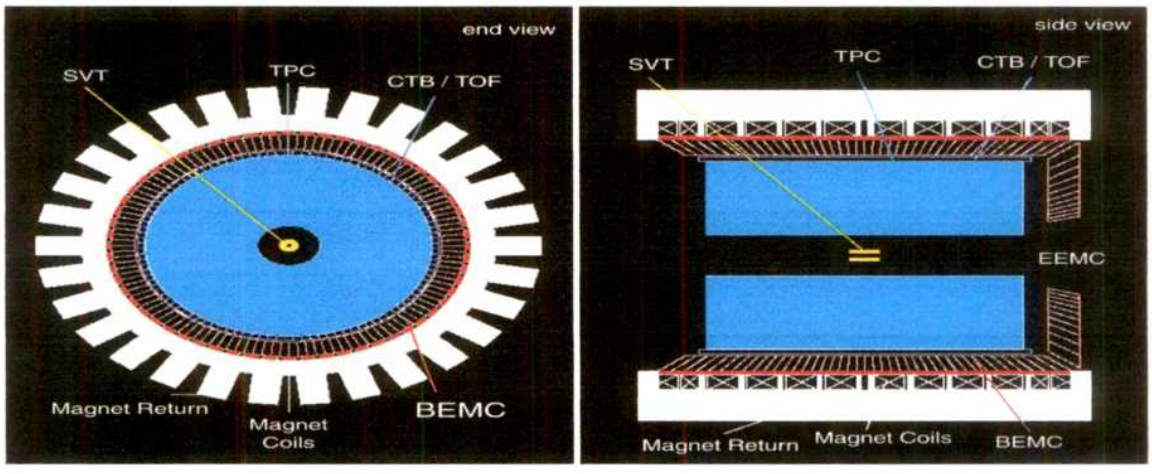

(a) BEMC detector [25] (b) EEMC detector [25]

Figure 2.8: STAR calorimeters

2.3.2 TPC detector

TPC is main tracking device of STAR experiment. It records tracks of particles, measures their momenta and ionisation energy loss [33]. From ionisation energy loss, it identifies tracks. It has a wide coverage of pseudo-rapidly (± 1.8 units) and full azimuthal coverage. All charged particles, which have momentum greater than 100 MeV/c are identified in the TPC [33].

The design and specification strategy for the TPC have been guided by the limits of the gas and the financial limits on size, without seriously compromising the potential for tracking precision and particle identification [33]. Basic parameters for STAR TPC is given in Table 2.6. We have shown cross-sectional view of TPC detector and one of collision-eye view in Fig. 2.9.

2.3.3 Technical design of TPC detector:

The TPC is 4.2 m long and 4 m in diameter. It is an empty volume of gas in a well defined, uniform, electric field of $\sim$ 135 V/cm. It sits inside large solenoidal magnet which operates at 0.5 T.

The TPC is filled with P10 gas (10% methane, 90% argon) regulated at 2 mbar above atmospheric pressure. It's primary attribute is a fast drift velocity which

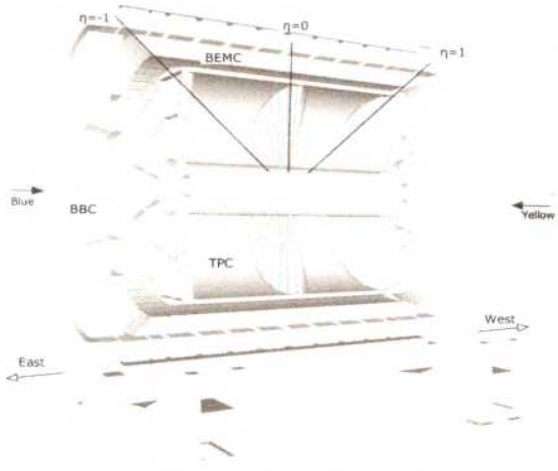

(a) TPC Detector:[35]

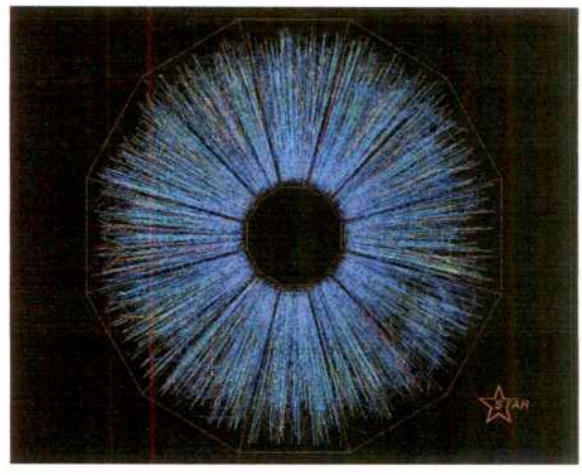

(b) AuAu collision eye view:[36]

Figure 2.9: TPC and Collision eye view

Table 2.6: TPC parameters [33]

Item	Dimension
Length	420cm
Outer/Inner diameter	400/100cm
Cathode diameter	400cm
Cathode potential	28kV
Drift gas	P10
Pressure	Atmospheric + 2 mbar
Number of anode sector	$12 * 2 = 24$
Number of pad rows	$12 * 2 * 45(13inner, 32outer) = 1080$
Number of pads	12*2*5692 (1750 inner, 3942 outer) =1,36,608
Magentic field	0, $\pm$ 0.25T, $\pm$ 0.5T
Electric field	135 V/cm

peaks at a low electric field. The gas system circulates gas in TPC and maintains purity, reducing electro negative impurities (viz. oxygen and water) which capture drifting electrons. To keep the electron absorption to a few percent, the oxygen is held below 100 parts/million and water less than 10 parts/million [33].

Electrons from ionized gas drift toward the nearest endcap, where the signals are read out. TPC readout is divided into 24 sector (12 on each side of end-cap). Each sector is divided into inner and outer sub-sectors. The inner and outer sector geometries are somewhat different, to emphasise 2-track separation at small radii, and good dE/dx and moderate channel count at large radii[34]. Each inner sector

Table 2.7: Inner and outer sector parameters. [34]

	Inner Sector	Outer Sector
Pad length	1.15 mm	19.5 mm
Pad width	2.85 mm	6.2 mm
Anode wire-pad spacing	2 mm	4 mm
Mean N_{pri}	33	79
Wire voltage	1170 V	1390 V
Wire gain	3770	1230
Pad:wire coupling	30%	34%
Min. ion signal	23000 e^-	21000 e^-
Number of pads	1750	3942

have 13 pad rows, whereas outer sector have 32 pad rows; so a track can give a maximum 45 hits. We have listed few Inner and outer sector parameters in Tab. 2.7.

The readout chambers have 3 wire planes: a gated grid, ground plane, and anode wires.

- The gated grid is normally closed, minimizing buildup of positively charged ions in the drift volume. When a trigger is received, the voltages are switched and it becomes transparent [34].

- The ground plane, anode wires (and TPC pad plane) form a multi-wire proportional chamber. Electrons drift to the wire where they initiate an avalanche, leaving a cloud of positively charged ions remaining around the wire. The 136,608 pads on the TPC pad plane image this charge; this image charge goes to the electronics [34].

2.3.4 Reconstruction of the x, y & z position:

As STAR TPC sits over an uniform magnetic filed, so a charged track can be described by helix. It can be parameterized as function of the track length. This can

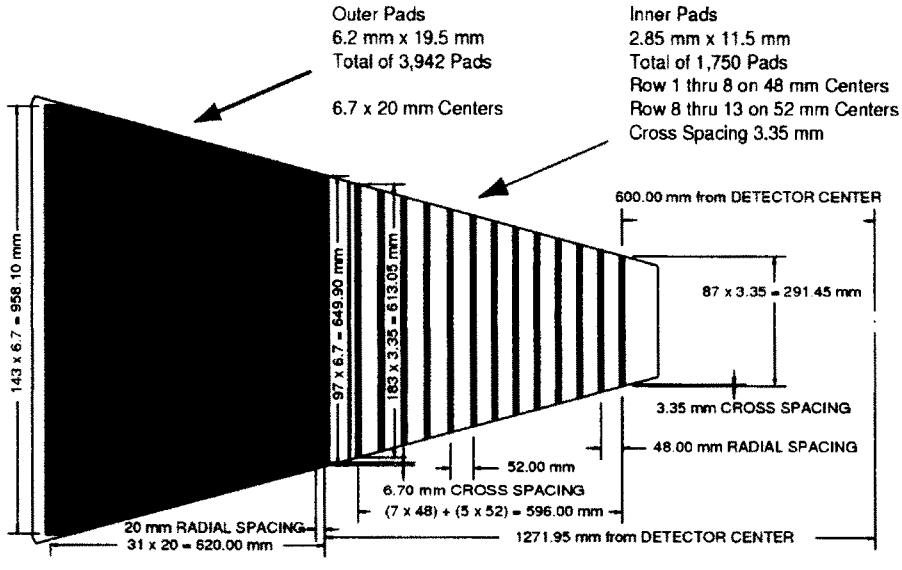

Figure 2.10: The anode pad plane with one full sector shown [33]

be defined as [47]:

$$x(s) = x_0 + \frac{1}{k}[cos(\psi_0 + hskcos\lambda) - cos\Phi_0] \tag{2.1a}$$

$$y(s) = y_0 + \frac{1}{k}[sin(\psi_0 + hksin\lambda) - sin\Phi_0] \tag{2.1b}$$

$$z(s) = z_0 + ssin\lambda. \tag{2.1c}$$

Here s is path along helix, λ is the dip angle, $\Phi = \psi + \pi/2$, k is curvature (1/R), $\psi(s)$ is azimuthal angle of the track direction at the origin of the helix [46], and h is ± 1, i.e., the rotation of the helix, projected in the xy plane (depends on the sign of the product of magnetic field and charge of the particle [47]. Projections in both the axis is shown in Fig. 2.11.

Transverse momentum of a track is determined by fitting a circle through x, y co-ordinates of a vertex and the points along the track [33]. This can be written as:

$$p_T = 0.3 \times B \times r \times q, \tag{2.2}$$

where B is the magnetic field, q is the charge of the particle and r is the radius of curvature of helix.

For weak decay particles used in this thesis, fitting has to be done with out

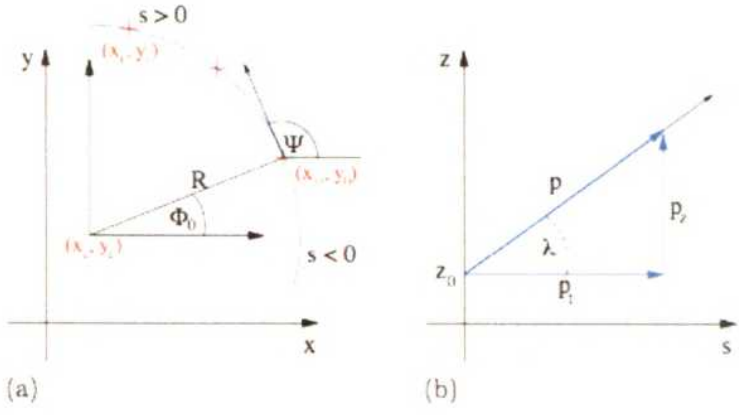

Figure 2.11: Visualisation of the helix: (a) projection in the xy plane (b) projection in the sz plane [47].

reference to primary vertex.

2.3.5 Particle identification using dE/dx

Ionisation energy loss works good for low p_T tracks, as energy loss band merges at high momentum. STAR experiment can separate pions and protons up to 1.2 GeV/c [33].

One usual practice to use standard deviation of Gaussian distribution from measured and expected value. This can be written as:

$$n\sigma = \frac{1}{R} log(\frac{< dE/dx >_{Exp}}{< dE/dx >_{Th}}). \tag{2.3}$$

Where $< dE/dx >_{Exp}$ is the energy loss measured in experiment, $< dE/dx >_{Th}$ is theoretical value (calculated from Bichsel functions [37]) and R is dE/dx resolution of the TPC detector ($\sim$ 8% if the track crosses 40 pad-rows).

Using extended Bethe-Bloch formula [38], most probable Bichsel values can be written as:

$$- < \frac{dE}{dx} >= K z^2 \frac{Z}{A} \frac{1}{\beta^2} [\frac{1}{2} ln f(\beta) - \beta^2 - \frac{\delta(\beta\gamma)}{2}]. \tag{2.4}$$

Where $f(\beta) = \frac{2m_e c^2 \beta^2 \gamma^2 T_{max}}{I^2}$,

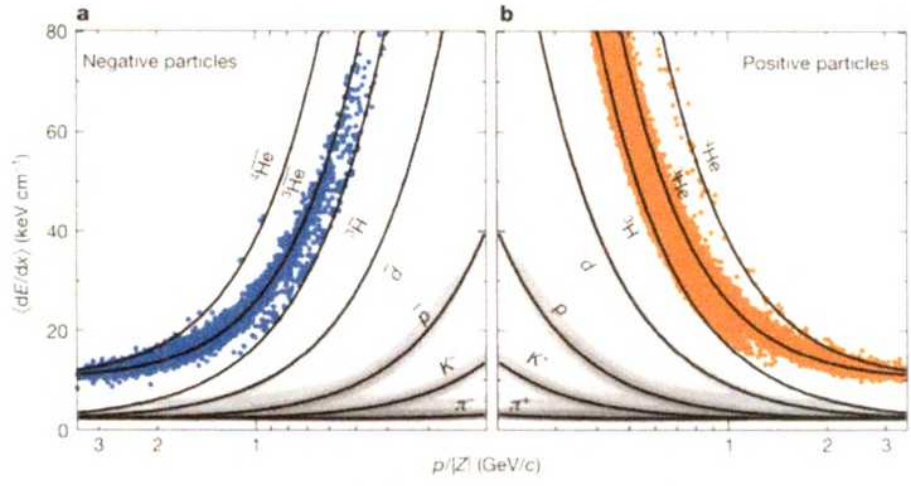

Figure 2.12: dE/dx distribution :[39]

$T_{max} = \frac{2m_e c^2 \beta^2 \gamma^2}{1+2\gamma m_e/M+(m_e/M)^2}$.

Here K is a constant, A atomic mass of absorber, Z, z and is atomic number of absorber and incident particle respectively, m_e is mass of electron, c is the vacuum speed of light, I is characteristic ionisation constant, T_{max} is the maximum energy transfer, $\delta(\beta\gamma)$ is density effect correction to ionisation energy loss, $\beta\gamma$ = p/Mc, where p is momentum and M is mass of charged particle. We have shown one such figure in Fig. 2.12.

2.3.6 Momentum Resolution

Embedding techniques are used to estimate momentum resolution. A track with a known momentum is created using the track simulator [33]. After that, to simulate the momentum smearing effects, tracks are embedded in a real event. The simulator implements all the processes that lead to the detection of particles; viz, gas gain, signal collection, ionisation, electron drift, dead channels, electronic amplification and electronic noise.

As we can see from Fig 2.13, momentum resolution is about 2% - 7% for pions.

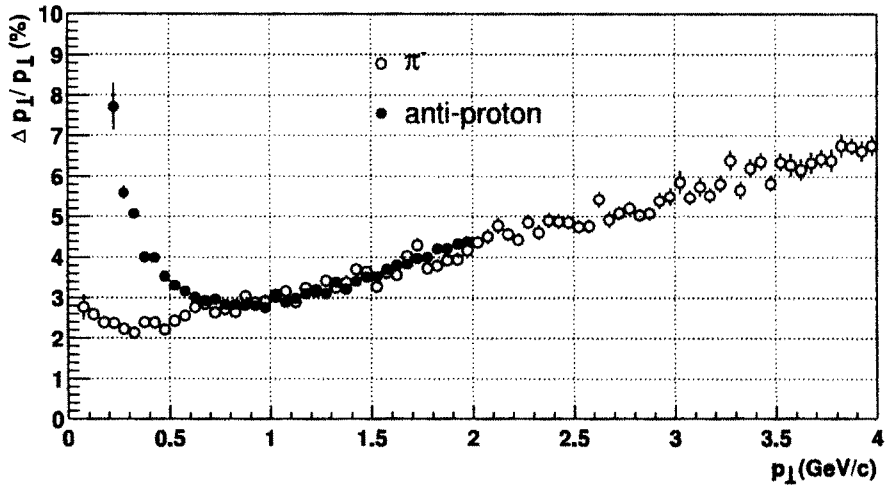

Figure 2.13: Transverse momentum resolution of tracks in STAR TPC [33]

2.4 Cooling

RHIC performs at a temperature maximum of 4 trillion degrees Celsius or 250,000 times hotter than the centre of the sun [40]. To counter this, liquid helium is being pumped into RHIC's 1,740 superconducting magnets to cool them about absolute zero temperature (-273 degree). This helps magnets to operate with zero energy loss.

Detector cooling system can broadly divided into 2 parts [41]:

- ECU cooling unit, which regulates air flow and air temperature, and
- Interlocks, Any condition that can potentially harmful for STAR.

FEE cards of TPC pad planes are water cooled to ± 0.7 deg C (to keep the wire gain constant and maintain the dE/dx calibration)[42, 43]. FTPC FEE cards are air cooled.

For the period of 2018-2020, RHIC CAD is undertaking an upgrade of electron cooling [44].

2.5 Calibration

Data AcQuisition System (DAQ) in STAR starts with STAR's trigger system, which is divided in four stages. Level 0 trigger operates using trigger detectors (MWC, ZDC, BBC and BEMC detector). If the data that passed Level 0, it is digitised and recorded. Then a subset of data is analysed by the Level 1 trigger. Level 2 trigger takes over after Level 1 passes the pre-set trigger condition. For displaying the reconstructed event in real time, some of the data is passed to Level 3 trigger, which is in fact online reconstruction software.

If the event is passed from trigger system, it is written to the disks of High Performance Storage System (HPSS) [47].

The reconstruction pass is managed by reconstruction framework, root4star. This converts the DAQ file to DST(Data Summary Tables) and other products [45] [a rough estimation of size between DST and Micro-DST is about five]. To have a immediate online QA (quality assurance & quality control), a small sample of the events are analysed online during data taking [45]. As the data flow runs to to mass storage, a small fraction of the data passes through Fast Offline (for event reconstruction).

An estimate of U+U & Au+Au central event size for DAQ files is 1.02 MB [45]. After reconstruction, U+U central event size is 6.38 MB [45]. The data-set we have analysed were about 600×10^8 events (which will make it to the size of 382.8 PB of data !!!!). Final raw data is stored to the High Performance Storage System (HPSS). After reconstruction, the data is made available on disk for further analysis.

2.6 Computing

RCF (RHIC Computing Facility) at BNL (Brookhaven National Labortory) server is a Tier 0 centre for STAR experiment [48]. Currently RCF has 350 computing nodes, 1500 CPUs and 500TB of disk space dedicated to STAR experiment only [48]. STAR have a single Tier 1 centre: PDSF(Parallel Distributed Systems Fa-

cility) located at the NERSC(National Energy Research Supercomputing Centre), LBNL and at KISTI (Korean Institute of Science and Technology), Daejon, South Korea. STAR Tier 2 centres are at USA (Wayne State University and MIT) and Europe(NPI/ASCR,Prague) [49]. Regularly redistribution of small section (and entire sets of quantities) of the raw data are useful for physics analysis, takes place between Tier-1 (or Tier-2) centres.

Fetching of data for analysis purposes, STAR uses the SUMS (STAR Unified Meta Scheduler) [50, 48] tool. This gets data (in xrootd format) from the existing servers and perform jobs as mentioned in the xml file. Output files are received at user end. Physicist make analysis using those files.

Bibliography

[1] G Baym, Nucl.Phys. A698 (2002) XXIII-XXXII

[2] https://www.bnl.gov/rhic/news/121807/story1.asp

[3] https://www.bnl.gov/rhic_ags/users_meeting/Past_Meetings/2008/Agenda/Wed/BNL-baum.pdf

[4] https://www.bnl.gov/newsroom/news.php?a=26204

[5] PHENIX Collaboration, et al, Nucl.Phys.A757:184-283,2005

[6] STAR Collaboration, Science 02 Apr 2010:Vol. 328, Issue 5974, pp. 58-62

[7] STAR Collaboration, Nature 473, 353-356 (19 May 2011)

[8] STAR Collaboration, Phys. Rev. Lett. 86: 402-407,2001

[9] PHENIX Collaboration, Phys. Rev. Lett. 88: 022301, 2002

[10] https://www.bnl.gov/eic/eRHIC.php

[11] https://www.bnl.gov/eic/machine.php

[12] http://www.agsrhichome.bnl.gov/RHIC/Runs/

[13] Peter Braun-Munzinger and Johanna Stachel,Nature 448 (2007) 302-309

[14] http://www.rhip.utexas.edu/assets/index/pictures/star1.jpg

[15] https://inspirehep.net/record/1411819/files/BESII.png

[16] http://en.wikipedia.org/wiki/Relativistic_Heavy_Ion_Collider

[17] https://www.bnl.gov/userscenter/thesis/past-competitions/2012/Koster/KOSTER_THESIS.pdf

[18] http://www.agsrhichome.bnl.gov/AP/RHIC2012/

[19] https://drupal.star.bnl.gov/STAR/operations/detector_states

[20] https://drupal.star.bnl.gov/STAR/system/files/Det_Ops_Checklist_Feb_18_2012_Vers1.pdf

[21] https://www.star.bnl.gov/public/tpc/photos/GeneralMisc/STARdetector.jpg

[22] http://www.star.bnl.gov/public/pmd/pmd_feb04.jpg

[23] https://www.star.bnl.gov/public/trg/.introduction/Detectors_2004.pdf

[24] F. S. Beiser et al., Nucl. Instr. and Meth. A, 499, 762 (2003).

[25] https://www.star.bnl.gov/public/trg/

[26] C. Adler et al., Nucl. Instr. Meth. A 470, 488 (2001).

[27] J. Kiryluk, Trieste/Maine SPIN 2004, 2004, 718-721; arXiv:hep-ex/0501072

[28] J. Kiryluk, AIP Conf. Proc. 675, 424 (2003)

[29] M. Shao et al., Nucl. Instr. Meth. A 492 (2002) 344; W. J. Llope et al., Nucl. Instr. Meth. A 522 (2004) 252.

[30] C. E. Allgower et al., Nucl. Inst. Meth. A, 499, 740-750 (2003)

[31] M. Beddo et al., Nucl. Inst. and Meth. A 499, 725 (2003).

[32] W. W. Jacobs (for the STAR Collaboration), J. Phys., Conf. Ser. 160, 012008, (2009)

[33] M. Anderson et. al, Nuclear Instruments and Methods in Physics Research A 499 (2003) 659-678

[34] M. Anderson et. al, Nuclear Instruments and Methods in Physics Research A 499 (2003) 679 - 691

[35] http://people.physics.tamu.edu/sakuma/star/jets/c101218_misc/s0010_sketchup_001/images/star_sectioncut_02.png

[36] http://www.bnl.gov/bnlweb/photos/E80frontHR.jpg

[37] H. Bichsel, Nucl. Instr. Meth. A 562, 154 (2006)

[38] http://pdg.lbl.gov/2009/reviews/rpp2009-rev-passage-particles-matter.pdf

[39] http://cdn.iopscience.com/images/0954-3899/38/12/124072/Full/jpg398582fig01.jpg

[40] https://www.bnl.gov/rhic/news2/news.asp?a=1606&t=pr

[41] https://indico.cern.ch/event/469996/contributions/2148211/attachments/1278567/1898205/Bonn_2016_HFT_Pixel_Mechanics_Cooling.pdf

[42] M. Anderson et. al, Nuclear Instruments and Methods in Physics Research A 499 (2003) 679-691

[43] Nuclear Physics A, 499, 679-691 (2003)

[44] NuXu(STAR Collaboration),Nuclear Physics A 931 (2014) 1-12

[45] https://drupal.star.bnl.gov/STAR/files/STAR_Computing_Plan_Jan_22_2009.pdf

[46] PhD thesis, Michael L. Miller, Yale University, 2004 https://drupal.star.bnl.gov/STAR/files/startheses/2003/miller_michael.pdf

[47] PhD thesis, Betty I. Bezverkhny Abelev, Yale University, 2007

[48] Petr Chaloupka et al., Journal of Physics Conference Series, 219(7), 072031 https://drupal.star.bnl.gov/STAR/files/STAR_tier2.pdf

[49] PhD thesis, Mgr. Michal Zerola, Charles University, 2012, http://inspirehep.net/record/1220012/files/thesis_5.pdf

[50] http://www.star.bnl.gov/public/comp/Grid/scheduler/index.html

[51] PhD thesis, SABITA DAS, Institute of Physics, Bhubaneswar,2015

[52] Phd thesis, Shikshit Gupta,University of Jammu, India, 2015

[53] PhD thesis, Md. Rihan Haque, NISER, Bhubaneswar, 2015

[54] https://www.star.bnl.gov/public/trg/runschool/introduction/

Chapter 3

Strangeness Production in STAR

3.1 Dataset

The data we have used is from run12 of STAR experiment at RHIC for U+U collisions at $\sqrt{s_{NN}}$ = 193 GeV using minimum bias trigger. Minimum bias trigger requires co-incidence of signals from VPD, ZDC and/or BBC. Protected trigger assures from pile-up events. Bad runs are removed as mentioned in Ref. [1].

The dataset information is listed in Table 3.1.

Table 3.1: Dataset

Trigger Setup Name	UU_production_2012
Trigger ID (400005/400015/ 400025/400035)	vpd-zdc-mb-protected
File type	st_physics
Library	SL12d
Production tag	P12id
Total run numbers	783

3.2 Centrality selection

Centrality defination is based on StRefMultCorr class. This uses charged particle multiplicity (un-corrected) within $|\eta| < 0.5$. Different centrality bins (viz, 0-5%,

5-10%, 10-20%, 20-30%, 30-40%, 40-60% and 60-80%) were obtained by comparing measured $dN_{ch}/d\eta$ with input from simulation model [2]. This is presented in Fig. 3.1.

Table 3.2 gives the average number of reference multiplicity (RefMult), Number of participants (Npart) and number of binary collisions (Ncoll) for different centralities [3].

Table 3.2: Average reference multiplicity, participants and binary collisions

Centrality	RefMult	$< N_{part} >$	$< N_{coll} >$
0-5%	≥ 535	414.873	1281.26
5-10%	≥ 466 & < 535	355.421	1010.97
10-20%	≥ 338 & < 466	277.29	713.269
20-30%	≥ 233 & < 338	195.1615	435.2285
30-40%	≥ 150 & < 233	133.207	253.8305
40-60%	≥ 50 & < 150	69.51445	103.61285
60-80%	≥ 10 & < 50	21.99945	22.48325

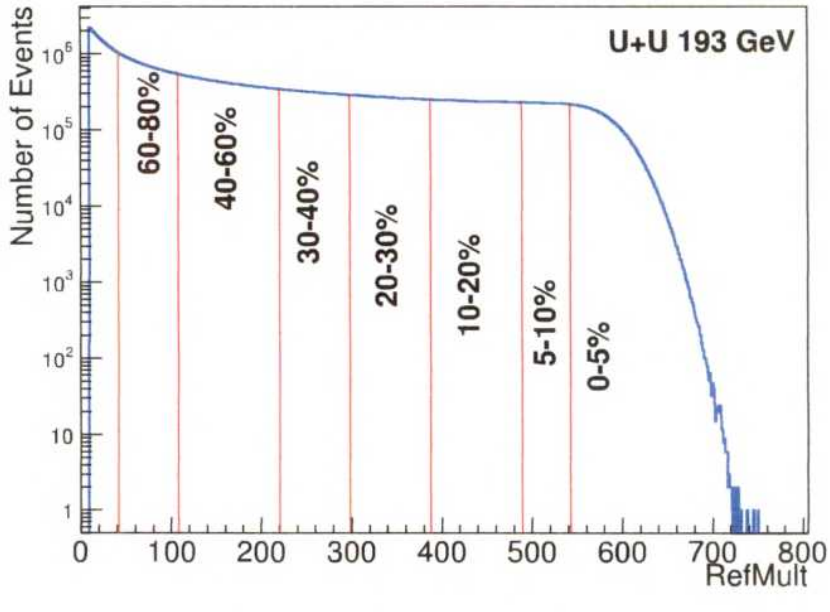

Figure 3.1: Reference multiplicity distribution of events. 0-5% corresponds most central collision, while 60-80% for most peripheral collision.

3.3 Events selection

Primary vertex is supposed to be the point where collisions occurred. This can be identified from all reconstructed tracks. However, due to finite detector resolution, it may vary. We have applied cut on distance of vertex from centre of TPC in the longitudinal direction of beam (V_z) as well as along transverse direction ($V_r = \sqrt{V_x^2 + V_y^2}$). We have taken V_z value to maximum available on StRefMultCorr class and we have taken half of the value of TPC beam-pipe radius ($\sim$ 3.75cm) as V_r.

Table 3.3 gives numerical values of the analysis cuts that have been applied for selecting events for this analysis. And Fig. 3.2 shows distributions in this regard.

Table 3.3: Event cuts

$\lvert V_z \rvert$	$\leq$ 30 cm
V_r	$\leq$ 2.0 cm
Statistics	285×10^6 events
Centrality	0-80%

In this work, we have reconstructed secondary (K_s *and* Λ) and tertiary vertex (Ξ *and* Ω) apart from in-built primary vertex. This can be done from their decay daughters, which will be discussed in detail in Sec 3.5.

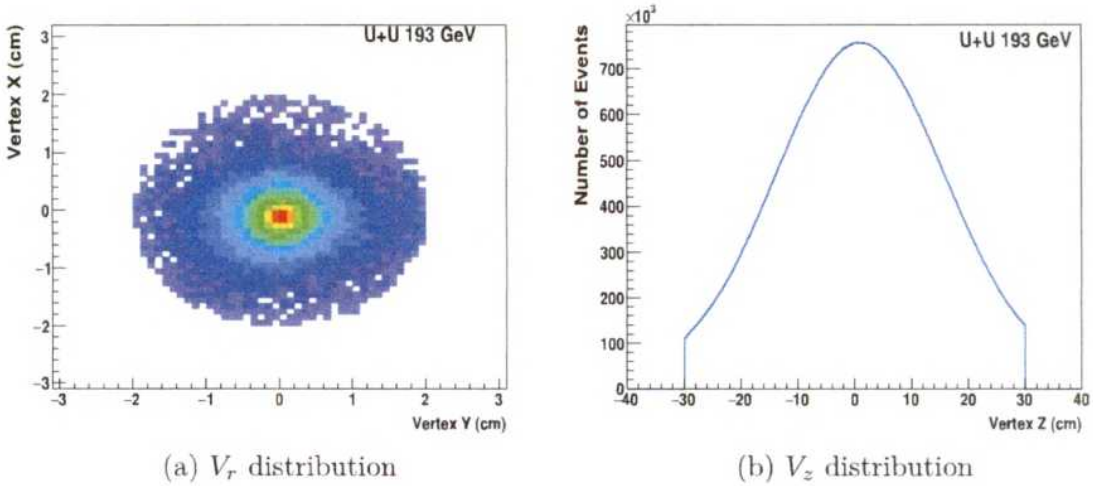

(a) V_r distribution (b) V_z distribution

Figure 3.2: Event's vertex distributions in x, y and z directions.

3.4 Track selection

All reconstructed tracks are referred as global tracks. Reconstruction is done by the helix fit to the TPC points one by one. (A primary track is reconstructed by the fitting helix to TPC points along with vertex, however this is not used in this thesis work).

To identify individual charged track, we have used dE/dx method, which may be defined as below:

$$N\sigma_i = \frac{1}{R} log\left(\frac{dE/dx_{Exp}}{dE/dx_{Th}}\right), \tag{3.1}$$

where R is resolution of the TPC detector, dE/dx_{Exp} is the experimental energy loss values measured by TPC detector and dE/dx_{Th} is the theoretical energy loss values taken from Bischel function [9]. A dE/dx distribution for charged tracks is shown in Fig. 3.3b. Solid lines represent Bischel function values, while red, green, blue marker represent pion/kaon/proton, respectively.

A track needs to have momentum > 100 MeV in order to overcome magnetic field of TPC. Tracks with lesser number of hits, primarily arises from splitting are rejected. For our analysis, charged tracks those are decay products as listed in Tab. 3.5, lying within pseudo-rapidity window as unity and full azimuthal coverage. We have taken 4 standard deviation (95.45%) from the mean of normal distribution, for a track. Table 3.4 gives numerical values of the analysis cuts that have been applied to tracks.

Table 3.4: Track cuts

p_T	$\geq$ 0.15 GeV
nHits	$\geq$ 15
$\|\eta\|$	$\leq$ 1
$\|n\sigma\|$	$\leq$ 4

In U+U dataset, there were some technical issue with sector-7 of TPC (details can be found from Ref [4, 5, 6]), for which we had to reject all tracks falling under this window. This thesis work, carried over tracks after rejecting all such cuts. $\eta - \phi$

distribution after removal of such cuts may be found at Fig. 3.3a.

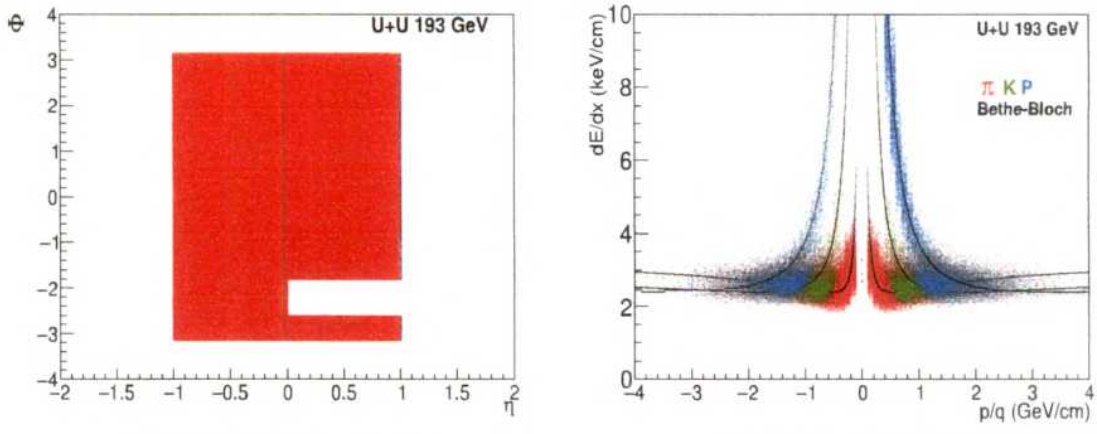

(a) Eta-Phi distribution

(b) dE/dx distribution

Figure 3.3: Fig. 3.3a shows $\eta - \phi$ distribution. The blank portion shows the excluded region for sector-7 tracks of TPC. Fig. 3.3b shows ionisation energy loss of particles as a function of rigidity.

3.5 Particle reconstruction

3.5.1 Analysis cuts

V_0 name has originated from bubble chamber photographs. Decay of it looks like V and 0 denotes a neutral particle. Since Ξ and Ω undergo a two-step cascading decay into a nucleon, these are called as cascade particles. Table 3.5 presents properties of V_0 and cascade tracks, which are used in this thesis work. Pictorially, most of these cuts are presented in Fig. 3.4.

Table 3.5: Particle properties

Particle	Decay mode	Branching ratio	PDG mass	Decay length
K_s	$\pi\pi$	68.6%	0.497 GeV	2.68 cm
Λ	Pπ	63.9%	1.1156 GeV	7.89 cm
Ξ	$\Lambda\pi$	99.88%	1.3211 GeV	4.91 cm
Ω	Λk	67.8%	1.67245 GeV	2.46 cm

Numerical values of the topological cuts that have been used for reconstructing V_0 and cascade candidate is mentioned in Table 3.6 and Table 3.7, respectively.

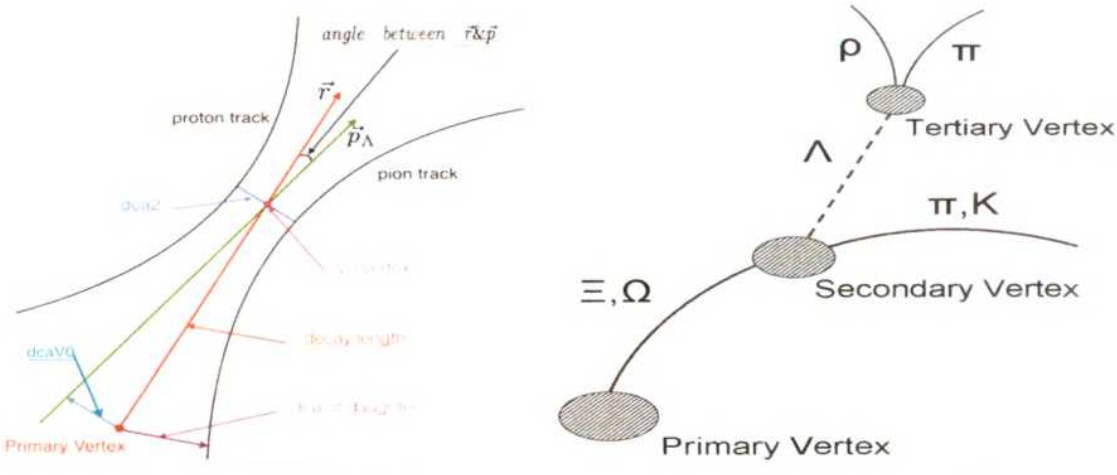

(a) V_0 topology :[7] (b) Cascade topology :[8]

Figure 3.4: Topology of tracks for V_0 and cascade tracks used in our analysis.

Table 3.6: V_0 topology cuts

Cut	K_s	$\Lambda(\bar{\Lambda})$
dau1 Dca	$\geq$2.0	$\geq$1.0
dau2 Dca	$\geq$ 2.0	$\geq$2.0
dau1 to dau2 Dca	$\leq$ 0.8	$\leq$ 0.8
Pointing away cut	$>$ 0.	$>$ 0.
V_0 dca	$\leq$ 0.8	$\leq$ 0.7
V_0 decaylength	$\geq$ 6.0	$\geq$ 6.0
$\lvert V_0\ rapidity\rvert$	$\leq$ 0.5	$\leq$ 0.5

3.5.2 Signal & Background Distribution

To reconstruct signal of a V_0 candidate, invariant mass hypothesis was applied.

$$M_{parent} = M_{dau1} + M_{dau2} + 2(E_{dau1}E_{dau2} - \vec{P}_{dau1}\vec{P}_{dau2}). \tag{3.2}$$

For a cascade candidate, we have reconstructed a V_0 first and then combined with a bachelor track. Decay daughters are mentioned in Table 3.5.

As pion and kaon bands merge after 0.6 GeV, so there is possibility of misidentification. A daughter of Ξ^- (which is π^-) may contribute for counts of Ω^- (whose daughter is K^-). To remove this, we have mixed π^- mass with K^- momentum and reconstructed Ω^-. If mass of this reconstructed Ω^- falls within $\pm$ 10 MeV of Ξ^- mass, then we have rejected this track for considering as Ω^-.

Table 3.7: Cascade cuts

Cut	$\Xi^-(\bar{\Xi}^+)$	$\Omega^-(\bar{\Omega}^+)$
V_0 daul Dca	$\geq$1.0	$\geq$1.0
V_0 dau2 Dca	$\geq$2.0	$\geq$2.0
V_0 daul to dau2 Dca	$\leq$ 0.8	$\leq$ 0.8
V_0 Pointing away cut	$>$ 0.	$>$ 0.
V_0 dca	>0.5	>0.5
V_0 decaylength	$\geq$ 6.0	$\geq$ 6.0
Cascade bachelor Dca	>1.0	>1.0
Cascade V_0 to bachelor Dca	<0.8	$<$ 0.6
Cascade pointing away cut	>0.	>0.
Cascade co-linear angle cut	<0.2	$<$ 0.14
Cascade Dca	<0.6	$<$ 0.5
Cascade decaylength	>4.0	$>$ 3.0
|Cascade rapidity |	<0.5	<0.5

For combinatorial background (arrises from mixing of two different parent's daughter) we have used Rotational Method. In this method, we have rotated one of daughter tracks in azimuthal space. This destroys correlation between daughter tracks and give no more signal of the parent track. Fig 3.5 and Fig 3.6 represent one of such plot for signal and background distribution of V_0 and cascade tracks, respectively. Most-central (0-5%) and most-peripheral (60-80%) collision's, all p_T window plots may be found at Sec. 3.9.1.

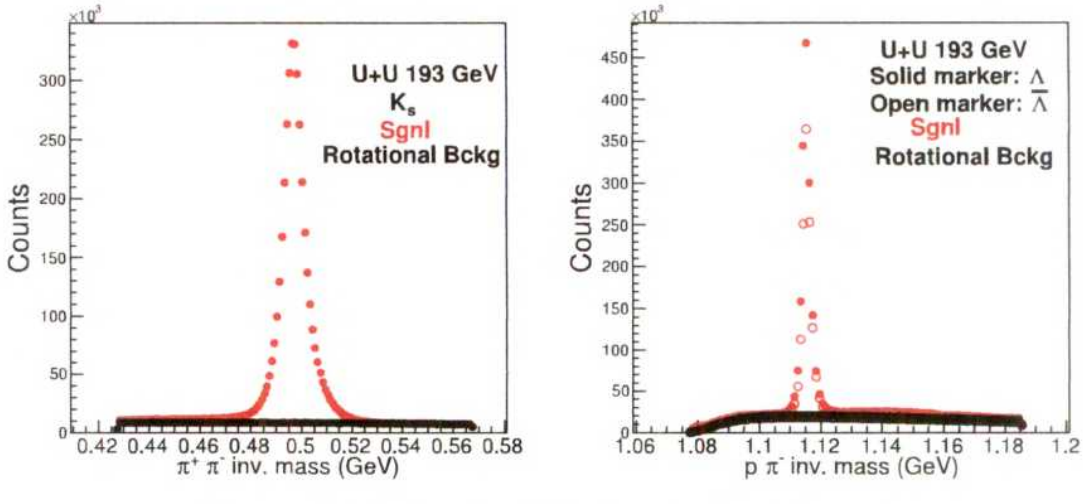

Figure 3.5: V_0 Signal and Background distribution.

For residual background (combinatorial background might not explain all back-

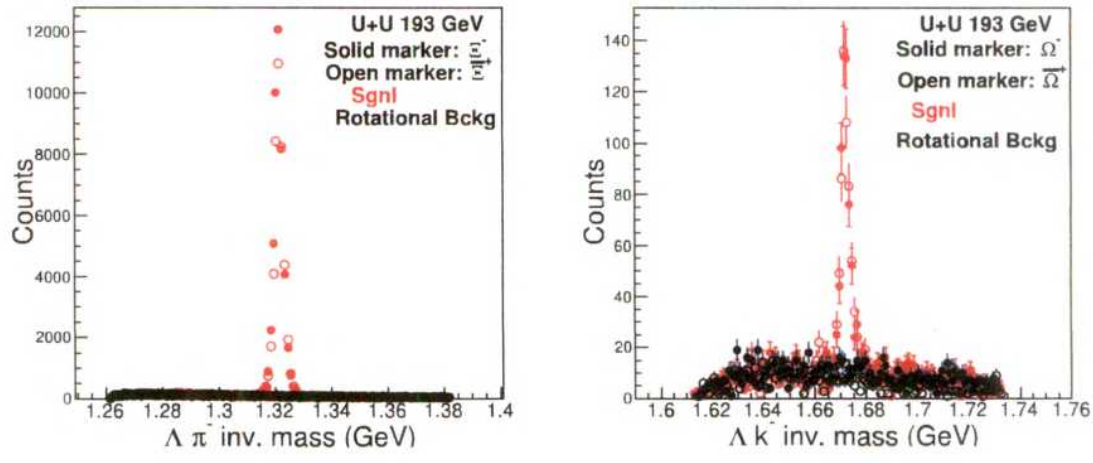

Figure 3.6: Cascade Signal and Background distribution.

ground) estimation, we have adopted sideband technique. In this technique, we define bands (or regions) in signal and background distribution. For this we have used PDG Mass of particle $\pm$ 1σ for signal band, while $1.5 < \sigma < 2.5$ for background bands. Scaling over background from each side of signal, we obtain resultant signal distribution.

We have used bin-counting method to count number of signal tracks. Fig 3.7 and Fig 3.8 represent one of such plot for yield extraction of V_0 and cascade tracks, respectively. Most-central (0-5%) and most-peripheral (60-80%) collision's, all p_T window plots may be found at Sec. 3.9.2.

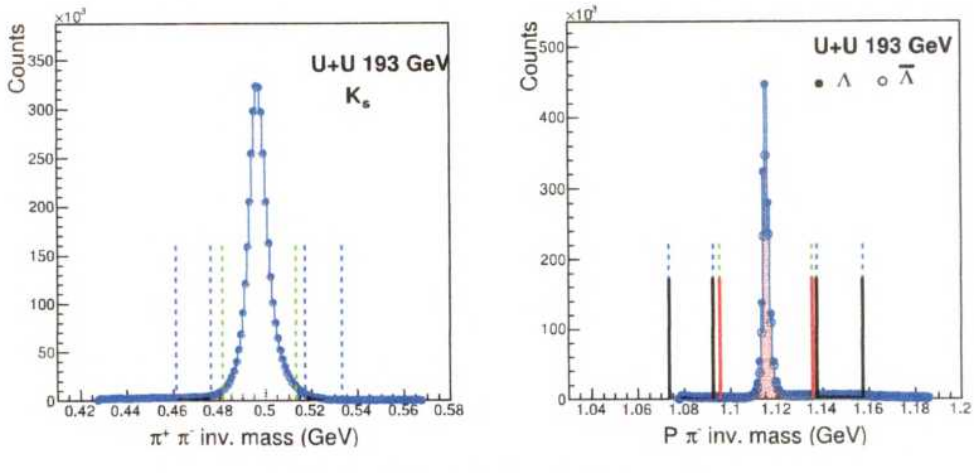

Figure 3.7: V_0 Yield Extraction.

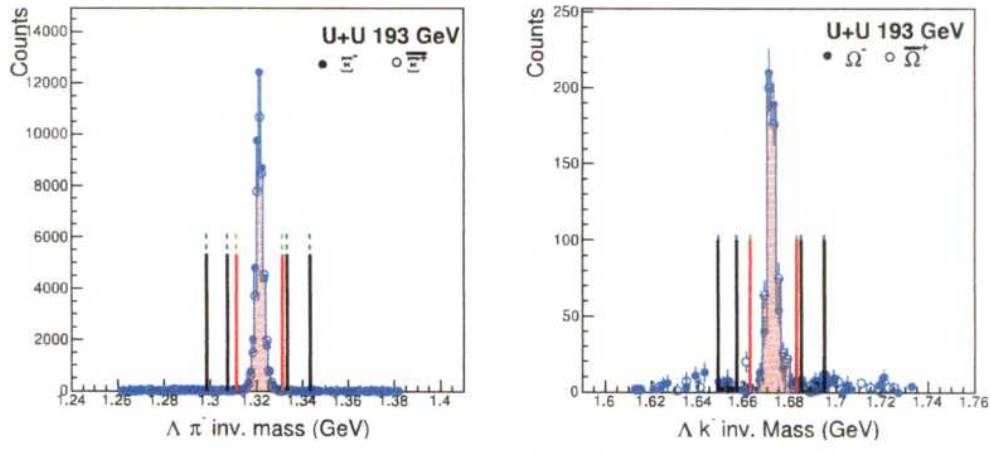

Figure 3.8: Cascade Yield Extraction.

3.5.3 Mass & Width Distribution

From fitting of double Gaussian (signal) with 2nd order polynomial (background) to raw spectra, we got required values of mass and width. Fig 3.9 and Fig 3.10 represent mass and width distribution of V_0 and cascade particles in most central collision (0-5%), respectively.

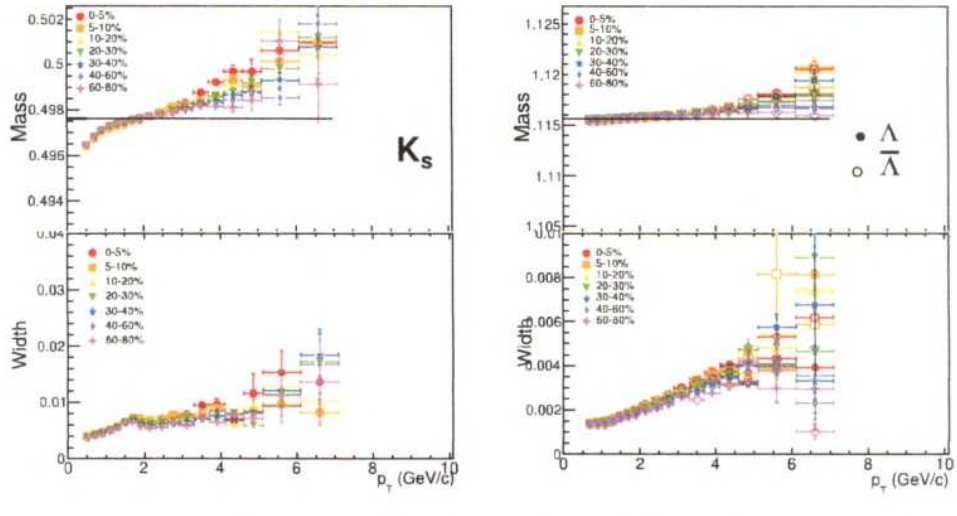

Figure 3.9: V_0 Mass and Width distribution for different centralities.

The observed mass shift might partially arise from the interaction between the outgoing particles from collisions and the materials close to the beam line in the detector. Although natural width of these particles are of the order keV, for finite momentum resolution of TPC, we observe them in higher values. However, both of

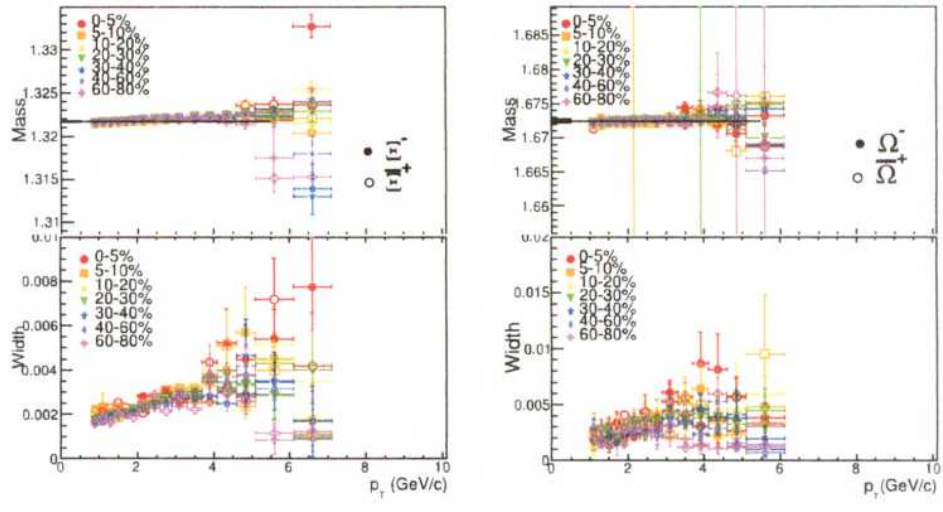

Figure 3.10: Cascade Mass and Width distribution for different centralities.

them almost independent of centrality.

3.6 Raw Spectra

By following method as described in Section 3.5.2 for all p_T and centrality window, we can count number of signal tracks. Raw spectra of a track is obtained after normalising this yield, over number of events & other variables over which the counting is done (viz p_T, rapidity, bin width).

Fig 3.11 and Fig 3.12 present raw spectra of V_0 and cascade candidate in seven different centrality, respectively.

3.7 Corrections to Raw Spectra

STAR uses GEANT simulation (GEometry ANd Tracking) [10] for embedding studies. At first, one need to generate tracks using Monte Carlo simulation at first [11], then these tracks are mixed with data tracks. Later this sample pass through reconstruction software (GSTAR and TRS) and it convert MC hits to real ones. Once we have results, we need to do track reconstruction, matching to detectors (MTD/TOF/TPC etc) and to create calorimeter hits.

GSTAR [12] is a framework to run STAR detector simulation using GEANT.

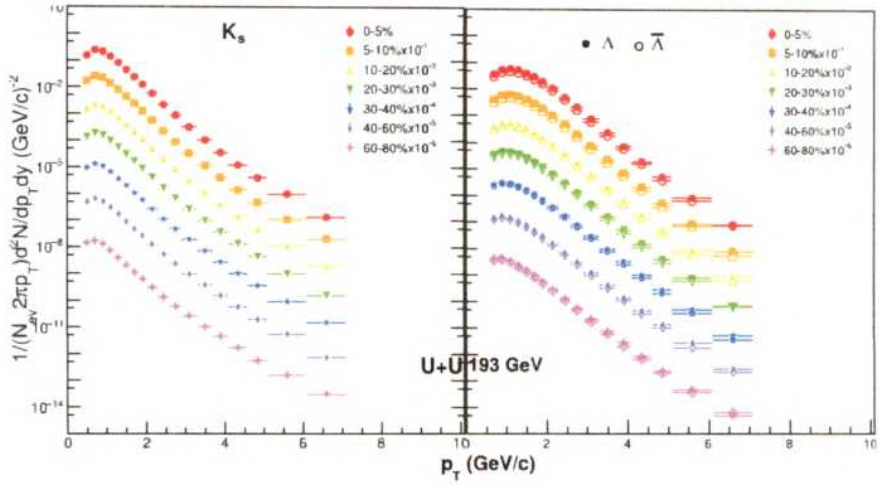

Figure 3.11: V_0 raw spectra for different centralities.

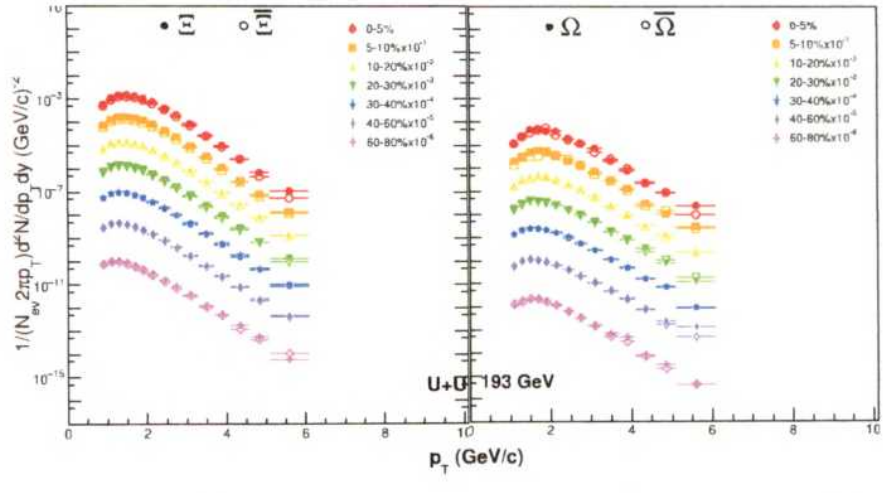

Figure 3.12: Cascade raw spectra for different centralities.

This consist of set of codes which contain informations on geometry of STAR detectors/procedures to perform I/O operations, particle generations and in-flight analysis [13]. Input to GSTAR is a tex file containing information regarding geometry of different detectors and other informations. Output file from GSTAR contains information on vertex/hit/track tables in a tabular form.

TRS [14] software simulates STAR TPC response to charged particles within gas volume of TPC. This involves amplification on sense wires, induction of signals on readout pads, drift of ionised electrons in gas and response of readout electronics. Input to TRS are hits from GEANT simulation. TRS's major evaluation is done

by comparing characteristics of pixels/hits/tracks with real data [13]. We have compared produced embedding samples with real data and they are presented in Fig 3.13 to Fig 3.16. We see there is good agreement between produced embedding files and real data.

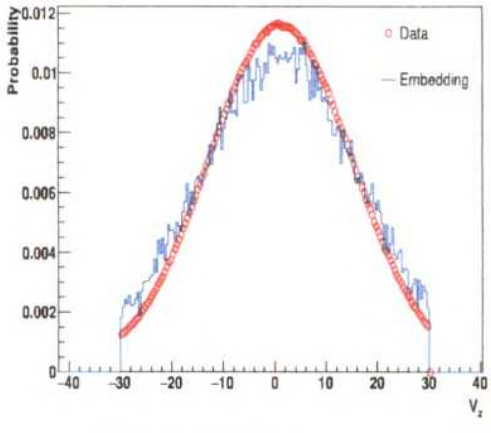

V_z comparison

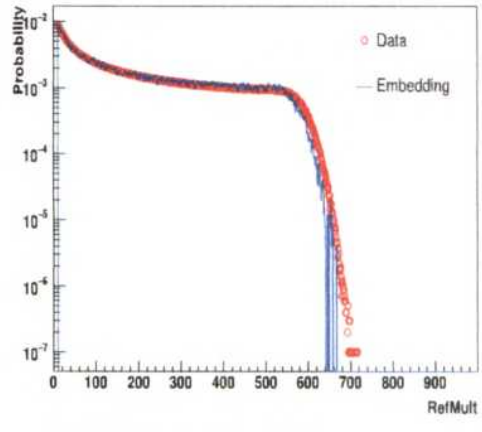

RefMult comparison

Figure 3.13: Comparison of embedding to data event variables.

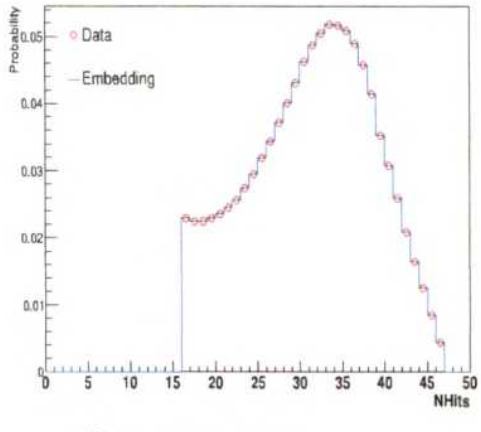

nHits comparison

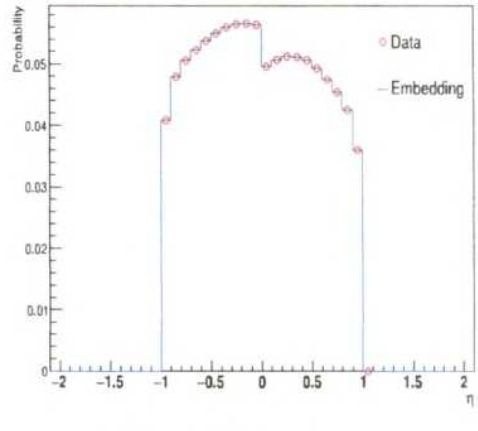

η comparison

Figure 3.14: Comparison of embedding to data track variables.

In Fig 3.17 and Fig 3.18, we have plotted efficiency $\times$ acceptance factor for V_0 and cascade tracks, respectively. Solid marker represents particles and open one's are for anti-particle. These efficiency corrections are applied to raw spectra bin by bin.

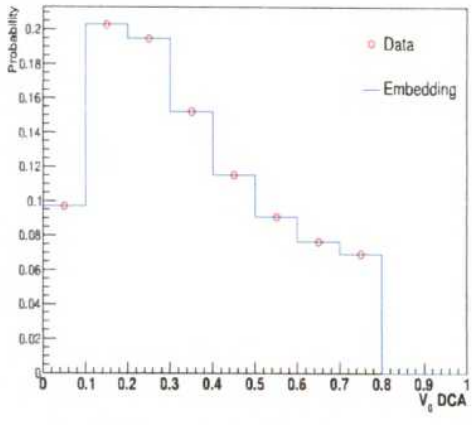

K_s DCA comparison

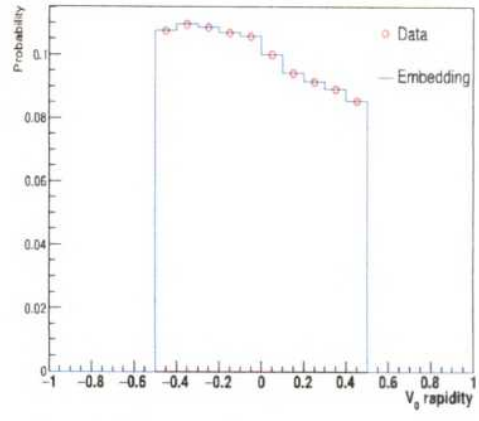

K_s rapidity comparison

Figure 3.15: Comparison of embedding to data V_0 analysis variables.

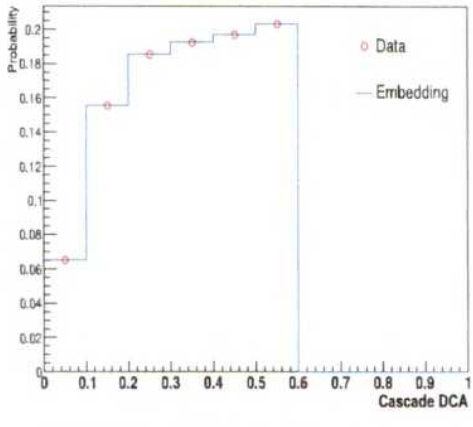

Ξ DCA comparison

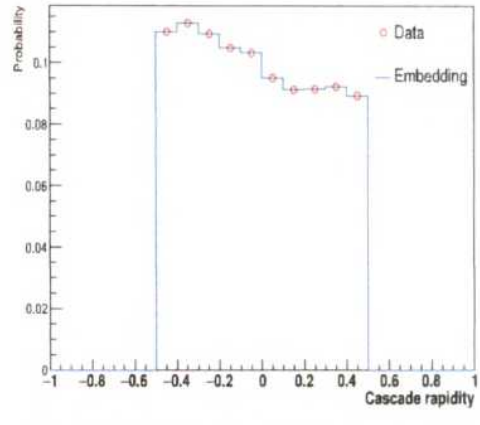

Ξ rapidity comparison

Figure 3.16: Comparison of embedding to data Cascade analysis variables.

3.8 Results

3.8.1 Corrected Spectra

In Fig 3.19 we have presented p_T spectra of K_s, Λ and $\bar{\Lambda}$ for U+U collisions at $\sqrt{s_{NN}} = 193$ GeV. Seven different centralities are presented in different colours and markers as shown in legend. In right hand figure, Λ are presented in solid markers, while $\bar{\Lambda}$ are presented in open markers. From top to bottom, we plotted decreasing in centrality, from most central (0-5%) to most peripheral (60-80%). Here we see a clear centrality dependence. We have p_T of 7 GeV/c.

Fig 3.20 is similar as of Fig 3.19, but for $\Xi, \bar{\Xi}, \Omega$ and $\bar{\Omega}$. Here we have p_T is

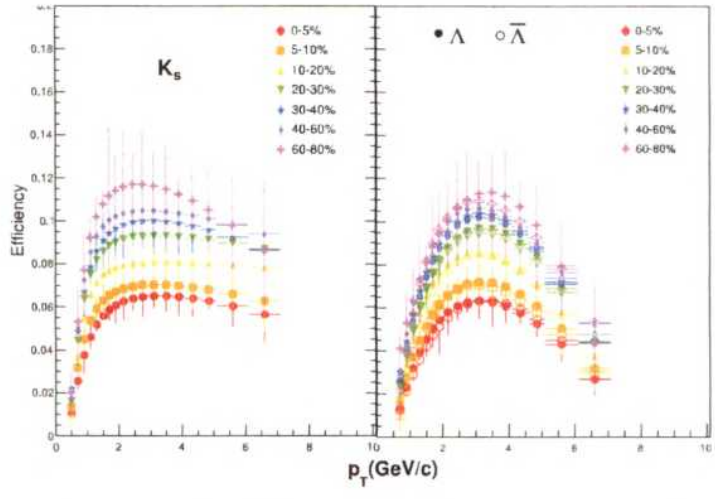

Figure 3.17: V_0 Efficiency for different centralities.

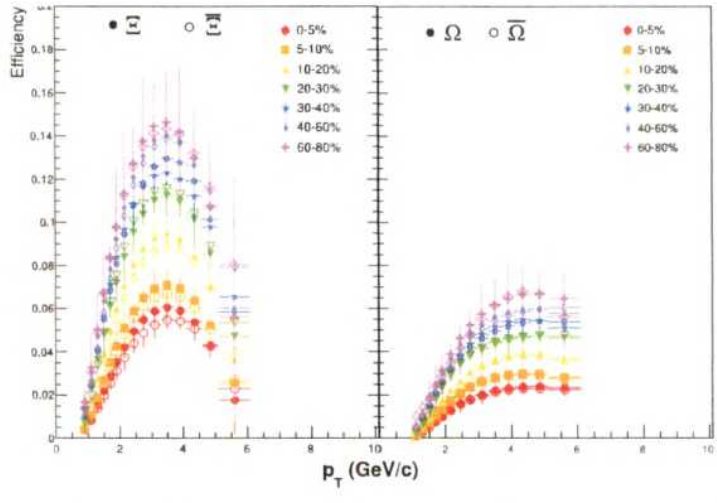

Figure 3.18: Cascade Efficiency for different centralities.

limited from that of V_0 tracks. We see here centrality dependence of p_T spectra as seen for V_0 tracks.

From both of figures, Fig 3.19 and Fig 3.20, we observe particles and anti-particles yields are of similar order.

3.8.2 Nuclear Modification Factor

Nuclear Modification factor may be defined as following:

$$R_{AA} = \frac{(d^2N/dp_T dy)^{AA}}{< T_{AA} > (d^2\sigma_{INEL}/dp_T dy)^{pp}}. \tag{3.3}$$

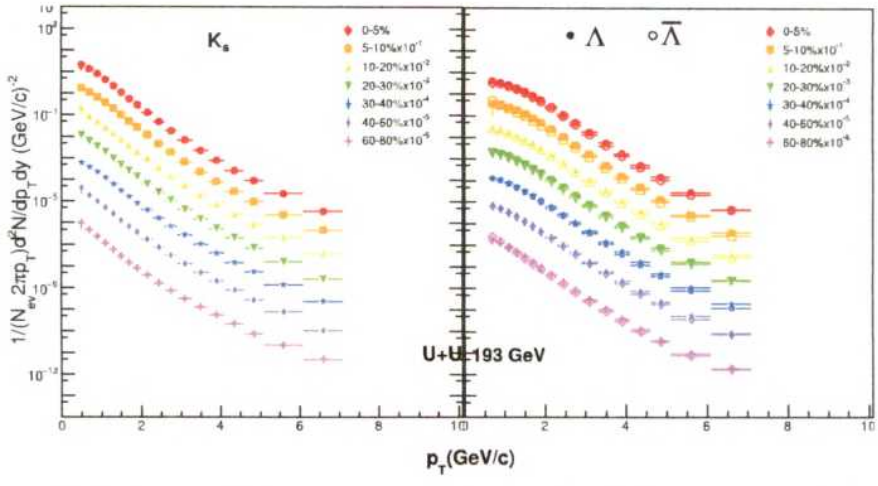

Figure 3.19: V_0 corrected p_T spectra for different centralities.

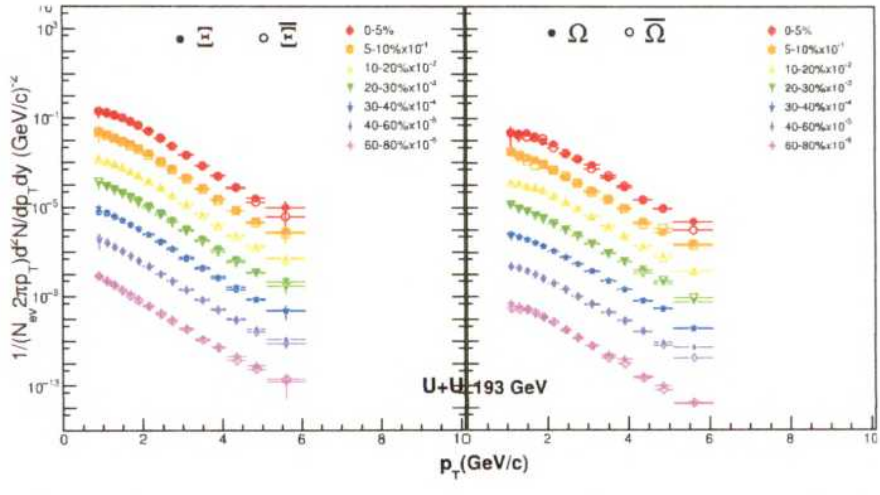

Figure 3.20: Cascade corrected p_T spectra for different centralities.

Where N_{AA} representes particle yield in nucleus-nucleus collision and σ^{pp}_{INEL} represents in-elastic cross-section in pp collisions.

$< T_{AA} >$ represents nuclear overlap function and may be defined as:

$$< T_{AA} >=< N_{coll} > /\sigma^{NN}_{INEL}. \tag{3.4}$$

In the absence of pp collision data, alternatively we can define R_{CP} as following:

$$R_{CP} = \frac{d^2N/dp_T dy/ < N^{cent}_{coll} >}{d^2N/dp_T dy/ < N^{Perph}_{coll} >}. \tag{3.5}$$

Where $< N_{coll}^{cent} >$ and $< N_{coll}^{Perph} >$ are average number of binary collisions in central and peripheral collisions.

In the absence of any nuclear matter effect, this will be unity.

In Fig 3.21, we have plotted R_{CP} as a function of p_T for K_s, $\Lambda(\bar{\Lambda})$, $\Xi(\bar{\Xi})$ *and* $\Omega(\bar{\Omega})$. Solid marker represent particles and open marker are for anti-particles. We observe they are actually less than unity. Our results are consistent with published Au+Au 200 GeV results [15, 16]. We also observe that anti-particles and particles are modified in the medium of similar order. However, we observe small dependence of R_{CP} with strangeness content. We observe hierarchy in strangeness content with R_{CP} of particle; i.e $K_s < \Lambda < \Xi < \Omega$.

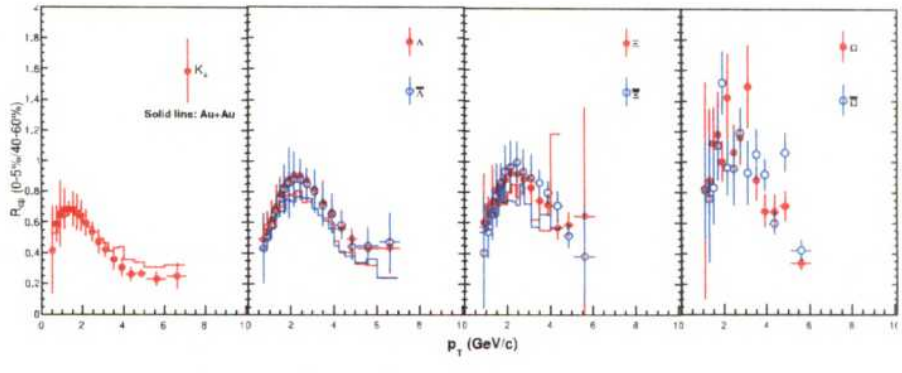

Figure 3.21: Nuclear Modification factor

3.8.3 Particle Ratio

In Fig 3.22 we have plotted anti-particle to particle ratios, viz $\bar{\Lambda}/\Lambda$, $\bar{\Xi}/\Xi$ and $\bar{\Omega}/\Omega$. We have shown results for most central and most peripheral collision (we choose 40-60% for statistics reason). We observe that the ratio values around 0.9. We found that they are independent of centrality and independent of hierarchy in strangeness content.

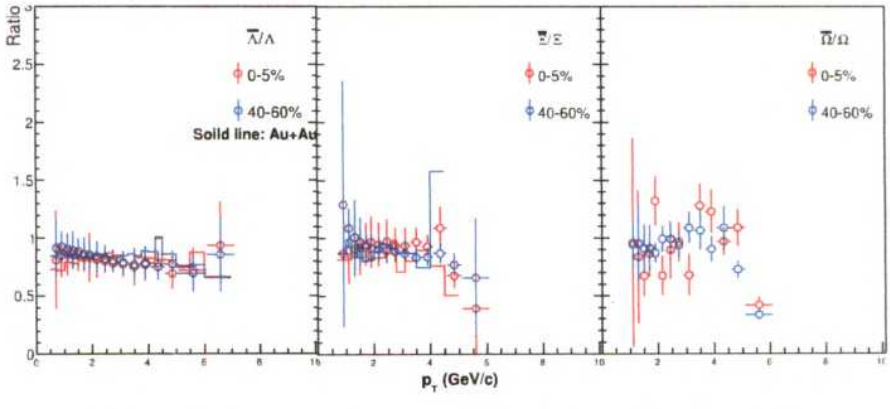

Figure 3.22: Anti-Particle to Particle ratio distribution

Bibliography

[1] http://www.star.bnl.gov/protected/bulkcorr/hmasui/2013/Centrality_UU_193GeV/hmasui_centrality_UU_200GeV_bulkcorr_Mar20_2013.pdf

[2] D. Kharzeev and M. Nardi, Phys. Lett. B 507, 121,2001

[3] https://drupal.star.bnl.gov/STAR/blog/yezhenyu/nbinary-and-npart-uu-collisions-zhenyu

[4] https://drupal.star.bnl.gov/STAR/system/files/Calibs_status_Winter14.pdf

[5] https://drupal.star.bnl.gov/STAR/system/files/kxin_embedding_Collaboration_BNL_20140214-4.pdf

[6] https://drupal.star.bnl.gov/STAR/blog/genevb/2013/jul/31/rt-2495-notes

[7] https://drupal.star.bnl.gov/STAR/system/files/userfiles/3639/tcut.png

[8] https://inspirehep.net/record/871877/files/cascadeGraph.png

[9] H. Bichsel, Nucl. Instr. and Meth. A 562,154 (2006).

[10] Brun, R. et al. CERN-DD-EE-84-1

[11] https://drupal.star.bnl.gov/STAR/comp/simu/star-simulation-framework

[12] http://www.star.bnl.gov/public/comp/simu/newsite/gstar/Manual/main_manual.html

[13] PhD thesis, Hui Long, UCLA, 2002

[14] B Lasiuk, The Physics of the TPC Response Simulator, STAR note, www.star.bnl.gov/public/comp/simu/TpcRespSim/src/papers/trs_prelim.ps

[15] G. Agakishiev et al. (STAR Collaboration), Phys. Rev. Lett. 108, 072301, 2012

[16] J. Adams et al. (STAR Collaboration), Phys. Rev. Lett. 98, 062301, 2007

3.9 Appendix

3.9.1 Signal and Background distribution

Here we are presenting signal (red marker) and combinatorial background (black marker) in most central (0-5%) and most peripheral (60-80%) collision centralities. On the top of each plot p_T window is presented.

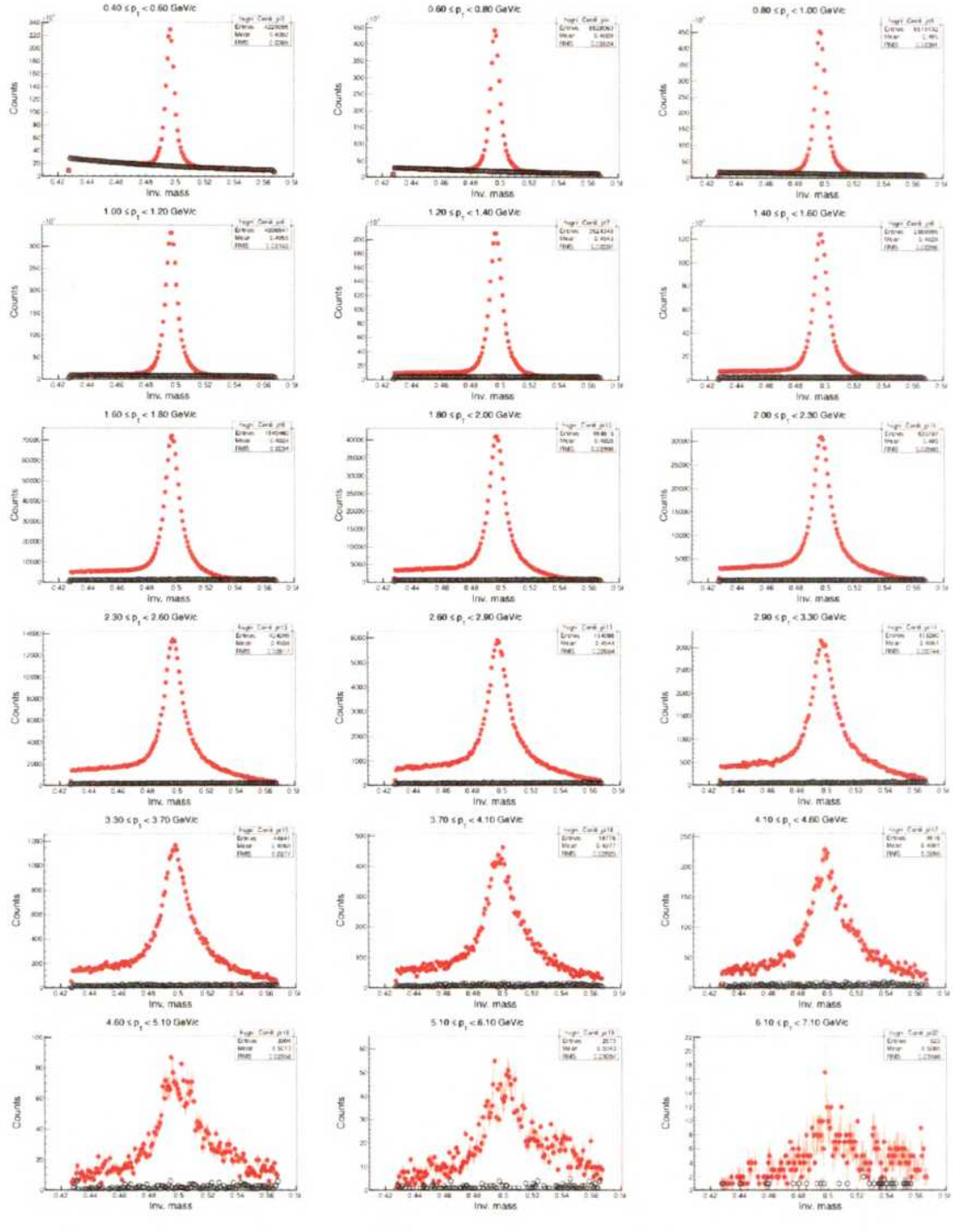

Figure 3.23: K_s Signal and Background distribution in 0-5% centrality.

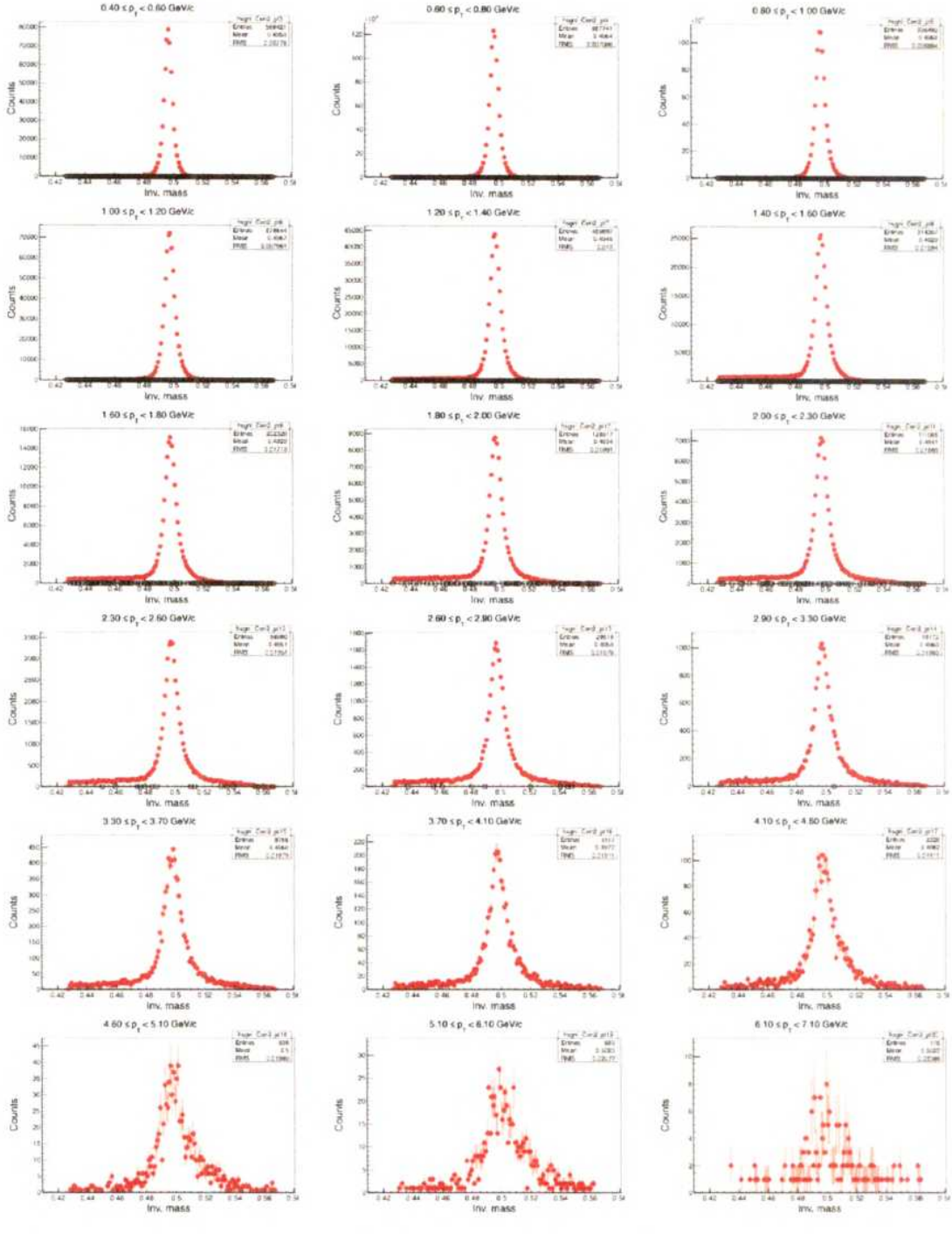

Figure 3.24: K_s Signal and Background distribution in 60-80% centrality.

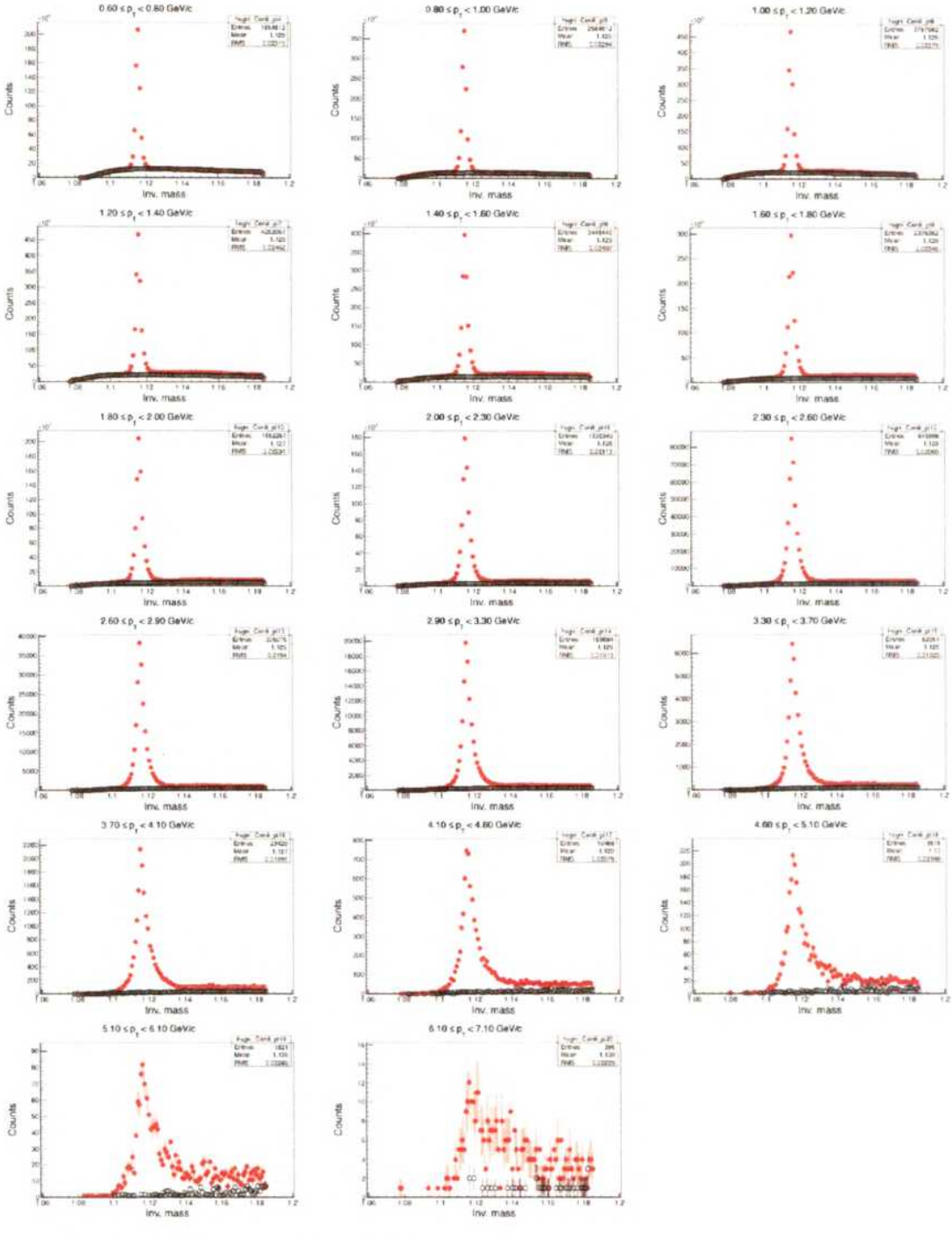

Figure 3.25: Λ Signal and Background distribution in 0-5% centrality.

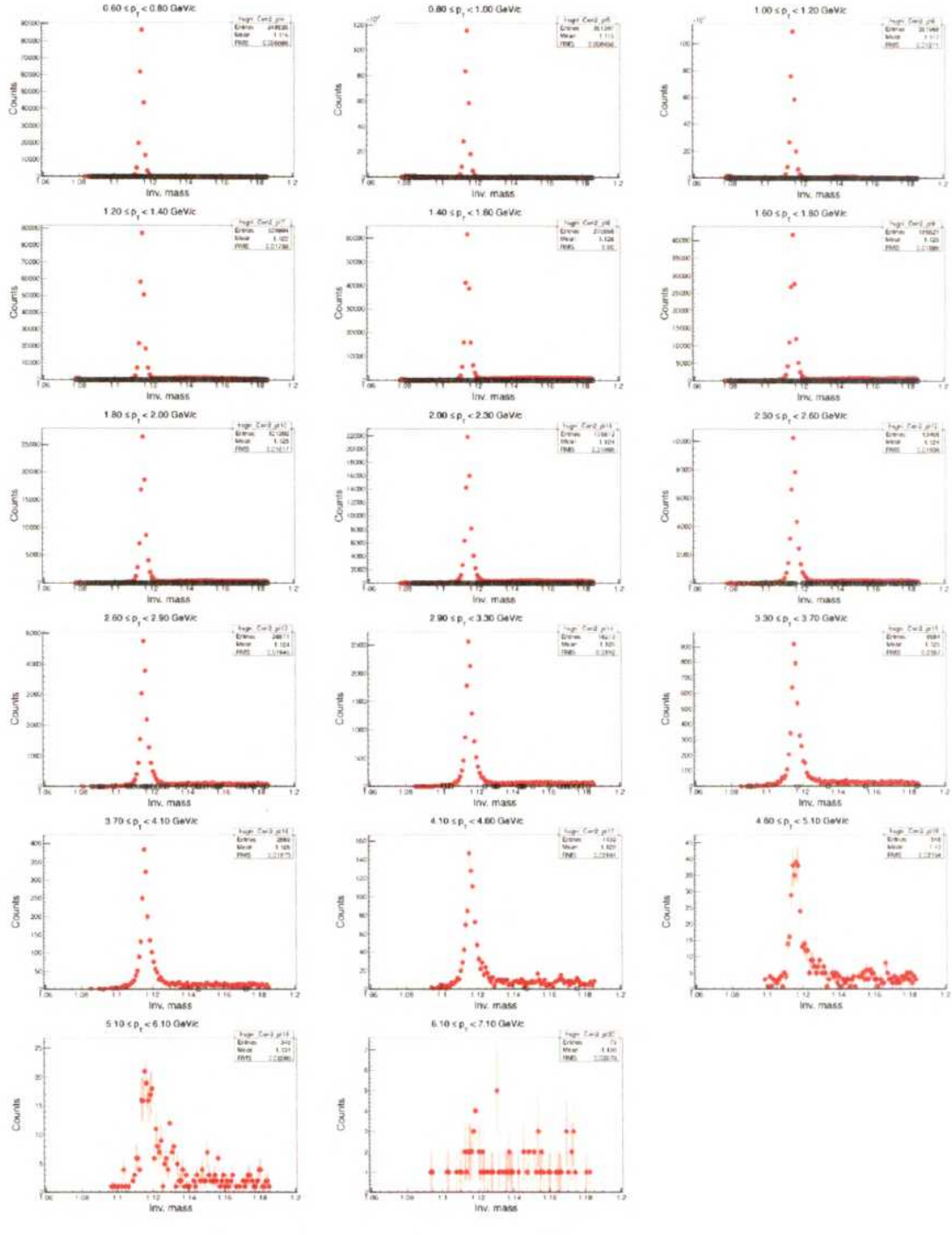

Figure 3.26: Λ Signal and Background distribution in 60-80% centrality.

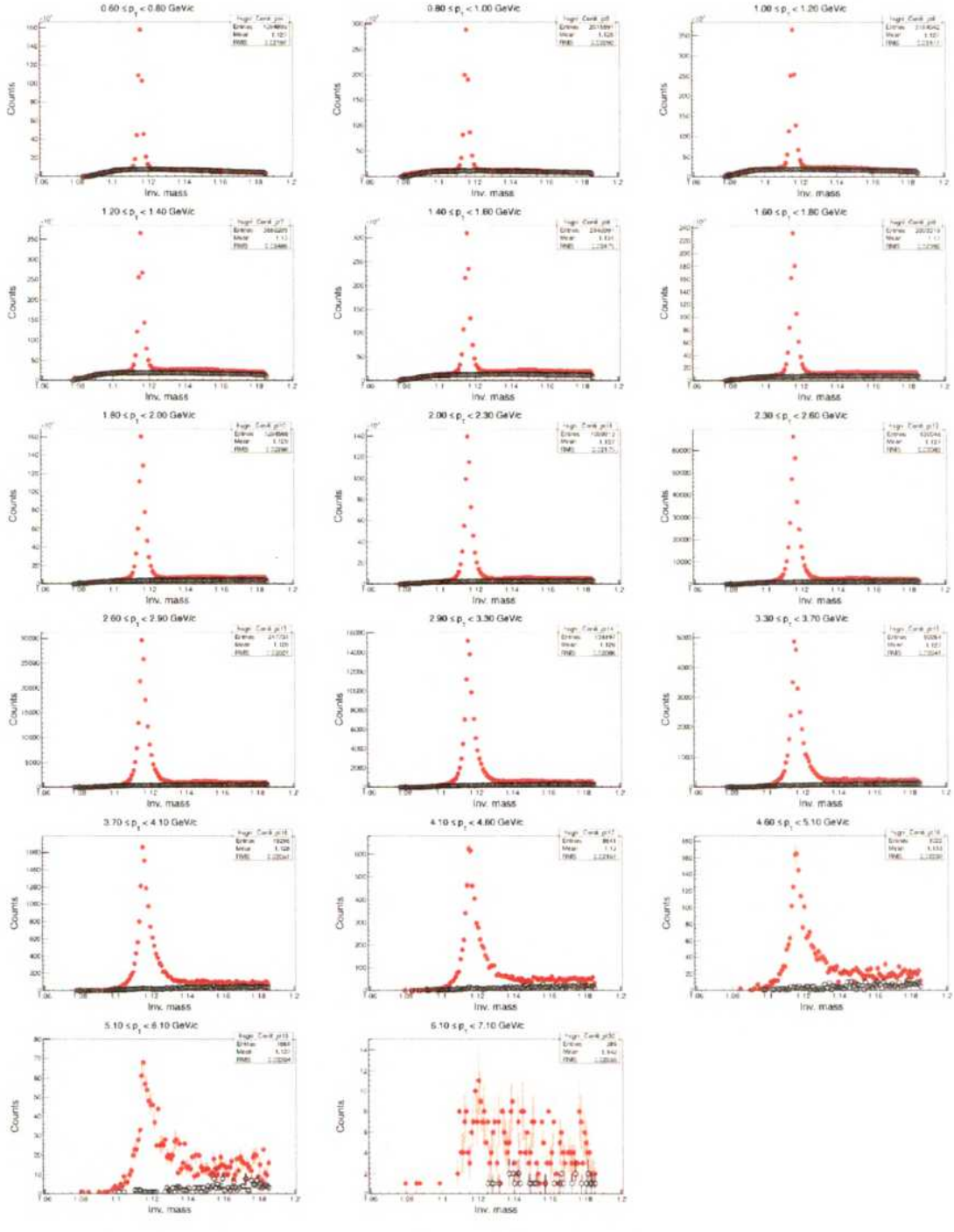

Figure 3.27: $\bar{\Lambda}$ Signal and Background distribution in 0-5% centrality.

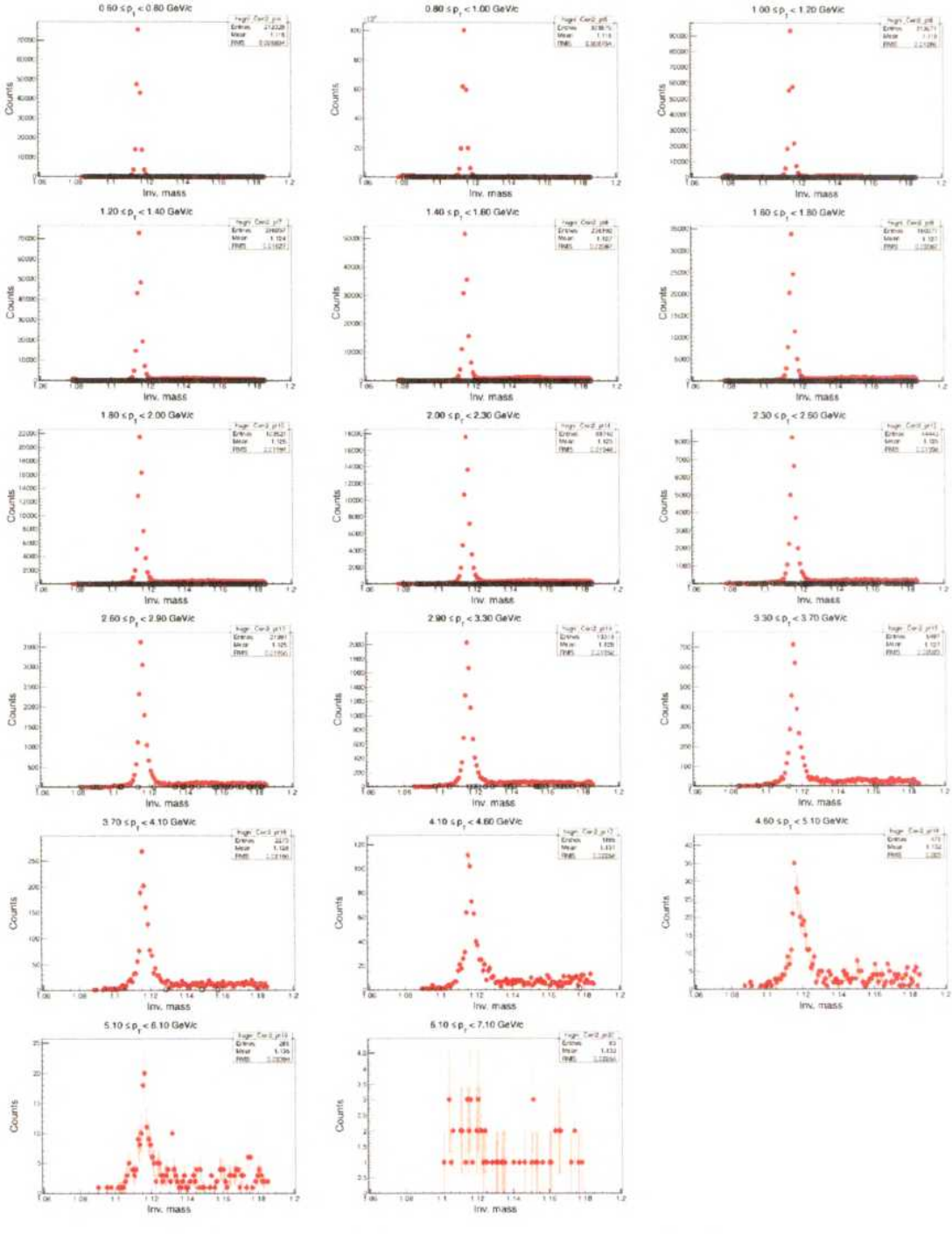

Figure 3.28: $\bar{\Lambda}$ Signal and Background distribution in 60-80% centrality.

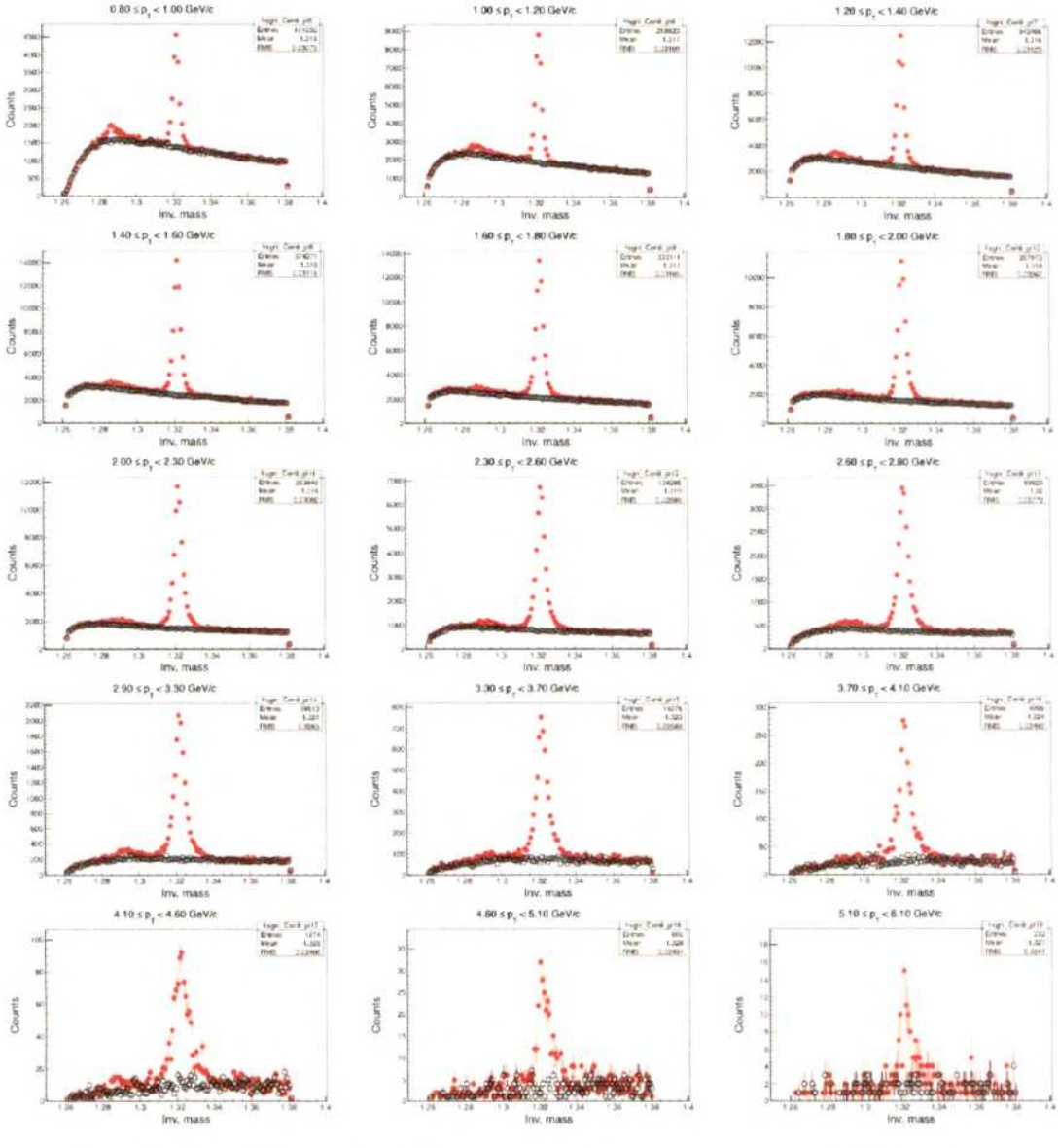

Figure 3.29: Ξ Signal and Background distribution in 0-5% centrality.

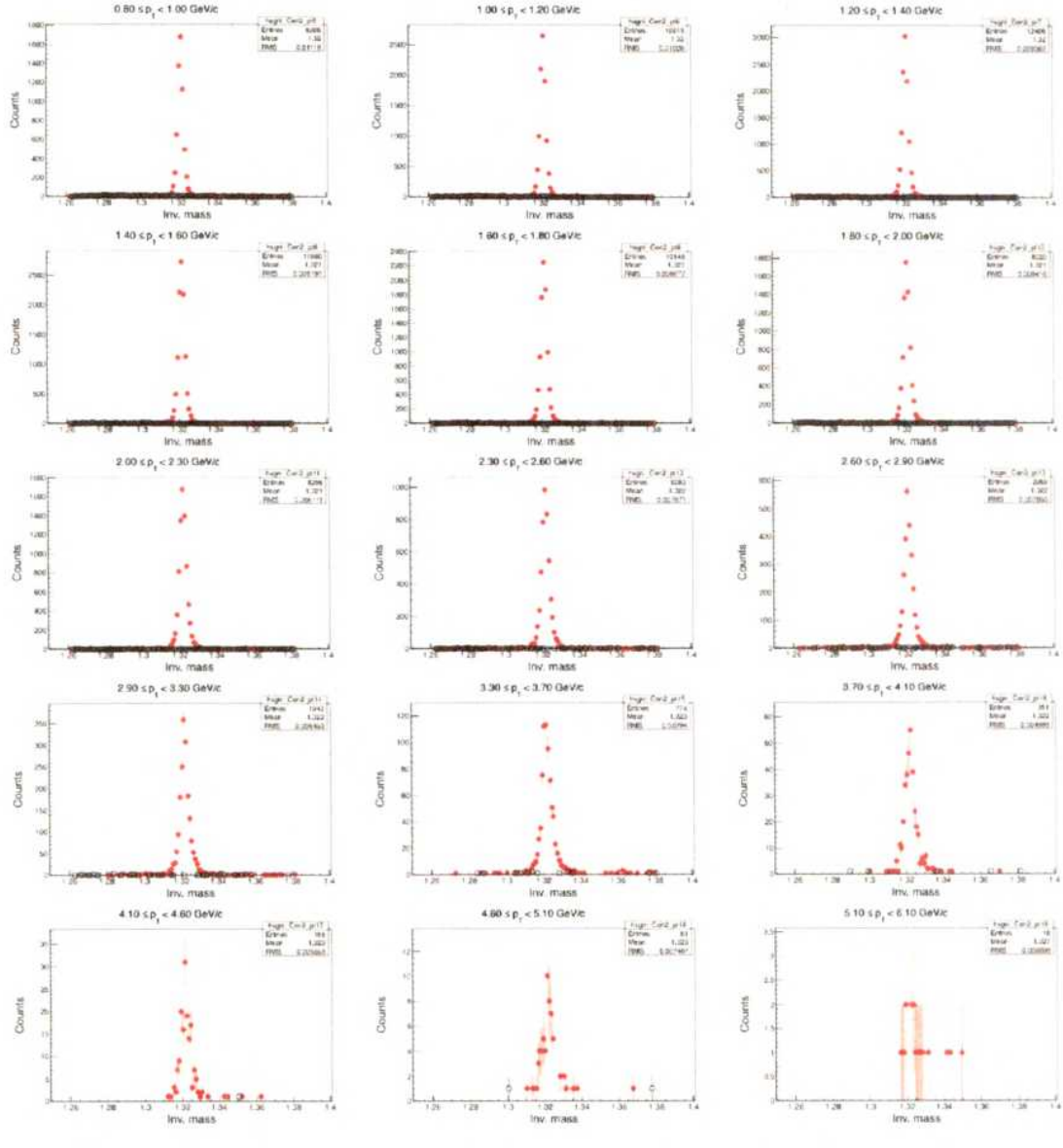

Figure 3.30: Ξ Signal and Background distribution in 60-80% centrality.

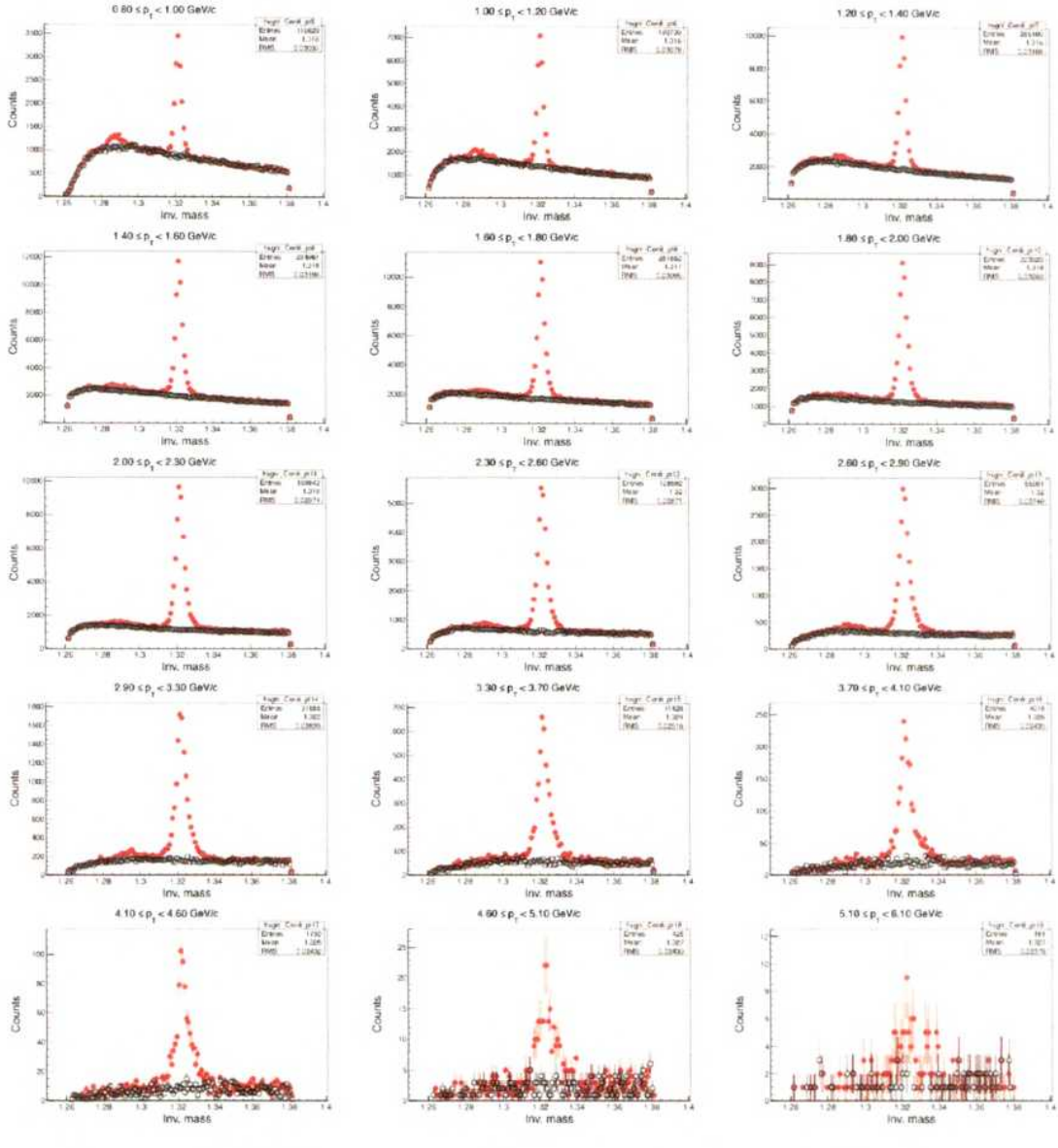

Figure 3.31: $\bar{\Xi}$ Signal and Background distribution in 0-5% centrality.

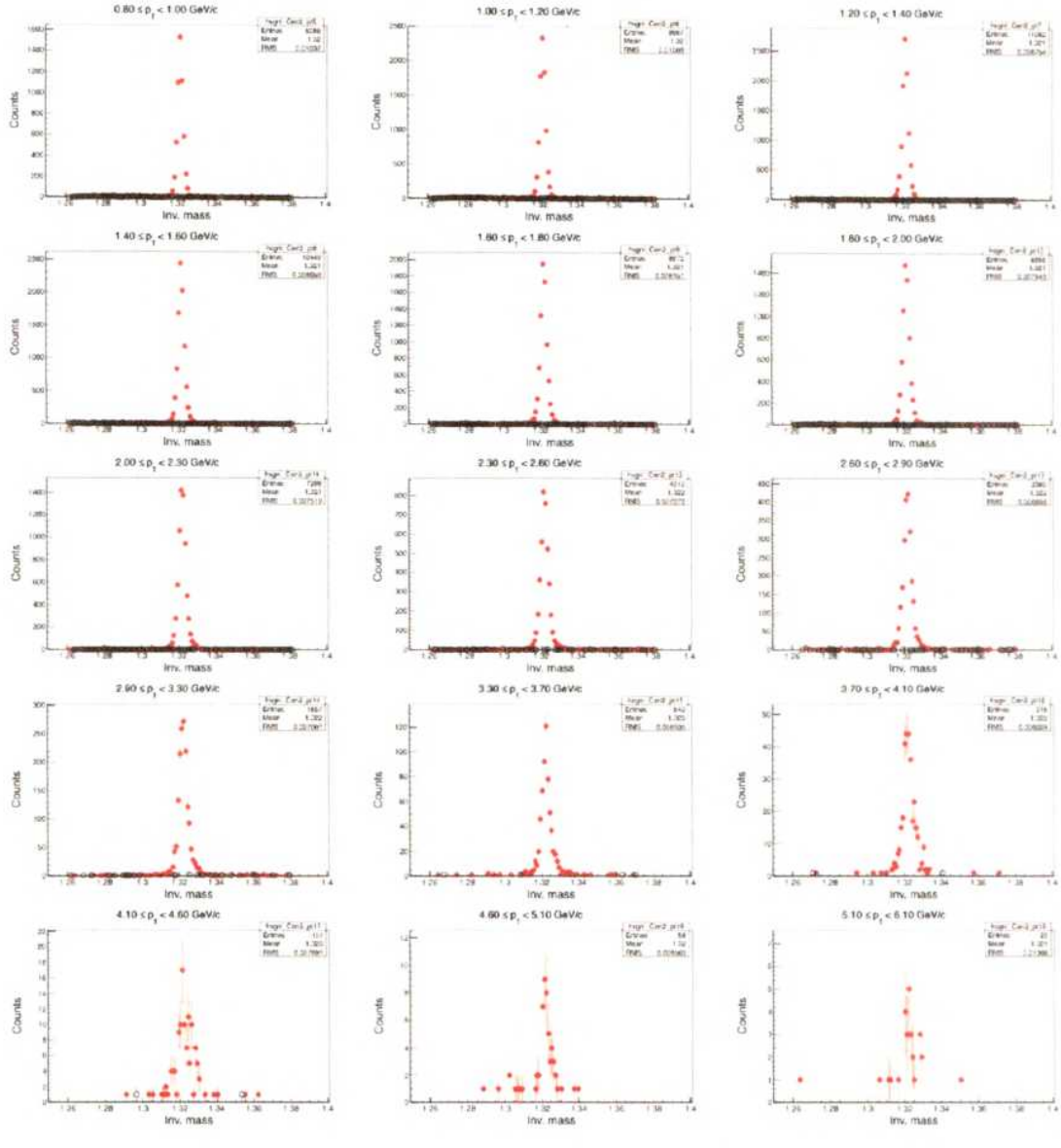

Figure 3.32: $\bar{\Xi}$ Signal and Background distribution in 60-80% centrality.

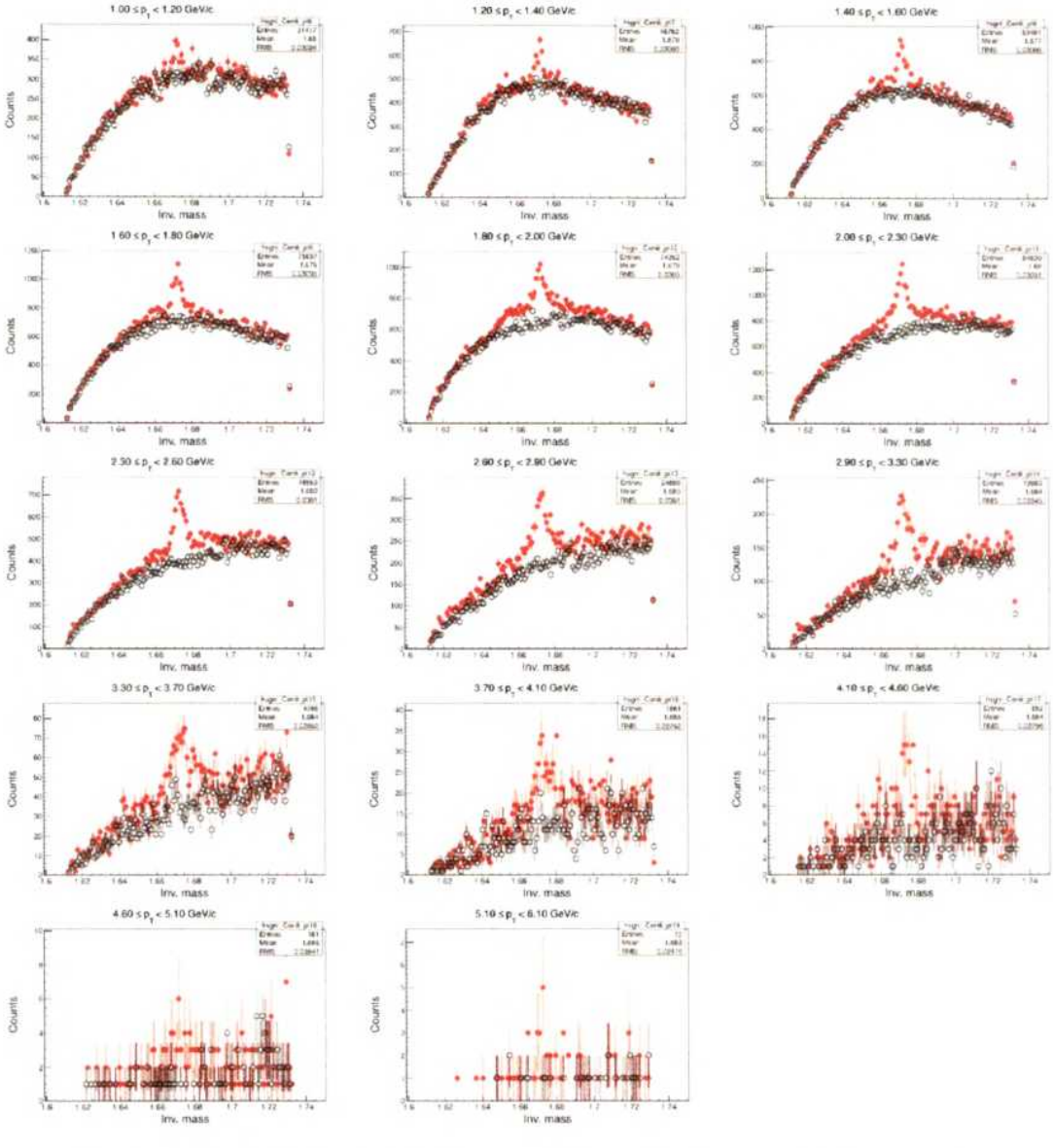

Figure 3.33: Ω Signal and Background distribution in 0-5% centrality.

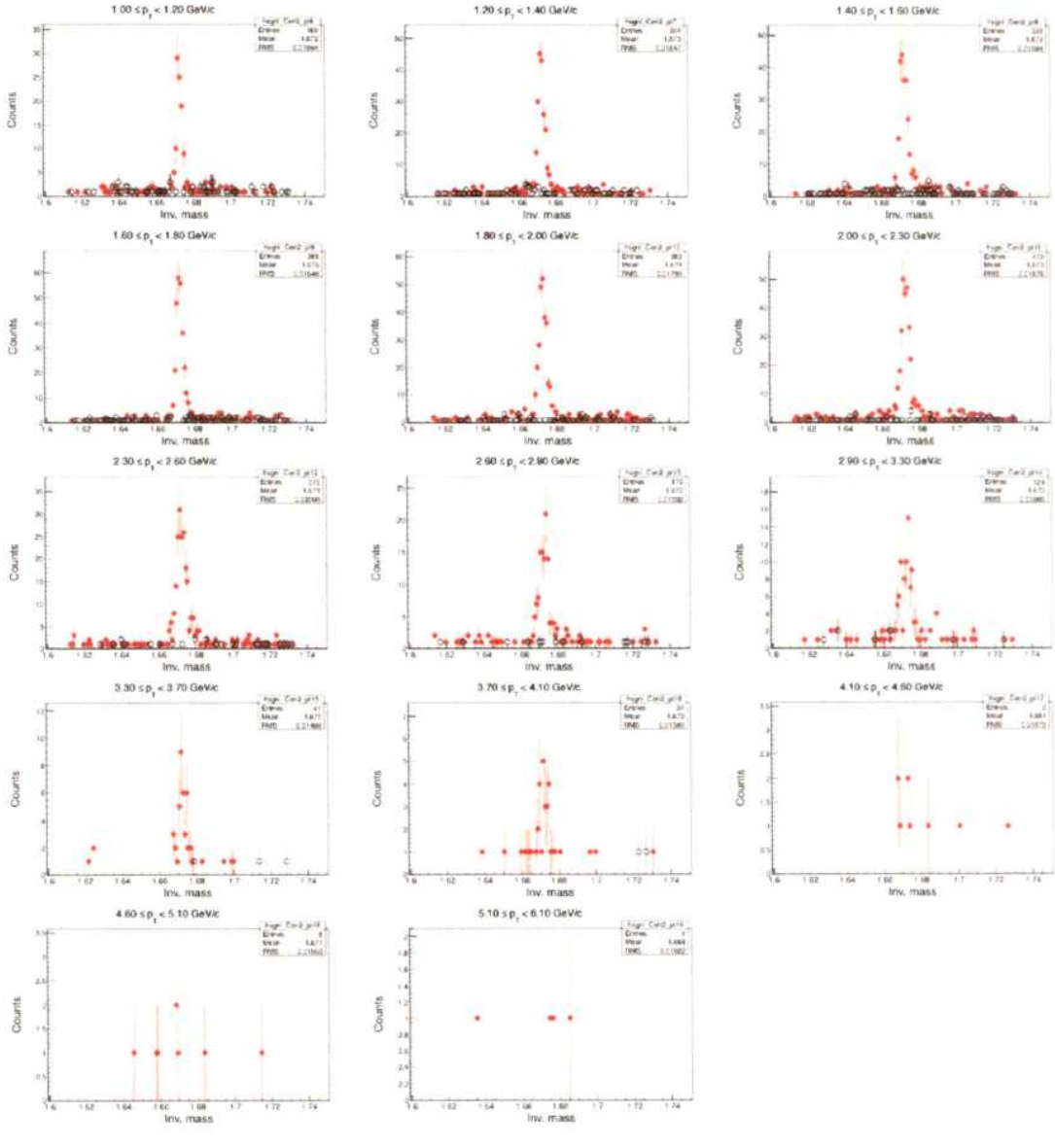

Figure 3.34: Ω Signal and Background distribution in 60-80% centrality.

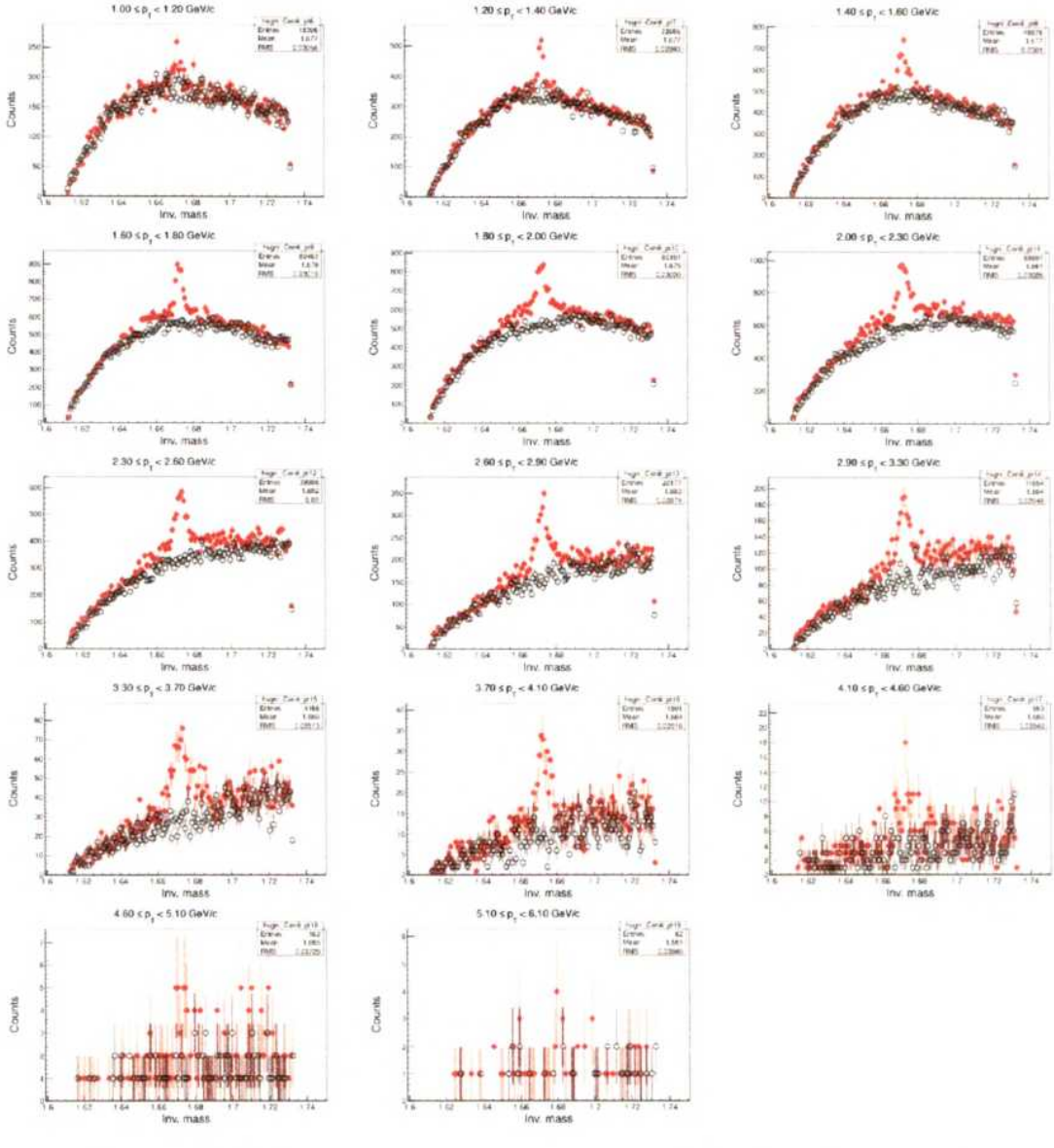

Figure 3.35: $\bar{\Omega}$ Signal and Background distribution in 0-5% centrality.

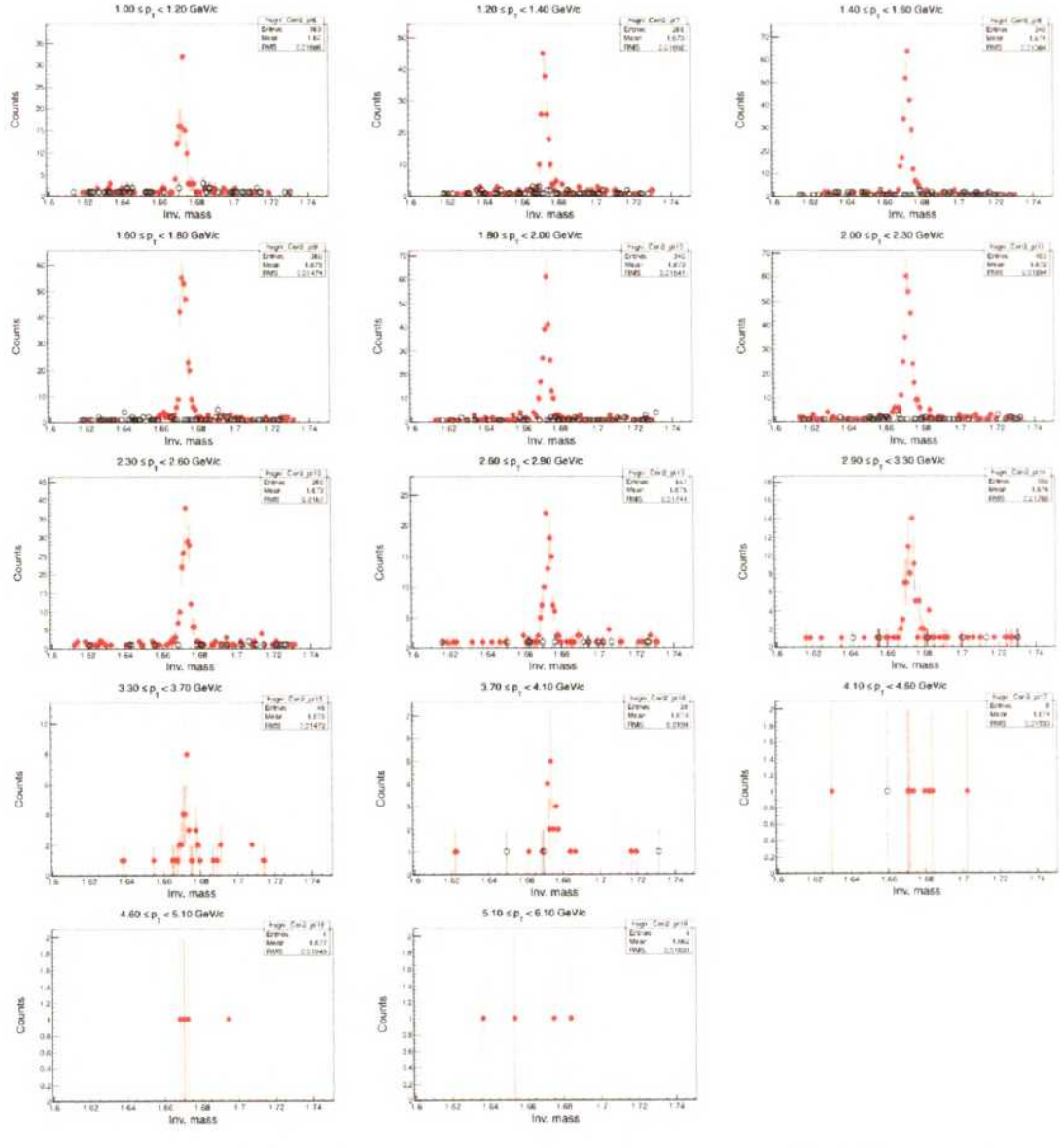

Figure 3.36: $\bar{\Omega}$ Signal and Background distribution in 60-80% centrality.

3.9.2 Signal distribution

Here we are presenting signal (green band) and residual background (black band) in most central (0-5%) and most peripheral (60-80%) collision centralities. On the top of each plot p_T window is presented.

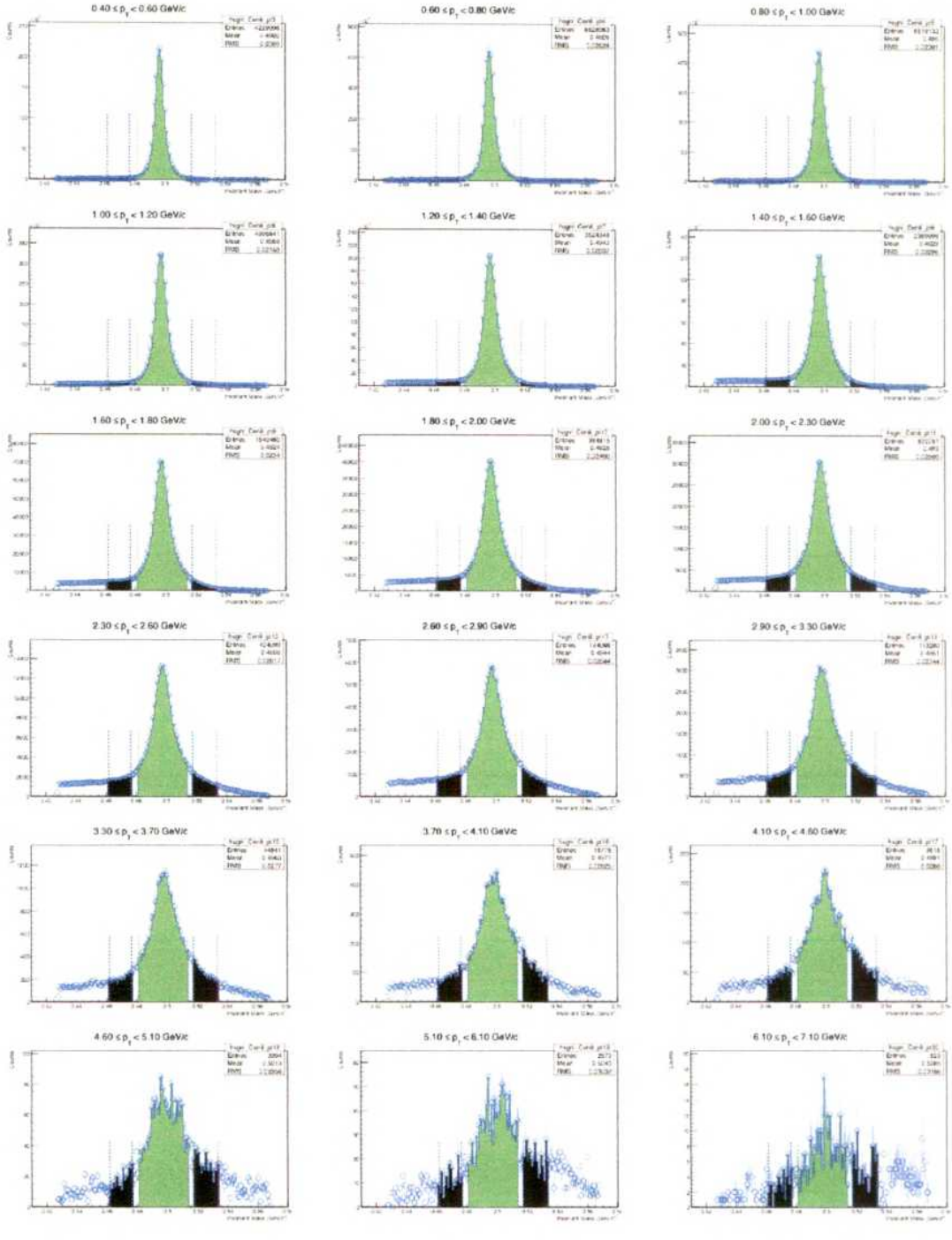

Figure 3.37: K_s Signal distribution in 0-5% centrality.

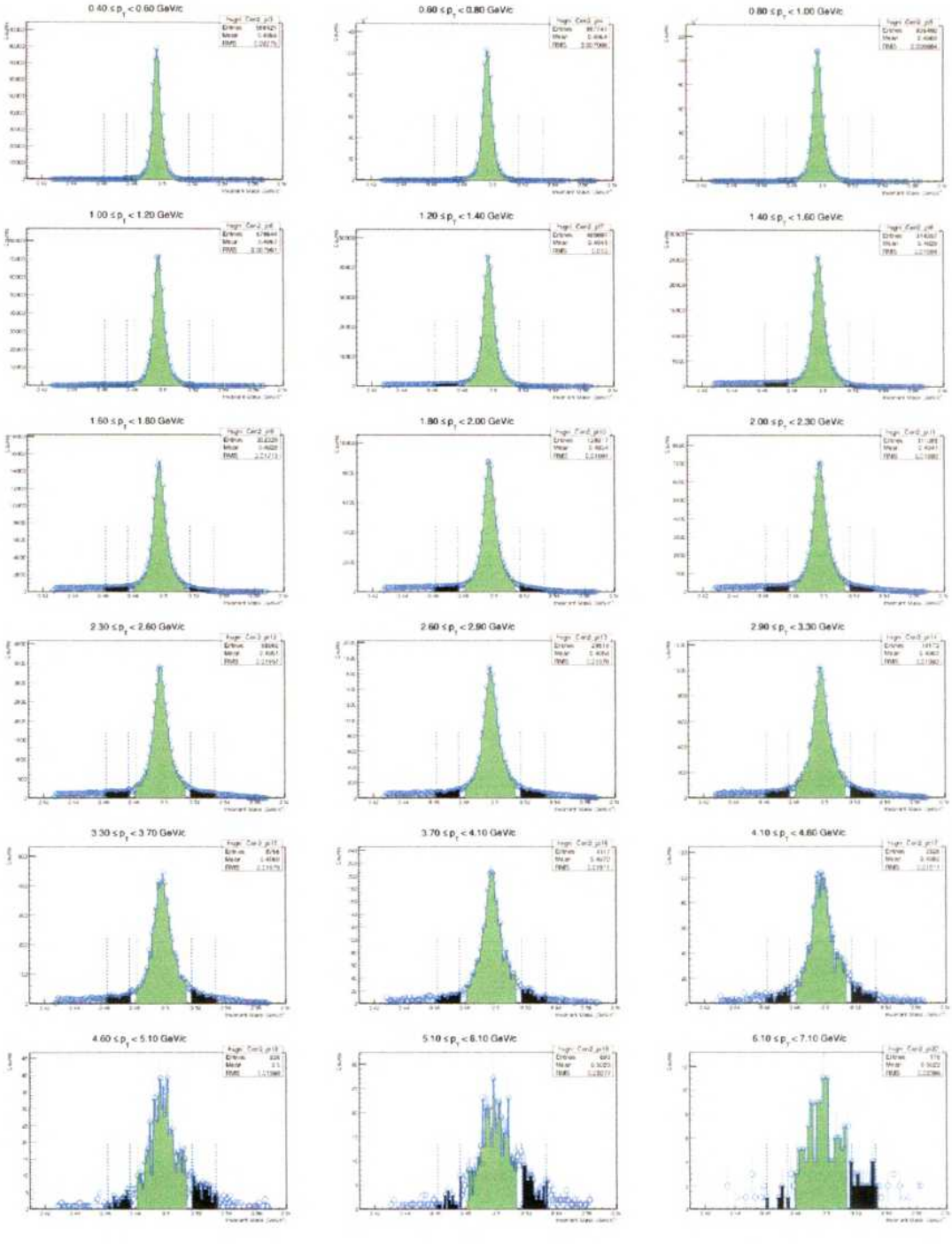

Figure 3.38: K_s Signal distribution in 60-80% centrality.

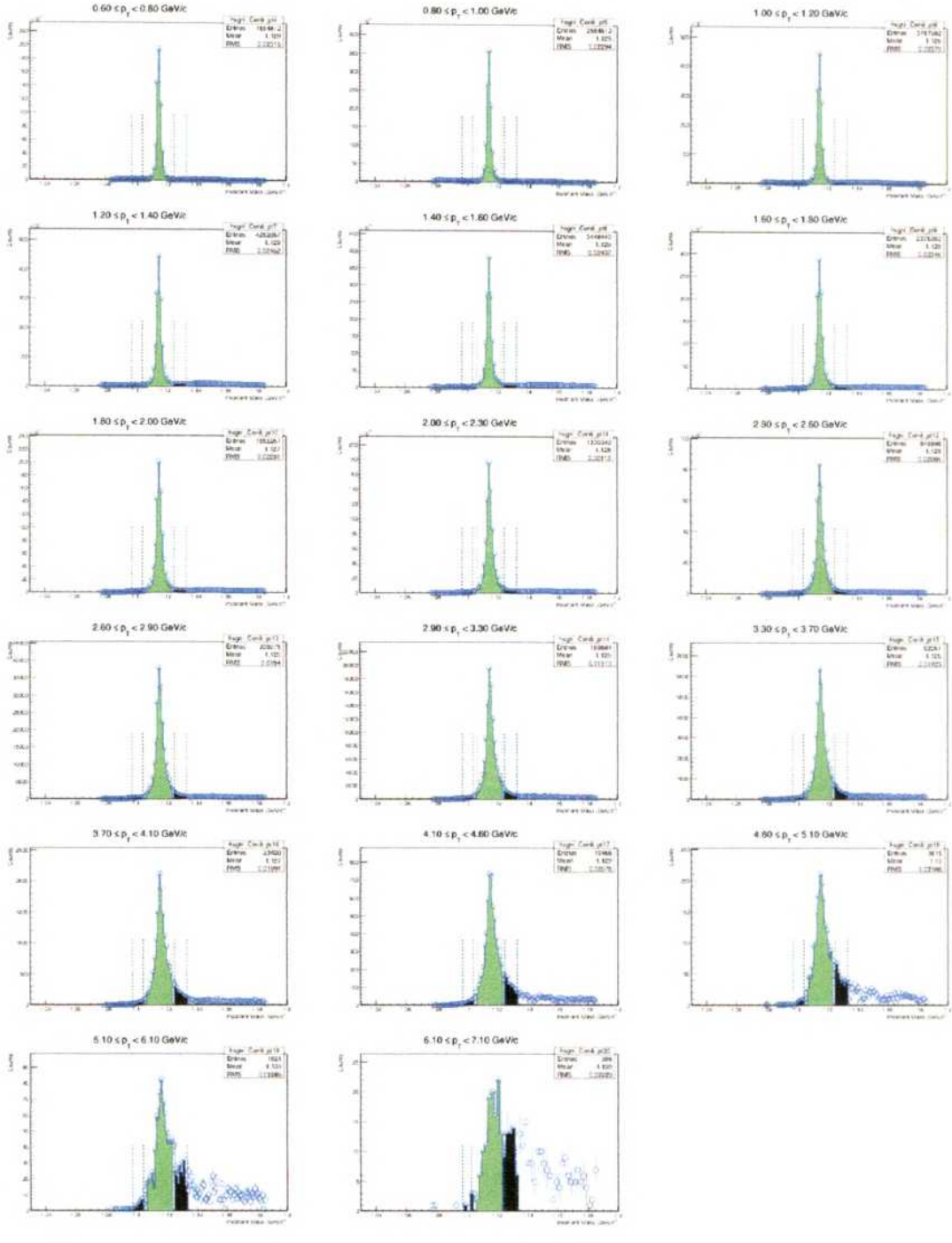

Figure 3.39: Λ Signal distribution in 0-5% centrality.

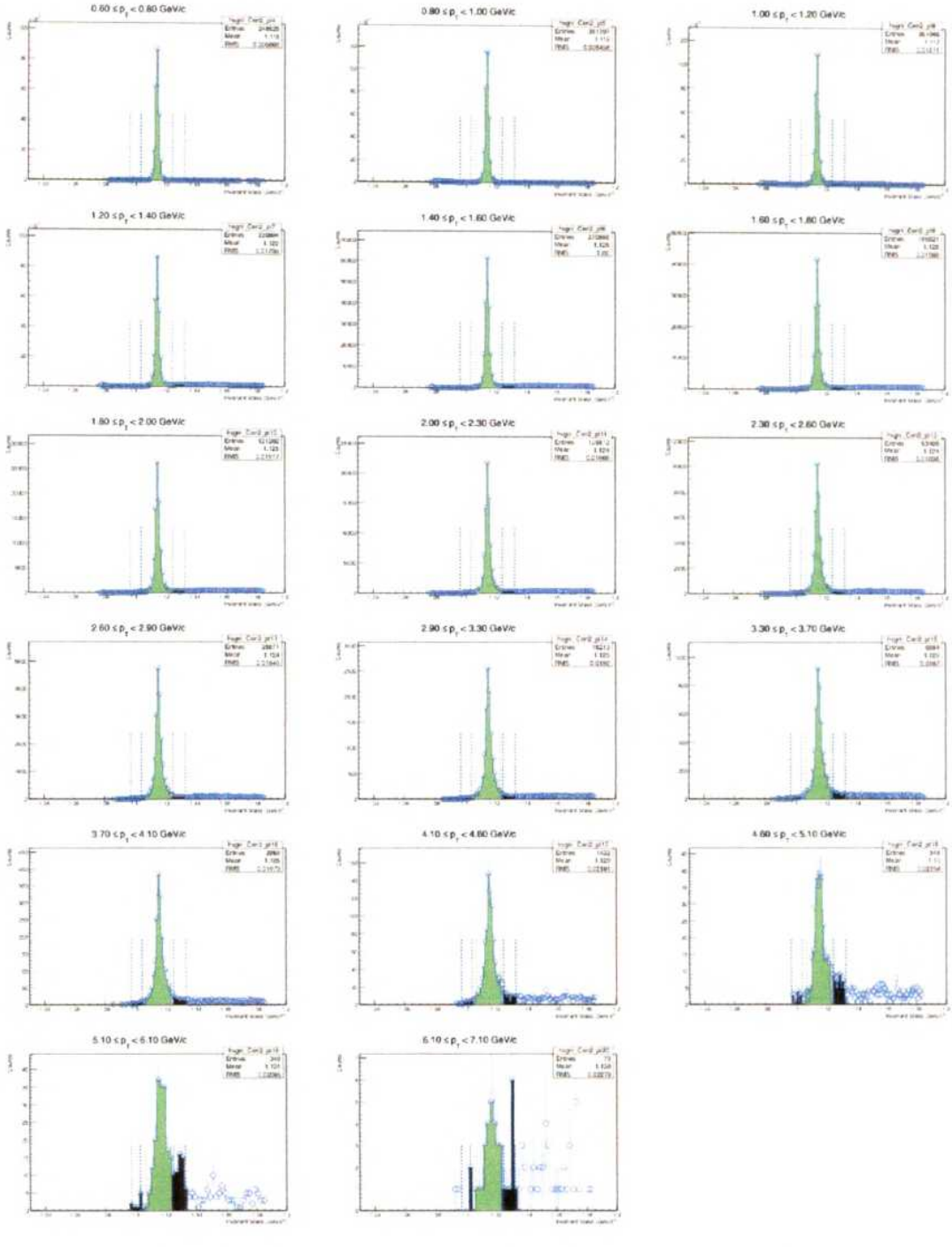

Figure 3.40: Λ Signal distribution in 60-80% centrality.

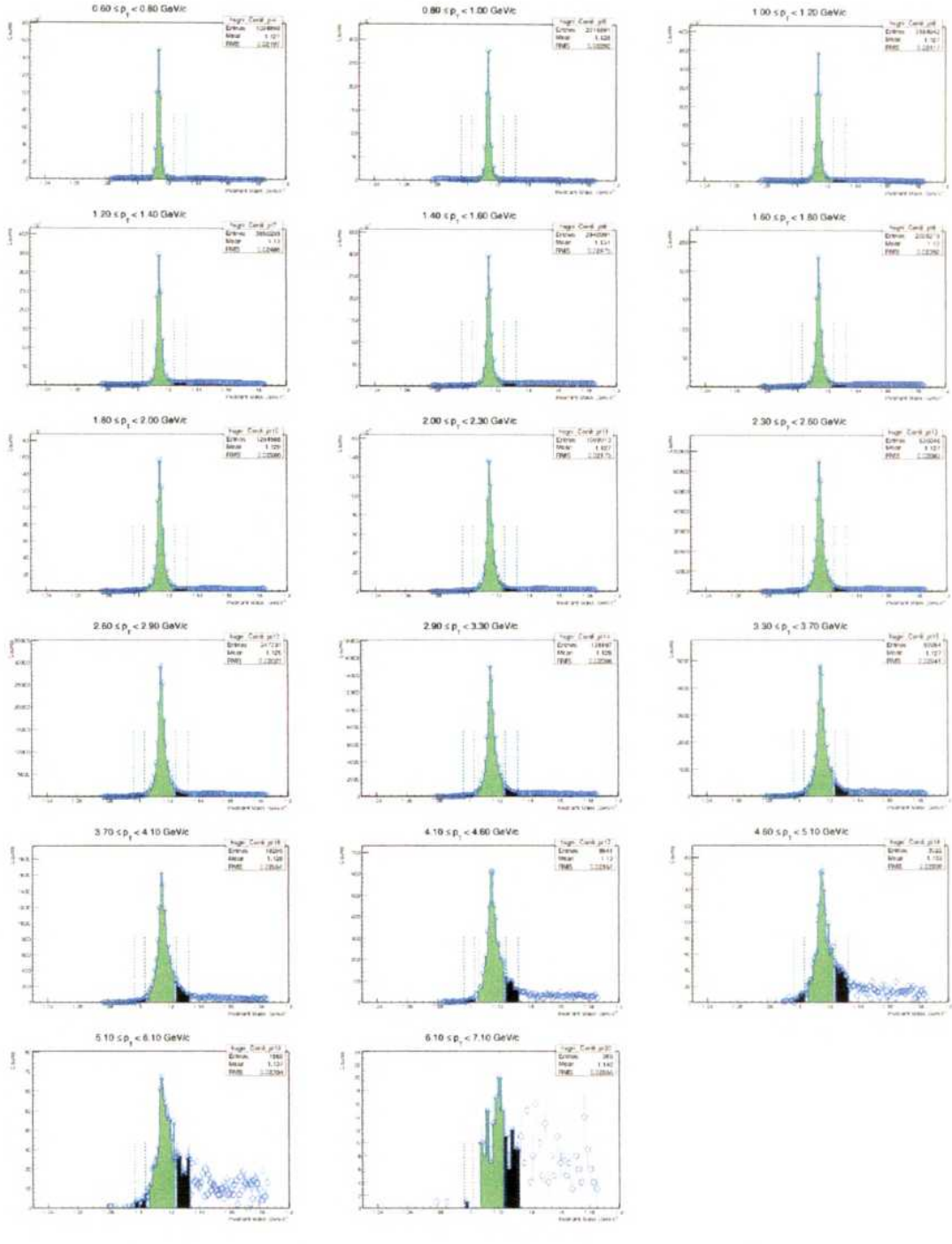

Figure 3.41: $\bar{\Lambda}$ Signal distribution in 0-5% centrality.

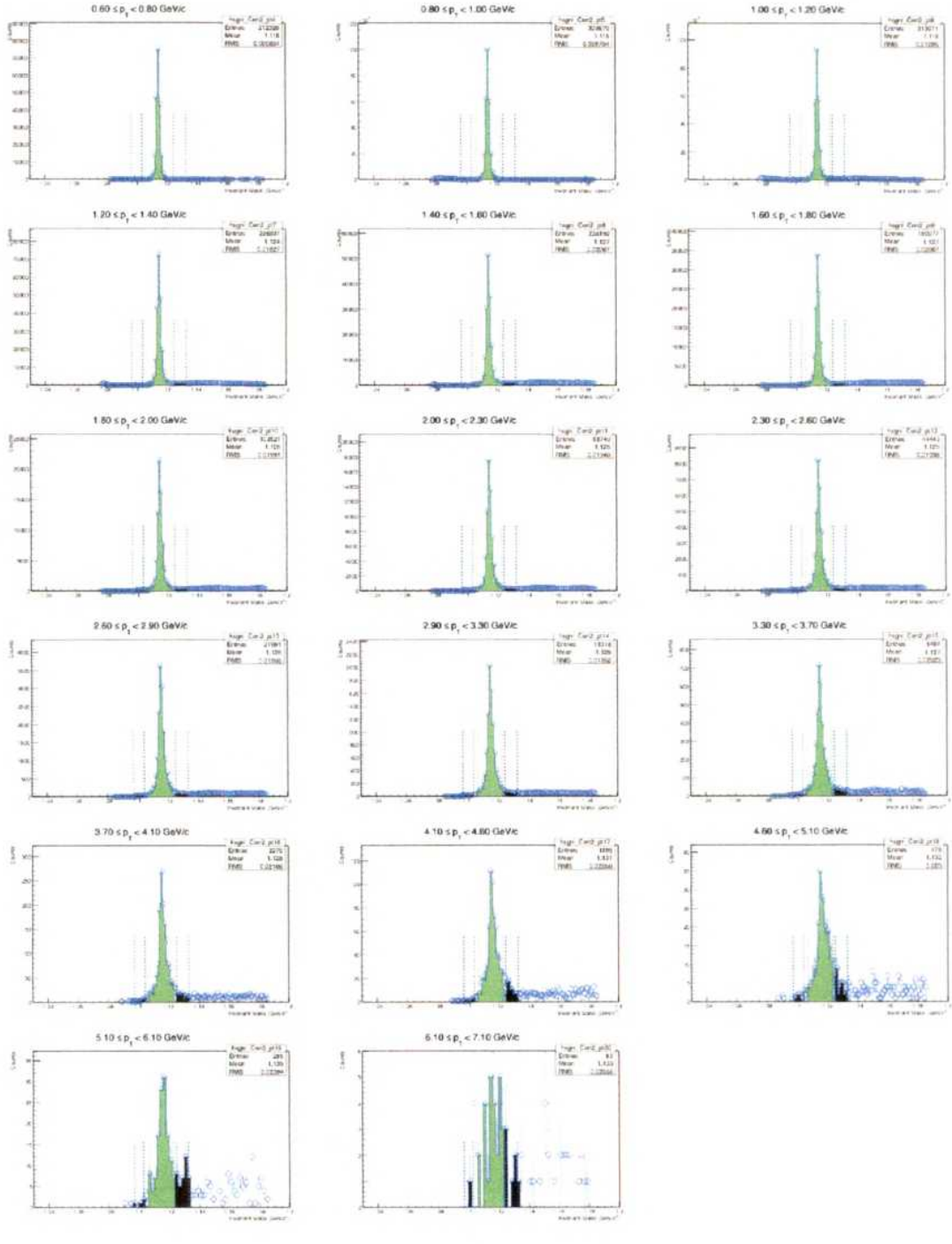

Figure 3.42: $\bar{\Lambda}$ Signal distribution in 60-80% centrality.

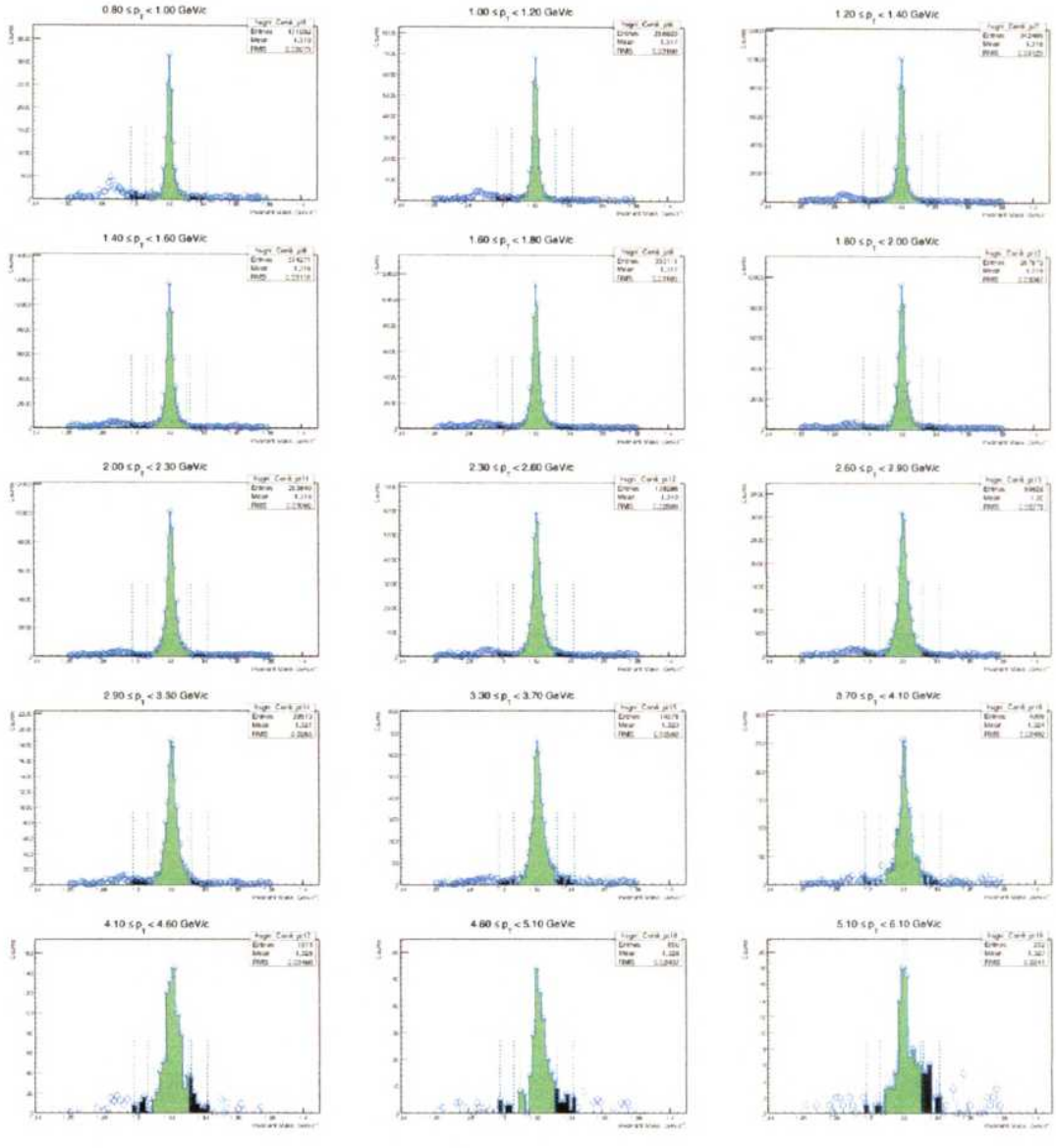

Figure 3.43: Ξ Signal distribution in 0-5% centrality.

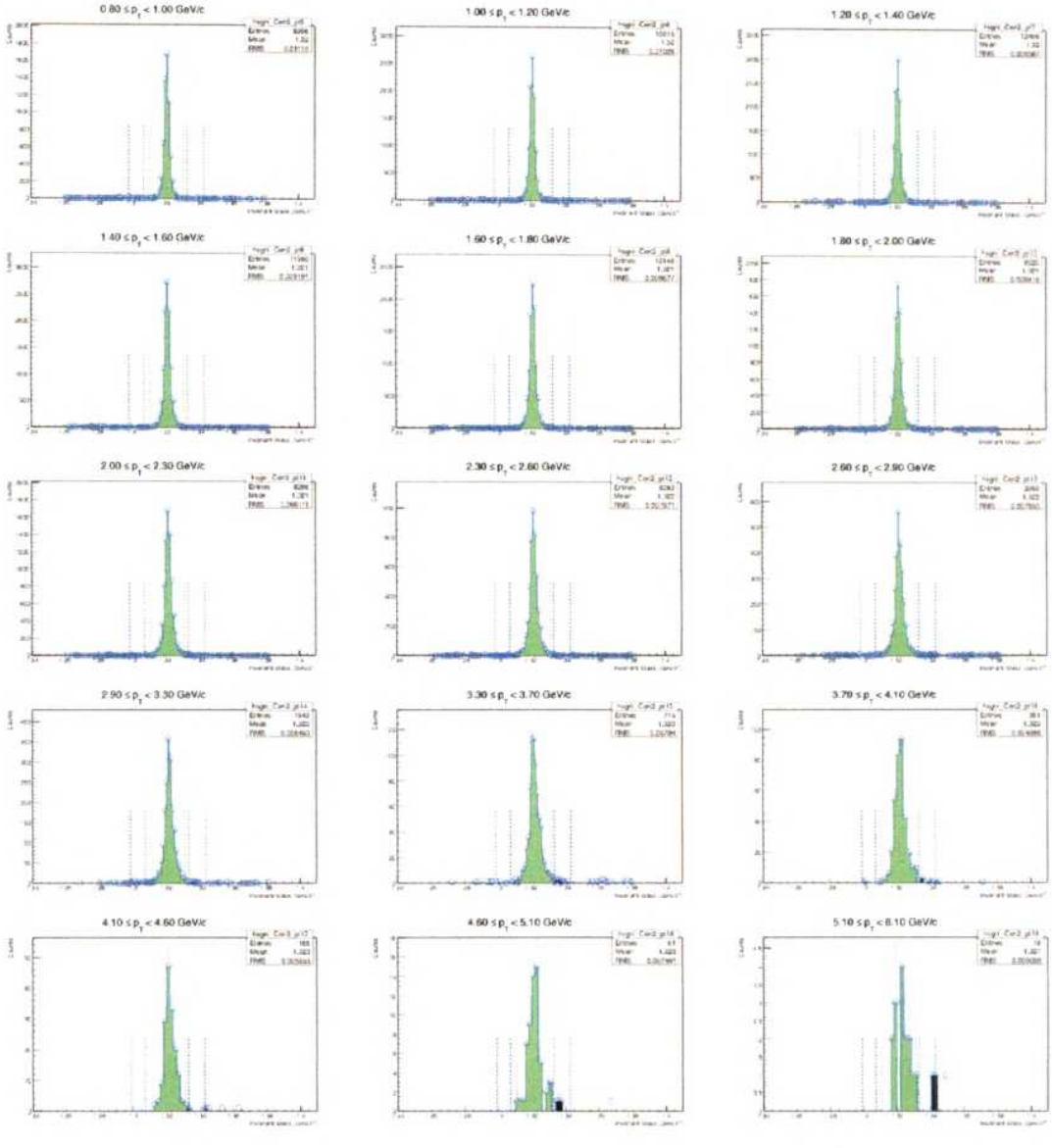

Figure 3.44: Ξ Signal distribution in 60-80% centrality.

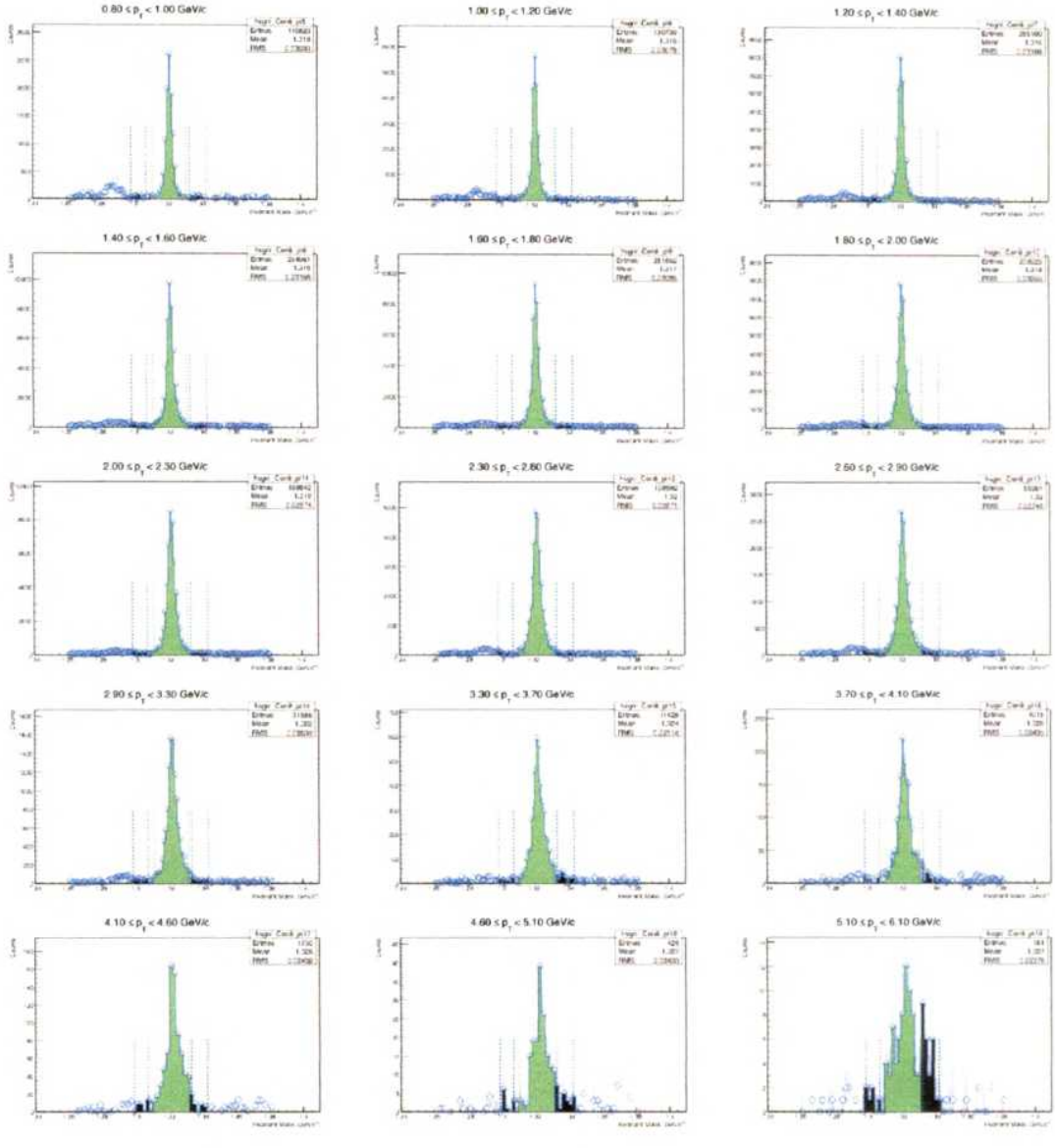

Figure 3.45: $\bar{\Xi}$ Signal distribution in 0-5% centrality.

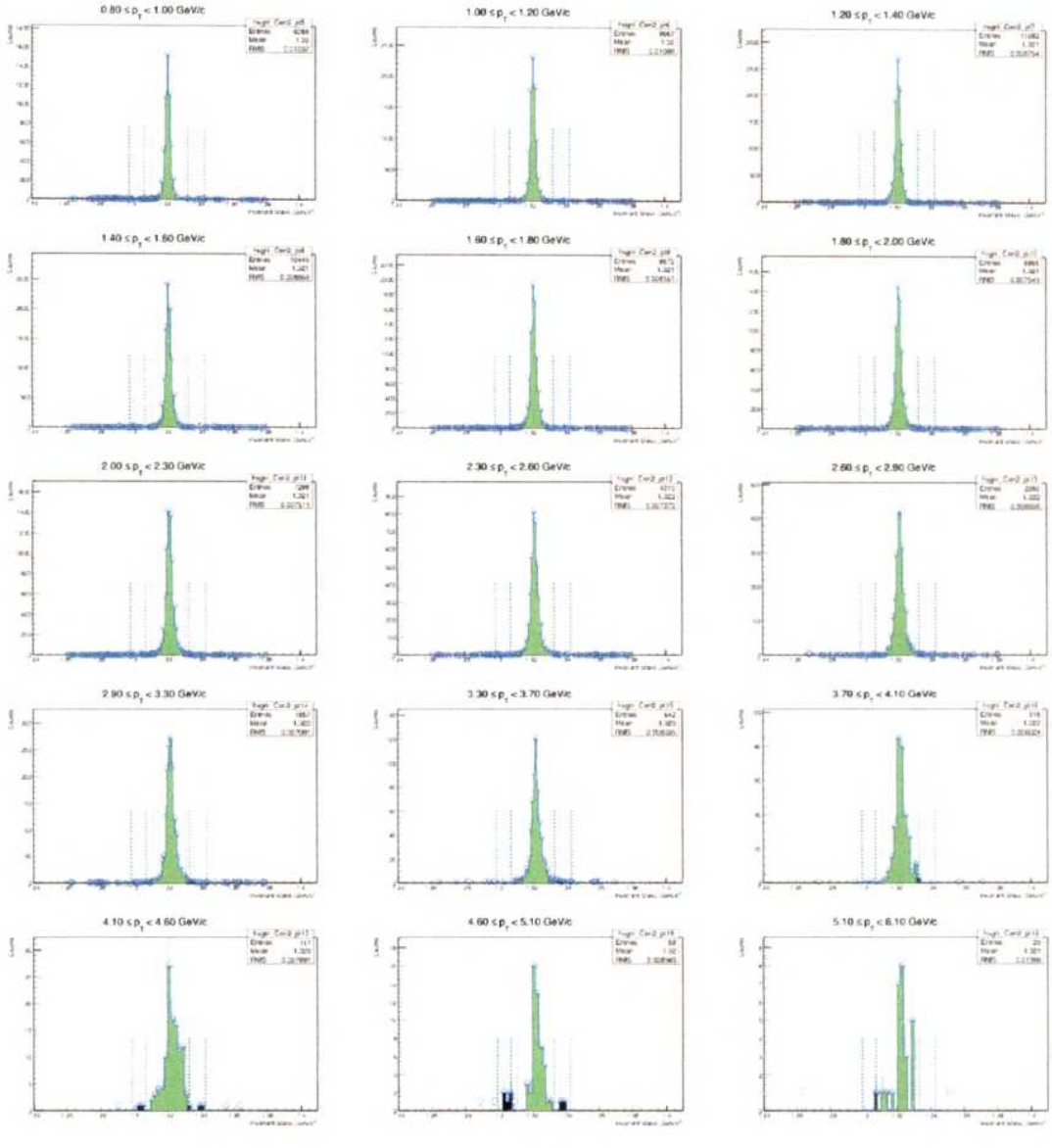

Figure 3.46: $\bar{\Xi}$ Signal distribution in 60-80% centrality.

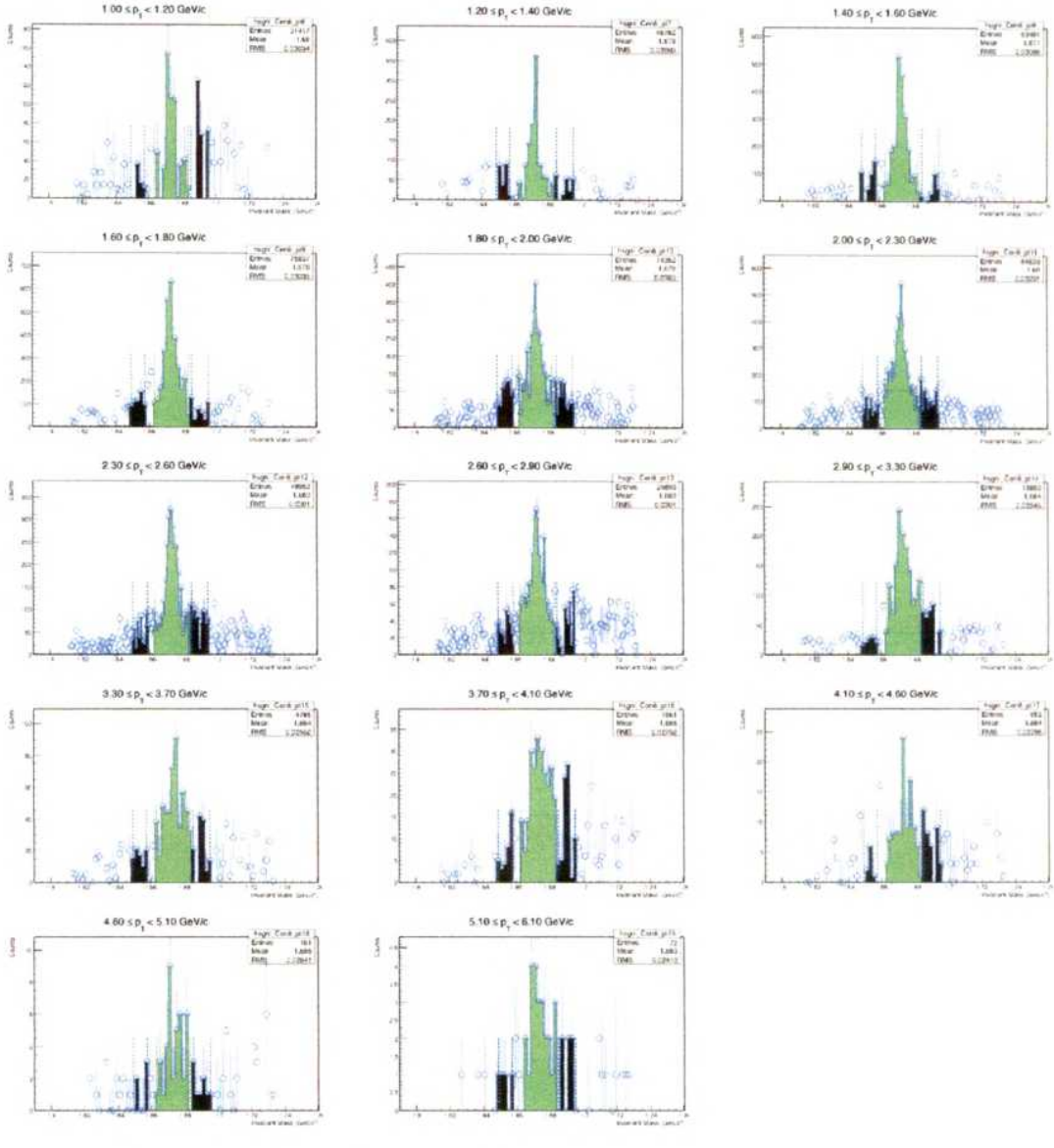

Figure 3.47: Ω Signal distribution in 0-5% centrality.

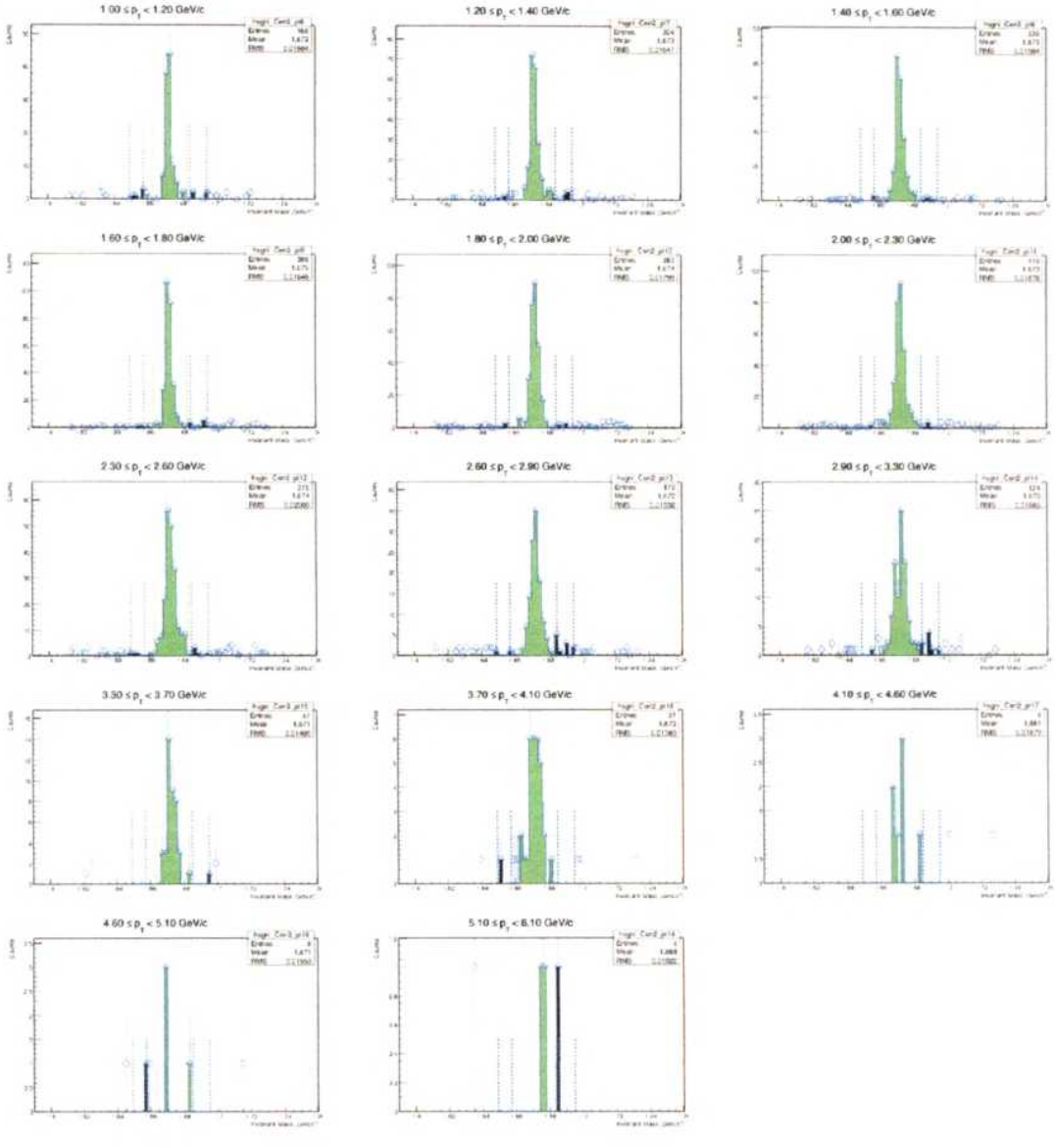

Figure 3.48: Ω Signal distribution in 60-80% centrality.

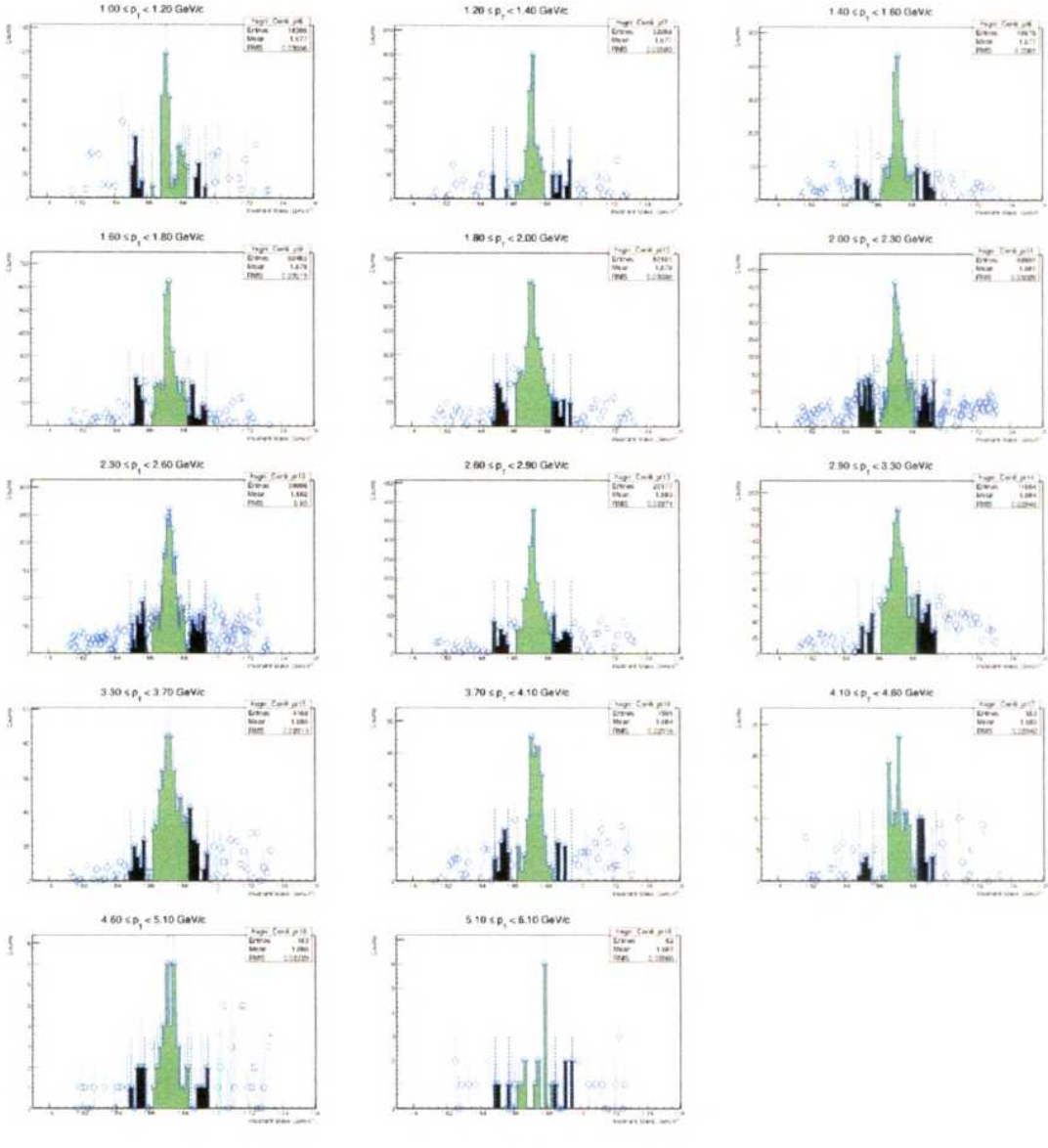

Figure 3.49: $\bar{\Omega}$ Signal distribution in 0-5% centrality.

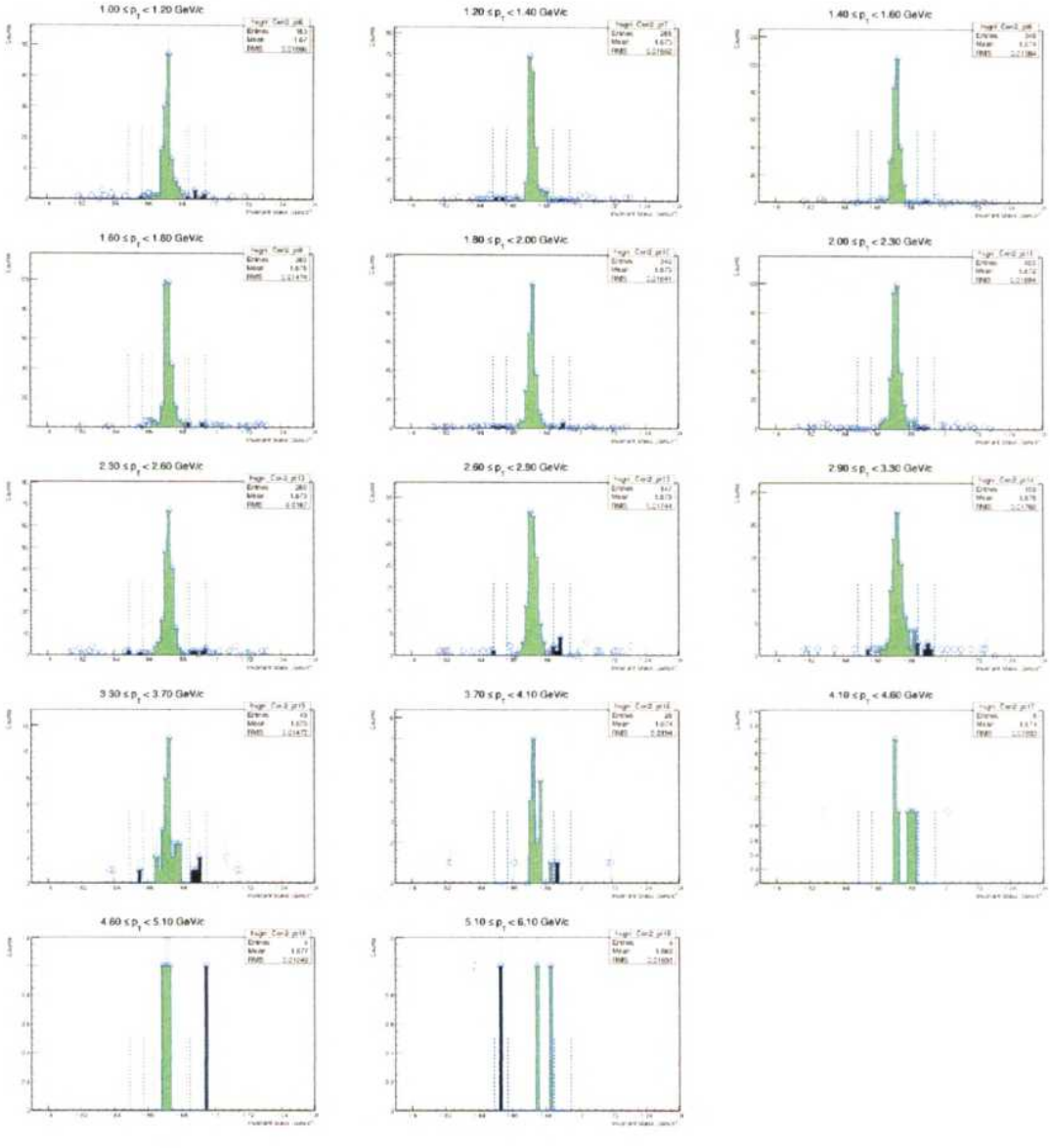

Figure 3.50: $\bar{\Omega}$ Signal distribution in 60-80% centrality.

Chapter 4

Model Implementation of Deformed Nuclei

4.1 Introduction to problem

Nucleon distribution inside nucleus is usually Fermi type, which further parameterised to Wood Saxon (WS) distribution [1]. The distribution was first proposed by Hofstadter in his Noble lecturer [2]. He considered an uniform charge density with smoothed out surface, which in fact taken from electron scattering experiments. However, he considered only spherical nucleus. Questions naturally arise:

- The distribution which we got from spherical nucleus might not hold good for deformed nucleus.

- Owing deformed shape, nucleus can undergo in different type of collision configuration with respect to beam axis and/or impact parameter axis.

There are at least two ways to deal with this.

- We may use spherical harmonic inside WS distribution and try to explain deformed nucleus properties. We refer it as Modified Wood Saxon (MWS) in our study.

- We may use an intrinsic deformed potential. In this study, we have used Nilsson or Modified Harmonic Oscillator (MHO) [3, 4].

For this we have taken an event generator used for relativistic heavy ion collisions, Heavy Ion Jet INTeraction Generator(HIJING) [5] and tried to explain charged particle behaviour at first hand.

Secondly we tried to see, if results from different collision configuration of a deformed nucleus is significantly different when compared with spherical nucleus (with similar number of nucleons or collided with similar centre of mass energy).

We observe that, these approaches certainly improve results in comparison with spherical WS. Also the results from different configuration may change significantly, in comparison with spherical nuclei result.

4.2 Approaches to solve it

4.2.1 Modified Wood Saxon formalism

Three parameter Fermi distribution may be written as:

$$\rho(r) = \rho_0[\frac{1 + w(r/R)^2}{1 + exp[(r - R)/a]}], \tag{4.1}$$

where ρ_0 is the density at center of nucleus, R is the radius of nucleus, a is skin depth or diffuseness parameter, r is a position parameter and distance of any point from centre of the nucleus, and w is the deviation from a smooth spherical surface. These parameters are obtained by fitting to electron scattering data [9, 10].

For w =0; this reduces to WS density distribution:

$$\rho(r) = \frac{\rho_0}{1 + exp[(r - R)/a]}. \tag{4.2}$$

For deformed nucleus (U^{238}), radius (deformed) [11] may be written as :

$$R_{A\Theta} = R[1 + \beta_2 Y_{20}(\theta) + \beta_4 Y_{40}(\theta)], \tag{4.3}$$

The spherical harmonics, Y_{20}, is given by [7],

$Y_{20}(\theta) = \frac{1}{4}\sqrt{\frac{5}{\pi}}(3\ cos^2\theta - 1)$,

and $Y_{40}(\theta) = \frac{3}{16\sqrt{\pi}}(35\ cos^4\theta - 30\ cos^2\theta + 3)$.

We have used deformation parameters $\beta_2 = 0.28$ and β_4 =0.093 [8] in our calculations for uranium nuclei.

Thus we have MWS formalism in hand [12].

4.2.2 Nilsson formalism

For Nilsson, nucleon's single particle distribution $\varrho(r)$ may be written as:

$$\varrho(r) \ = \frac{1}{3\pi^2}[\frac{2m}{\hbar^2}(\lambda_0 - V(r))]^{3/2}. \tag{4.4}$$

Here, V(r ,θ) is the Nilsson potential and λ_0 is the cut on turning point for Nilsson potential, when $\lambda_0 - V(r)$ becomes negative.

Assuming anharmonic oscillator equation for the distorted nucleus, the Nilsson form of $V(r, \theta)$ is taken as follows:

$$\begin{aligned} V(r, \epsilon, \theta) &= \frac{1}{2}\hbar\omega_0(\epsilon)\varrho_t^2\ [1 + 2\epsilon_1\sqrt{\frac{4\pi}{3}}Y_{10}(\theta_t) \\ &- \frac{2}{3}\epsilon_2\sqrt{\frac{4\pi}{5}}Y_{20}(\theta_t) + 2\sum_{\lambda=3}^{\lambda_{max}}\epsilon_\lambda\sqrt{\frac{4\pi}{2\lambda+1}}Y_{\lambda 0}(\theta_t)]\,. \end{aligned} \tag{4.5}$$

The position of the nucleon from nucleus centre, ϱ_t in the stretched spherical coordinates is given by: $\varrho_t^2 = \xi^2 + \eta^2 + \zeta^2\,[fm^2]$,
where $\xi = x[\frac{m\omega_0(\epsilon)}{\hbar}(1 + \frac{1}{3}\epsilon_2)]^{1/2}$, $\eta = y[\frac{m\omega_0(\epsilon)}{\hbar}(1 + \frac{1}{3}\epsilon_2)]^{1/2}$ and $\zeta = z[\frac{m\omega_0(\epsilon)}{\hbar}(1 - \frac{2}{3}\epsilon_2)]^{1/2}$.

So, we have Nilsson distribution for nucleons inside Uranium nucleus [13].

These two approaches (MWS and MHO) are implemented inside an event generator HIJING. However, here we will follow only MWS formalim.

4.3 Model Implementation

4.3.1 HIJING Model

HIJING [5] is a Monte Carlo model designed mainly to explore the range of possible initial conditions that may occur in nuclear collisions at collider energies and to produce output that can be compared directly with a wide variety of nuclear collider experimental observables. The main features included in HIJING are as follows.

- The formulation of HIJING is guided by Lund FRITIOF [16] and Dual Parton Model [17] for soft nuclear reaction at intermediate energy ($\sqrt{s_{NN}} \leq 20$ GeV). Multiple low p_T exchanges among the end point constituents are included to model initial state interactions.

- The PYTHIA [18] guides the pQCD processes, where multiple minijet production with initial and final state radiation are involved.

- To reproduce p+A or A+A results, the Eikonal formalism is used to calculate the number of minijets per inelastic p+p collision.

- The model uses three-parameter Woods-Saxon nuclear density determined by electron scattering data [19].

- A diffuse nuclear geometry decides the impact parameter dependence of the number of binary collisions [20].

The cross section for hard parton scattering at the leading order is written as [21]

$$\frac{d\sigma_{cc}^{pp}}{dp_T^2 dy_1 dy_2} = K \sum_{a,b} x_1 f_a(x_1, p_T^2)\ x_2 f_b(x_2, p_T^2) \times \frac{d\hat{\sigma}_{ab}}{d\hat{t}}, \tag{4.6}$$

here a, b are the parton species, y_1, y_2 are the rapidities of the scattered partons, and x_1, x_2 are the fraction of momentum carried by the initial partons. A factor K, of value 2.0 has been used to account roughly for the higher order corrections. In HIJING, the parton structure functions, $f_a(x_1, p_T^2)$ are the Duke-Owens [22] structure function set 1 and this is also implemented in PYTHIA. For the nuclear effect in A+A and p+A collisions, model follows the A dependence of the shadowing proposed in Ref. [23, 24] and uses its parameterization as

$$R_A(x) \equiv \frac{f_{a/A}(x)}{A\ f_{a/N}(x)} = 1 + 1.19\ ln^{1/6}A[x^3 - 1.5(x_0 + x_L)x^2 + 3x_0x_Lx] - \left[\alpha_A(r) - \frac{1.08(A^{1/3}-1)}{ln(A+1)}\sqrt{x}\right]e^{-x^2/x_0^2}\ , \tag{4.7}$$

and $\alpha_A(r) = 0.1(A^{1/3} - 1)\frac{4}{3}\sqrt{1 - r^2/R_A^2}$.
Here r is the transverse distance of the interacting nucleon from its nucleus centre and R_A is the radius of the nucleus, and $x_0 = 0.1$ and $x_L = 0.7$. The most important nuclear dependence term is proportional to $\alpha_A(r)$ in Eq.4.7, which determines the shadowing for $x < x_0$, and the rest gives the overall very slow A dependence nuclear effect on the structure function for $x > x_L$.

We have used HIJING version 1.41.

We have constructed probability density by weighting with differential volume elements $r^2 sin(\theta)$. As the nucleus is deformed one, so there are various collision configurations are possible, viz body-body, tip-tip, side-side etc. For random orientation, polar angle (angle between beam axis and major axis, $\Theta \in [0, \pi)$ sampled according to $sin(\Theta)$ probability distribution and azimuthal angle (angle between major axis and impact parameter, $\Phi \in [0, 2\pi)$ sampled with uniform distribution. Among that, if major axis of nuclei is perpendicular to beam axis, we refer it as body-body collisions and for tip-tip it is aligned with beam axis.

We have used RHIC energy, U+U $\sqrt{s_{NN}} = 193$ GeV for our analysis. For this, we have generated $\sim 5 \times 10^6$ events. Charged particles are considered in our analysis

Table 4.1: Average number of participants and binary collisions

system and energy	centrality	$< N_{part} >$	$< N_{coll} >$
Au+Au, 200 GeV	0-5%	352.794	970.368
Au+Au, 200 GeV	70-80%	7.892	8.751
U+U, 193 GeV	0-5%	432. 77	1436.16
U+U, 193 GeV	70-80%	10.868	10.462

(π, k and p).

4.3.2 Calculation of $< N_{part} >$ and $< N_{coll} >$ values

Average number of participating nucleons(N_{part}) and average number of binary collisions(N_{coll}) have been calculated using Glauber model with optical approximation. These are in fact function of centrality of collision [15]. This may be written as:

$$T_{AB}(b) = \int T_A(s) \, . T_B(|\mathbf{s} - \mathbf{b}|) \, d^2s \, , \tag{4.8}$$

where, $T_{AB}(b)$ is the nucleus overlap function at a given impact parameter, b.

So $< N_{coll} >$ for collisions of $A + B$ nucleus, is given by

$$N_{coll}(b) = A.B.T_{AB}(b).\sigma_{NN} \, , \tag{4.9}$$

and N_{part} as,

$$\begin{aligned} N_{part}(b) &= A. \int T_A(s).\Big\{1 - [1 - T_B(|\mathbf{s} - \mathbf{b}|)\sigma_{NN}]^B\Big\}.d^2s \\ &+ B. \int T_B(|\mathbf{s} - \mathbf{b}|).\Big\{1 - [1 - T_A(s)\sigma_{NN}]^A\Big\}.d^2s \, , \end{aligned} \tag{4.10}$$

where σ_{NN} being nucleon-nucleon inelastic cross section. In Tab. 4.1, we have given $< N_{part} >$ and $< N_{coll} >$ values for most central and most peripheral collisions in Au+Au 200 GeV and U+U 193 GeV.

4.4 Results and Discussions

In Fig 4.1, we have shown N_{ch}(charged particle multiplicity) distribution from HIJING in both U+U and Au+Au collisions systems. Particles with mid-rapidity ($|\eta| < 0.5$) and minimum-bias collision are considered here. Results from random configuration lies in between body-body and tip-tip configurations. Body-body configuration gives least number of charged particles and tip-tip configuration gives higher charged particles. N_{ch} distribution for Au+Au collisions at $\sqrt{s_{NN}} = 200$ GeV is less than all configurations of U+U collisions. However, both of them shows 2 times magnitude difference from STAR experiments's preliminary data [14].

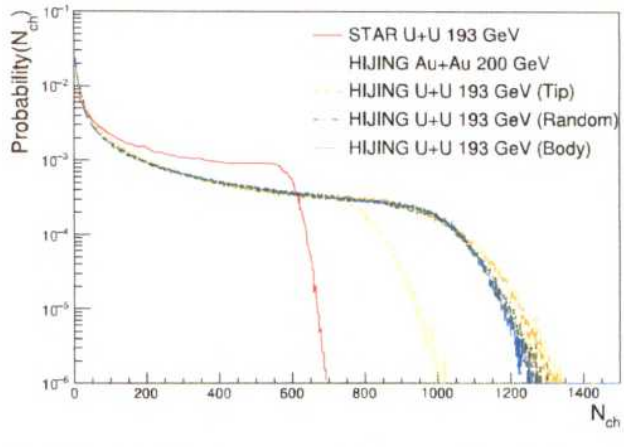

Figure 4.1: N_{ch} for U+U collisions at $\sqrt{s_{NN}} = 193$ GeV and Au+Au collisions at $\sqrt{s_{NN}} = 200$ GeV from HIJING. We have shown experimental data for U+U at $\sqrt{s_{NN}} = 193$ GeV [14] along with this.

In Fig 4.2 transverse momentum (p_T) spectra for most central (0-5%) and most peripheral collisions (70-80%) are shown, for U+U collisions at $\sqrt{s_{NN}} = 193$ GeV and Au+Au collisions at $\sqrt{s_{NN}} = 200$ GeV at top plot. In the bottom, ratio betweeb various types of U+U configuration to the Au+Au results are presented. We observe that, in U+U give higher magnitude in central collisions, while Au+Au give higher magnitude for peripheral centrality. Reverse of magnitude of p_T spectra, might be reflected in ratio plots viz. as nuclear modification factor.

In Fig 4.3 we have shown nuclear modification factor (R_{CP}) as a function of p_T.

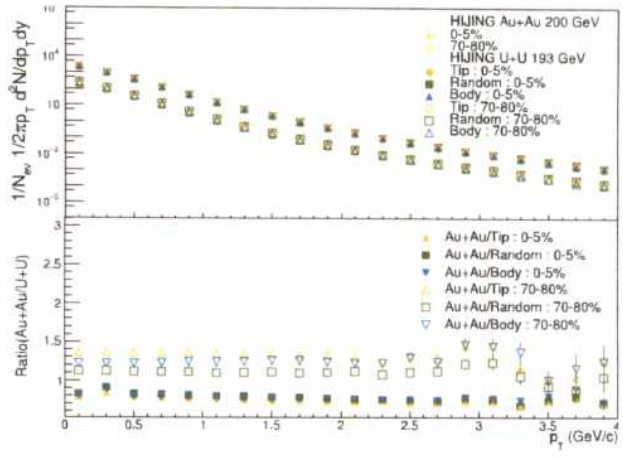

Figure 4.2: p_T spectra for U+U collisions at $\sqrt{s_{NN}} = 193$ GeV and Au+Au collisions at $\sqrt{s_{NN}} = 200$ GeV from HIJING.

This may be defined as:

$$R_{CP} = \frac{d^2N/dp_T dy/ < N_{coll}^{cent} >}{d^2N/dp_T dy/ < N_{coll}^{Perph} >} . \tag{4.11}$$

Where $< N_{coll}^{cent} >$ and $< N_{coll}^{Perph} >$ are average number of binary collisions in most central and most peripheral collisions. We indeed observe, R_{CP} for U+U is higher than Au+Au, although there is little difference in magnitude.

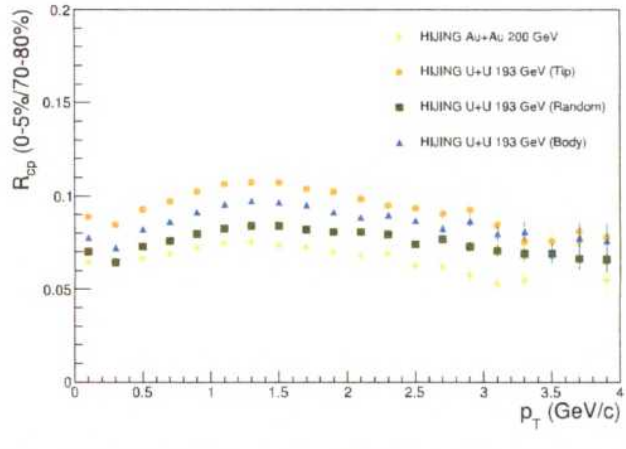

Figure 4.3: R_{CP} for U+U collisions at $\sqrt{s_{NN}} = 193$ GeV and Au+Au collisions at $\sqrt{s_{NN}} = 200$ GeV from HIJING.

Particle ratios as function of p_T is plotted in Fig 4.4. In the left plot, we show p/π and k/π ratio for most central collisions (0-5%) as a function of p_T and in right plot, we have shown anti-particle to particle ratios π^-/π^+, k^-/k^+ and $\bar{p}/p$. We

observe from $p_T > 1$ GeV onward, the trend of k/π ratio reverses from p/π ratio. While pions with anti-pions gives ratio close to unity, others particle ratios decrease from unity after $p_T > 1$ GeV. Interestingly, we do not observe any orientation or collision configuration dependencies in either of the ratio plots.

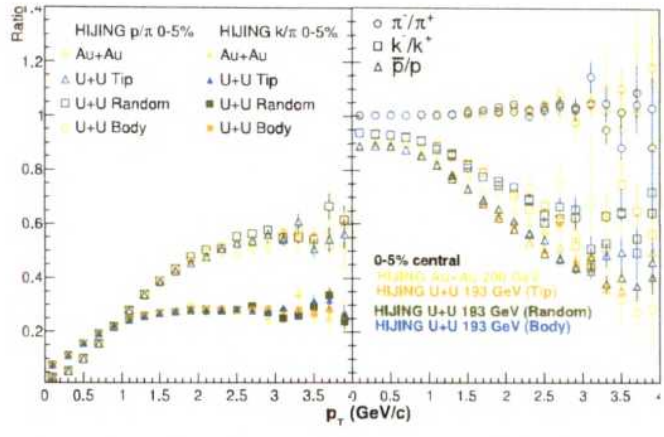

Figure 4.4: Particle ratios for U+U collisions at $\sqrt{s_{NN}} = 193$ GeV and Au+Au collisions at $\sqrt{s_{NN}} = 200$ GeV from HIJING.

Our study shows that, particular collision configuration of U nuclei can yield higher number of particles than other one's. One of the key interesting feature is, if p_T spectra of charged particles measured in data, we think, U+U collisions give higher magnitude than Au+Au in most central collision (0-5%) only. Trend will be flipped for most-peripheral collision (70-80%). This will be reflected in nuclear modification factor, i.e. Au+Au system will be more suppressed than U+U system, although difference will be less. We also propose that, charged particle ratios might not show any difference between U+U and Au+Au collision systems.

Bibliography

[1] Roger D. Woods and David S. Saxon, Phys. Rev. 95, 577, 1954

[2] R. Hofstadter, Nobel Lecture, December 11, 1961

[3] Shapes and Shells in nuclear structure, Nilsson and Ragnarsson, Cambridge Univ. Press,1995

[4] Structure Of The Nucleus by M. A. Preston, Bhaduri, R. K. Bhaduri, WestView Press, 1993

[5] Miklos Gyulassy and Xin-Nian Wang, Comput.Phys.Commun. 83, 307,1994

[6] M Brack et al, Nuclear Physics A, 234, 185-215 (1974)

[7] C 5, Quantum Theory of Angular Momentum, By D A Varshalovich, A N Moskalev, V K Khersonskii, Singapore: World Scientific (1988)

[8] P.Moller, J.R.Nix, W.D.Myers and W.J.Swiatecki,Atomic Data and Nuclear Data Tables 59 185 (1995)

[9] R.C. Barrett and D.F. Jackson, Nuclear Sizes and Structure (Oxford University Press, New York, 1977)

[10] H. De Vries, C.W. De Jager, C. De Vries, Atomic Data and Nuclear Data Tables 36 (1987) 495.

[11] D.L. Hendrie, N.K. Glendenning, B.G. Harvey, O.N. Jarvis, H.H. Duhm, J. Saudinos, J. Mahoney, Physics Letters B Volume 26, Issue 3, Pages 127-130,1968

[12] S. K. Tripathy et al, arXiv:1805.02713, Nuclear Physics A, Available online 25 September 2018

[13] S. K. Tripathy et al, arXiv:1802.00639

[14] Hui Wang (Brookhaven National Lab) Quark Matter 2014 - Talk `https://indico.cern.ch/event/219436/contributions/1523576/`

[15] Michael L. Miller, Klaus Reygers, Stephen J. Sanders, and Peter Steinberg, Annu. Rev. Nucl. Part. Sci., 57:205-243,2007

[16] B. Andersson, G. Gustafson, and B. Nilsson-Almqvist, Nucl. Phys. **B 281**, 289 (1987); B. Nilsson-Almqvist and E. Stenlund, Comp. Phys. Commun. **43**, 387 (1987).

[17] A. Capella, U. Sukhatme, and J. Tran Thanh Van, Z. Phys. **C 3**, 329 (1980); J. Ranft, Phys. Rev. **D 37**, 1842 (1988); J. Ranft. Phys. Lett. **B 188**, 379 (1987).

[18] T. Sjostrand and M. van Zijl, Phys. Rev. **D 36**, 2019 (1987); T. Sjostrand, Comput. Phys. Commun.**39**, 347 (1986); T. Sjostrand and M. Bengtsson, ibid. **43**, 367 (1987).

[19] C. W. Dejager, H. DeVries, and C. DeVries, At. Data Nucl. Data Tables **14**, 479 (1974).

[20] ATTILA (ALL TYPE TARGET INDEPENDENT LUND ALGORITHM) FOR NUCLEAR COLLISIONS AT approximately 200-AGeV , M. Gyulassy, in Proceedings of Eighth Balatonfured Conference on nuclear Physics, edited by Z. Fodor (KFKI, Budapest, 1987); CERN Report No. CERN-TH-4794/87, 1987.

[21] E. Eichten, I. Hinchliffe, K. Lane, and C. Quigg, Rev. Mod. Phys. **56**, 579 (1984).

[22] D. W. Duke and J. F. Owens, Phys. Rev. **D 30**, 50 (1984).

[23] A. H. Mueller and J. Qiu, Nucl. Phys. **B 268**, 427 (1986); J. Qiu, ibid. **B 291**, 746 (1987).

[24] L. L. Frankfurt and M. I. Strikman, Phys. Rep. **160**, 235 (1988).

Chapter 5

Conclusion

In this thesis work, we have done STAR data analysis of U+U collisions at $\sqrt{s_{NN}}$ = 193 GeV, taken during the year 2012.

Chapter one introduces Quark Gluon Plasma and few of it's signatures. We have presented how these signatures signifies some of important aspects of QGP in brief. As this thesis based on strangeness in particular, we have presented history of it and up to what level studies are carried out. We mentioned what we plan further to study with strangeness at top RHIC energy.

Chapter two represents experimental facility at RHIC in general and STAR experiment in particular. STAR experiment involves more than one detector, we restrict ourself to the detector(s) used for thesis work. We have shown TPC detector technical design, particle identification mechanism, reconstruction of position of particle along with momentum resolution. We also presented cooling of detectors, calibration and computing system, how these collision information made data.

Chapter three presents our data analysis result. Here, we have reconstructed K_s, $\Lambda(\bar{\Lambda})$, $\Xi(\bar{\Xi})$ and $\Omega(\bar{\Omega})$ from their hadronic decay channels. We have also compared our results with published Au+Au 200 GeV results. Mass of these reconstructed particles, are with in uncertainties of PDG values. Measured with of particles are due to finite detector resolution. We have investigated detector acceptance and efficiency factors, to correct transverse momentum (p_T) spectra. We observed a clear centrality dependence of p_T for all particles. We have measured Nuclear modification factor

(R_{CP}). This allows us to disentangle between hot and cold nuclear matter effect. We have observed that, all particles shows suppression from unity, which hints presence of nuclear matter under extreme conditions. As this thesis work involves single, double and multi-strange hadrons, we took this opportunity to check hierarchy of strangeness dependence of in R_{CP}. We observe the order $K_s < \Lambda < \Xi < \Omega$. This means light mass particles are affected most, while heavy mass particles are least affected. We also observe that, particles and anti-particles are suppressed of similar order. We have measured anti-particle to particle ratios, viz $\bar{\Lambda}/\Lambda$, $\bar{\Xi}/\Xi$, $\bar{\Omega}/\Omega$ in most central and most peripheral collisions. We observe that, they are independent of centrality. We also observe that, they do not depend on strangeness content. Our results on R_{CP} and particle ratios are consistent with published results.

Chapter four presents phenomenology results with deformed nucleus collision. We have used spherical harmonics with wood saxon density distribution and implemented in one of event generators used in heavy-ion collision formalism, HIJING. Also we have taken an intrinsically deformed density distribution, Nilsson in the same model. Mid-rapidity Charged particles are used in our study. We investigated our analysis in the energy & system of STAR data along with Au+Au collisions at $\sqrt{s_{NN}} = 200$ GeV. Our study shows that, p_T spectra, might show a higher magnitude than U+U collision in peripheral collision, although in central collision U+U system dominates. This will lead the fact that, nuclear matter created in Au+Au system will be more suppressed than U+U, in similar energy. Our study also suggests that, if we can distinguish between different types orientations, then particle ratios will not be useful one, rather p_T spectra in peripheral collision will shed some light.

Future scope of this work, lies for experimental ability of distinguishing different types of collision configurations from all possible one. If we can do this, we can indeed check, geometrical orientations dependence of physics observables in single collision system.